



8-2013

# On Strong Pressure Waves in Cylinders

Andrew W. Wilson  
awilso45@utk.edu

---

## Recommended Citation

Wilson, Andrew W., "On Strong Pressure Waves in Cylinders." PhD diss., University of Tennessee, 2013.  
[https://trace.tennessee.edu/utk\\_graddiss/2497](https://trace.tennessee.edu/utk_graddiss/2497)

This Dissertation is brought to you for free and open access by the Graduate School at Trace: Tennessee Research and Creative Exchange. It has been accepted for inclusion in Doctoral Dissertations by an authorized administrator of Trace: Tennessee Research and Creative Exchange. For more information, please contact [trace@utk.edu](mailto:trace@utk.edu).

To the Graduate Council:

I am submitting herewith a dissertation written by Andrew W. Wilson entitled "On Strong Pressure Waves in Cylinders." I have examined the final electronic copy of this dissertation for form and content and recommend that it be accepted in partial fulfillment of the requirements for the degree of Doctor of Philosophy, with a major in Aerospace Engineering.

Gary Flandro, Major Professor

We have read this dissertation and recommend its acceptance:

Trevor Moeller, John Steinhoff, Kivank Ekici, Monty Smith

Accepted for the Council:

Dixie L. Thompson

Vice Provost and Dean of the Graduate School

(Original signatures are on file with official student records.)

---

On Strong Pressure Waves in Cylinders

A Dissertation  
Presented for the  
Doctor of Philosophy  
Degree  
The University of Tennessee, Knoxville

Andrew W. Wilson

August 2013

## **Dedication**

For my wife, for our child, for God.

## Acknowledgments

The author wishes to gratefully acknowledge the following people.

Dr. Gary Flandro, who built the foundation for this work.

Drs. Trevor Moeller, Kivanc Ekici, Monty Smith and John Steinhoff, who generously gave of their time to help me through the PhD process.

Dr. Eric Jacob, who built the ground floor of this work, and whose mentoring made all this work possible.

Drs. Josh Batterson and R. Joel Thompson, whose encouragement and intellectual stimulation kept the work interesting.

GTL Laboratories, Inc. and the Space Institute, whose financial support enabled the work.

The University of Tennessee Space Institute, which offered both opportunity to work and a wonderful place to work.

Starbucks of Manchester, Tennessee, whose caffeine and friendship kept the work going.

Every good soul of the Internet who has ever answered the question “how do you do *this* in *that* software”.

The Church of Christ at Cedar Lane, where God’s work in all its forms finds favour.

# Abstract

High power-density devices such as liquid rocket engines and gas turbine power plants often experience *combustion instabilities*, when the fluid flow ceases to be smooth and begins oscillating. These flow oscillations often have pressure oscillations with negative consequences.

Much work has been done in recent years to extend the theories describing these combustion instabilities to cover high-amplitude waves, where the behavior ceases to be linear and energy cascades through the natural modes of the system. However, in cylindrical geometries, a tension exists between the usual model (that energy cascades through natural modes) and the observed phenomena (which usually contains integer harmonics of the primary frequency), as the natural frequencies of circular waves are *not* harmonics of each other.

One old theory describes strong cylindrical waves, predicting that the natural mode shapes will change in the presence of strong nonlinearity. Several recent theories use an assumption that the natural modes do not change in strong waves, and that the nonlinear solution can be expressed in terms of these unchanged natural modes. All the theories shared a lack of strong, direct experimental validation for strong cylindrical waves.

An experiment was located which exhibits the properties under consideration, and that experiment was modeled with four different theories. The theories successfully modeled the major behavior of the experiment, with varying degrees of quantitative agreement. Three of the theories did not make the assumption that the linear mode shapes do not change, and were used to evaluate the quality of that assumption.

Further, the three theories that permitted it all showed a spatially-distributed, time-independent pressure shift: a DC offset with a radial dependence. This valley-shaped time-independent pressure feature was not found in the literature, though it would have important consequences to engine design and operation if it is real.

# Contents

<b>1</b>	<b>Introduction</b>	<b>1</b>
1.1	The Combustion Instability Problem . . . . .	1
1.2	Strong Cylinder Waves . . . . .	3
1.2.1	Standing Pressure Waves . . . . .	3
1.2.2	Cylinder Waves . . . . .	9
1.2.3	Strong Waves . . . . .	12
1.2.4	Some Issues with Terminology . . . . .	12
1.3	State of the Art . . . . .	15
1.3.1	CFD Instability Modelling . . . . .	16
1.3.2	Linear Combustion Instability Theory . . . . .	17
1.3.3	Nonlinear Combustion Instability Theory . . . . .	18
1.3.4	Strong Cylindrical Instabilities . . . . .	19
1.4	New Contributions . . . . .	19
1.4.1	Experiment . . . . .	21
1.4.2	Why Waves Steepen . . . . .	21
1.4.3	The Mode/Frequency Assumption . . . . .	21
1.4.4	DC Shift Valley . . . . .	22
1.5	Summary of Procedure . . . . .	23
1.5.1	Model Problem . . . . .	23
1.5.2	Evaluating Theories . . . . .	23
1.5.3	Experimental Validation . . . . .	24
1.5.4	Mode/Harmonic Decomposition . . . . .	24
1.5.5	Error Energy . . . . .	25
1.6	Summary of Work . . . . .	26
<b>2</b>	<b>Steepened Wave Experiments</b>	<b>27</b>
2.1	Survey of Experimental Work . . . . .	27
2.1.1	Device Development Programs . . . . .	27
2.1.2	Academic CI Research . . . . .	29

2.1.3	Longitudinal Wave Experiments . . . . .	29
2.1.4	Cylindrical Wave Experiments . . . . .	31
2.2	The Case for Heidmann’s Experiment . . . . .	32
2.3	Model Problem: Spinning Wave . . . . .	36
2.3.1	Description of Experiment . . . . .	36
2.3.2	Data Analysis of Spinning Wave . . . . .	39
2.4	Summary . . . . .	41
<b>3</b>	<b>Theory 1: Energy Cascade</b>	<b>42</b>
3.1	Theory . . . . .	42
3.2	Physical Explanation . . . . .	43
3.2.1	Amplitude Energy Balance . . . . .	44
3.2.2	Burnley’s Optimal Energy Transfer . . . . .	44
3.2.3	Extended Energy Balance . . . . .	45
3.3	Procedure . . . . .	46
3.3.1	Selection of Modes . . . . .	46
3.3.2	Determining Coefficients . . . . .	47
3.3.3	Solution . . . . .	47
3.3.4	Amplitude vs. Driving . . . . .	48
3.4	Experimental Validation . . . . .	48
3.5	Mode/Harmonic Decomposition . . . . .	51
3.6	Summary . . . . .	51
<b>4</b>	<b>Theory 2: Steepening</b>	<b>53</b>
4.1	Theory . . . . .	53
4.2	Physical Explanation . . . . .	55
4.2.1	Speed-of-Sound and Wave Reflections . . . . .	55
4.2.2	Nonlinear Amplifiers . . . . .	55
4.3	Procedure . . . . .	57
4.3.1	Numerical Solutions . . . . .	57
4.3.2	Amplitude vs. Epsilon . . . . .	57
4.4	Experimental Validation . . . . .	59
4.5	Mode/Harmonic Decomposition . . . . .	61
4.5.1	Assumption Examined . . . . .	62
4.6	DC Valley . . . . .	65
4.7	Summary . . . . .	65



<b>5</b>	<b>Theory 3: Oscillators</b>	<b>68</b>
5.1	Theory . . . . .	68
5.1.1	Expansion . . . . .	68
5.1.2	Governing Equations . . . . .	69
5.2	Physical Explanation . . . . .	69
5.2.1	The Harmonic Cascade . . . . .	70
5.2.2	Generalization . . . . .	72
5.3	Procedure . . . . .	72
5.3.1	Driving vs. Amplitude . . . . .	73
5.4	Experimental Validation . . . . .	74
5.5	Mode/Harmonic Decomposition . . . . .	76
5.5.1	Assumption Examined . . . . .	76
5.6	DC Valley . . . . .	80
5.7	Summary . . . . .	80
<b>6</b>	<b>Theory 4: CFD</b>	<b>82</b>
6.1	Theory . . . . .	82
6.1.1	Governing Equations . . . . .	82
6.1.2	Numerical Approach . . . . .	82
6.2	Procedure . . . . .	83
6.2.1	Solver Development . . . . .	83
6.2.2	Test Case Development . . . . .	84
6.2.3	Mesh Refinement . . . . .	87
6.2.4	Initial Conditions vs. Amplitude . . . . .	89
6.3	Experimental Validation . . . . .	90
6.4	Mode/Harmonic Decomposition . . . . .	92
6.4.1	Procedure . . . . .	92
6.4.2	Assumption Examined . . . . .	96
6.5	DC Valley . . . . .	96
6.6	Summary . . . . .	97
<b>7</b>	<b>Conclusions</b>	<b>99</b>
7.1	Rediscovering Heidmann . . . . .	99
7.2	The Why of Cylindrical Harmonics . . . . .	99
7.3	Mode/Frequency Assumption . . . . .	100
7.4	DC Valley . . . . .	100
7.5	Expanded State-of-the-Art . . . . .	101

7.6 Future Work . . . . .	101
<b>Bibliography</b>	<b>103</b>
<b>Appendices</b>	<b>108</b>
<b>A Energy Balance: Derivation</b>	<b>109</b>
A.1 Variables and Expansions . . . . .	110
A.2 Defining Equations . . . . .	110
A.3 Finalized Energy Balance . . . . .	113
A.3.1 1st Order Energy . . . . .	113
A.3.2 2nd Order Energy . . . . .	113
A.3.3 3rd Order Energy . . . . .	114
A.4 Cylinder Mode Assumptions . . . . .	114
A.5 Acoustic Decomposition . . . . .	115
A.6 Source: Driving Work . . . . .	115
A.7 Sink: Viscous Boundary Layer Losses . . . . .	116
A.8 Sink: Compressive Viscous Losses . . . . .	117
A.9 Dynamic Model . . . . .	117
<b>B Steepening: Alternate Wave Equation Derivation</b>	<b>118</b>
B.1 Governing Equations . . . . .	118
B.2 Potential Flow . . . . .	120
B.3 Wave Equation . . . . .	120
<b>C Example Nonlinear Oscillator Simulation</b>	<b>122</b>
<b>D Decomposition Examples</b>	<b>132</b>
<b>Vita</b>	<b>137</b>

# List of Tables

1.1	Sample set of harmonics . . . . .	15
1.2	Natural frequencies of a cylinder . . . . .	16
2.1	Heidmann experiment parameters . . . . .	36
2.2	Summary of Heidmann experiment cases . . . . .	38
3.1	Comparison of energy balance to experiment . . . . .	51
3.2	Decomposition coefficients for energy balance . . . . .	52
4.1	Comparison of Maslen/Moore to experiment . . . . .	61
4.2	$a_{nm}$ decomposition coefficients for Maslen/Moore . . . . .	63
4.3	$b_{nm}$ decomposition coefficients for Maslen/Moore . . . . .	64
5.1	Comparison of oscillator theory to experiment . . . . .	76
5.2	$a_{nm}$ decomposition coefficients for nonlinear oscillators . . . . .	77
5.3	$b_{nm}$ decomposition coefficients for nonlinear oscillators . . . . .	78
6.1	Comparison of CFD to experiment . . . . .	93
6.2	$a_{nm}$ decomposition coefficients for CFD . . . . .	95
6.3	$b_{nm}$ decomposition coefficients for CFD . . . . .	95
A.1	Additional variables and their defining equations. . . . .	111
A.2	The thermodynamic relations. . . . .	112
A.3	Assumptions and expansions applied to $\vec{W}_2$ . . . . .	116

# List of Figures

1.1	An F-1 engine instability . . . . .	2
1.2	Longitudinal geometry . . . . .	5
1.3	Longitudinal mode shapes . . . . .	7
1.4	Time history of one longitudinal mode . . . . .	8
1.5	Circular geometry . . . . .	10
1.6	Circular mode shapes . . . . .	11
1.7	Comparison of sloshing and spinning modes . . . . .	13
1.8	Prediction of Corporal data . . . . .	20
2.1	Timeline of large liquid rocket programs . . . . .	28
2.2	Saenger's steepened pressure traces . . . . .	30
2.3	Temkin's steepened harmonics . . . . .	30
2.4	Jacob's measured mean pressure shift . . . . .	31
2.5	Caap and Mokewitz's radial mode shape . . . . .	32
2.6	Phillips' chamber response . . . . .	33
2.7	Heidmann's apparatus . . . . .	33
2.8	Heidmann's chamber response . . . . .	34
2.9	Heidmann 1T test cases . . . . .	37
2.10	Heidmann mean pressure variance . . . . .	38
2.11	Determining horizontal axis . . . . .	39
2.12	Determining vertical axis . . . . .	39
2.13	Digitized data reviewed . . . . .	40
3.1	Nonlinear energy cascade in amplitude . . . . .	45
3.2	Sample amplitude equations from Mathematica . . . . .	48
3.3	Minimum and maximum pressures of energy balance solution . . . . .	49
3.4	Peak-to-peak amplitudes of energy balance solution . . . . .	49
3.5	Pressure-time comparison of energy balance prediction to experiment . . . . .	50
4.1	Longitudinal/planar steepening diagram . . . . .	56

4.2	Turn-scattering of an acoustic pulse . . . . .	56
4.3	Numerical issues with Maslen/Moore's solution . . . . .	58
4.4	Minimum and maximum pressures of Maslen/Moore solution . . . . .	58
4.5	Peak-to-peak amplitudes of Maslen/Moore solution . . . . .	59
4.6	Pressure-time comparison of Maslen/Moore analytic prediction to experiment . . . . .	60
4.7	Energy error of Maslen/Moore prediction . . . . .	65
4.8	DC Valley in Maslen/Moore . . . . .	66
5.1	Minimum and maximum pressures of oscillator solution . . . . .	73
5.2	Peak-to-peak amplitudes of oscillator solution . . . . .	74
5.3	Pressure-time comparison of nonlinear oscillator prediction to experiment . . . . .	75
5.4	Error energy of oscillator prediction . . . . .	79
5.5	1R component of oscillator simulation . . . . .	80
6.1	Sod shock problem verification: nondimensional pressure . . . . .	84
6.2	Sod shock problem verification: nondimensional density . . . . .	85
6.3	Sod shock problem: nondimensional pressure surface . . . . .	85
6.4	Sod shock problem: nondimensional density surface . . . . .	86
6.5	Sod shock problem: nondimensional x-velocity surface . . . . .	86
6.6	Example CFD time trace . . . . .	87
6.7	Example CFD mode shape . . . . .	88
6.8	Mesh independence of final spatial pressure distribution . . . . .	89
6.9	Mesh independence of pressure-time solution . . . . .	90
6.10	Diagram of CFD initial conditions . . . . .	91
6.11	Minimum and maximum pressures of CFD solution . . . . .	91
6.12	Peak-to-peak amplitudes of CFD solution . . . . .	92
6.13	Pressure-time comparison of CFD prediction to experiment . . . . .	93
6.14	Error energy in CFD prediction . . . . .	97
6.15	DC valley in CFD results . . . . .	98
C.1	The complete, superposed solution: (a) time snapshot of limit cycle mode shape; (b) time dependence at the wall for the complete simulation; (c) the limit cycle pressure-time wave as observed at a wall station. . . . .	123
C.2	Oscillator simulation, modes 1 through 6 . . . . .	124
C.3	Oscillator simulation, modes 7 through 12 . . . . .	125
C.4	Oscillator simulation, modes 13 through 18 . . . . .	126
C.5	Oscillator simulation, modes 19 through 24 . . . . .	127

C.6	Oscillator simulation, modes 25 through 30 . . . . .	128
C.7	Oscillator simulation, modes 31 through 36 . . . . .	129
C.8	Oscillator simulation, modes 37 through 42 . . . . .	130
C.9	Oscillator simulation, modes 43 through 44 . . . . .	131
D.1	System that meets mode/harmonic approximation . . . . .	132
D.2	System that does not meet mode/harmonic approximation . . . . .	133
D.3	System that approximately matches mode/harmonic assumption . . . . .	134
D.4	System with error quantified . . . . .	135

# Nomenclature

$0R, 1R, 2R, \dots$  indicates a cylindrical mode with a specified number of nodal circles (the “radial” mode number)

$0T, 1T, 2T, \dots$  indicates a cylindrical mode with a specified number of nodal diameters (the “azimuthal” or “tangential” mode number)

$\alpha_n$  growth constant for mode  $n$  in linear combustion instability theory

$\delta(m)$  Dirac delta distribution,  $\delta(m) = 1$  if  $m = 0$ ;  $\delta(m) = 0$  if  $m \neq 0$

$\delta_{nm}$  Kronecker delta function,  $\delta_{nm} = \delta(n - m)$

$\zeta_n$  direct-driving coefficient for mode  $n$

$\epsilon$  a small ( $\epsilon \ll 1$ ) dimensionless parameter wherever it appears

$\eta_n(t)$  the (arbitrary) time dependence function governing a particular mode  $n$

$\gamma$  ratio of specific heats,  $C_p/C_v$

$\kappa$  thermal conductivity

$\kappa$  wave number,  $f t^{-1}$  or  $m^{-1}$

$\lambda_{nm}$   $m^{\text{th}}$  root of the  $n^{\text{th}}$  Bessel function’s derivative,  $J'_n(r)$

$\mu$  shear viscosity, kinematic viscosity

$\zeta$  bulk viscosity, second coefficient of viscosity

$\Phi$  velocity potential,  $\vec{u} = -\nabla\Phi$

$\phi_n$  phase of oscillation for  $n^{\text{th}}$  mode

$\psi_n(\vec{r})$  spatial mode shape for the  $n^{\text{th}}$  mode

$\rho$  density (mass per unit volume)

$\tau$  period of oscillation, seconds

$\theta$	azimuthal coordinate variable in circular or cylindrical coordinates
$\omega$	frequency of oscillation, radians per second
$a$	speed of sound
$a_{nm}$	decomposition coefficient; shows the $n^{\text{th}}$ mode / $m^{\text{th}}$ harmonic / $\sin(m\omega t)$ contribution to a total solution
$b_{nm}$	decomposition coefficient; shows the $n^{\text{th}}$ mode / $m^{\text{th}}$ harmonic / $\cos(m\omega t)$ contribution to a total solution
$e$	internal energy, or energy of heat, per unit mass
$f$	frequency of oscillation, in Hz (cycles per second)
$h$	enthalpy (per unit mass)
$J_n$	$n^{\text{th}}$ Bessel function of the first kind
$L$	length of longitudinal geometry, ft or m
$\Delta p$	peak-to-peak pressure amplitude, $\Delta p = p_{\max} - p_{\min}$ , psi
$\frac{\Delta p}{p_0}$	relative peak-to-peak pressure amplitude
$p$	pressure
$P_{ij}(r)$	functions determined from inhomogeneous Bessel equations for Maslen/Moore's solution to the strong cylindrical wave problem
$R$	radius of a cylindrical cavity
$r$	radial coordinate variable in circular or cylindrical coordinates
$R_n$	amplitude of oscillation for $n^{\text{th}}$ mode
RMS Error	a metric for quantifying the difference between two sets of numbers, e.g., an experimental data set across a set of points, and predicted values at those same points
$s$	entropy (per unit mass)
$T$	temperature
$t$	time, seconds
$\vec{u}$	fluid velocity
$x$	axial distance coordinate in cylindrical coordinates, ft or m
$()_0$	when applied to fluid dynamic variables, indicates mean values that are constant or slowly-varying in time



$\phi_1, \phi_2, \dots$  when applied to fluid dynamic variables, indicates progressively smaller unsteady corrections to the mean flow variables

$\hat{\phi}$  unit vector in the  $\phi$  direction (e.g.,  $\hat{r}$  for radial unit vector,  $\hat{n}$  for a unit normal vector)

$\phi_i, \phi_f$  values at initial and final time, respectively

$\phi_{nml}$  indicates a third-rank coupling coefficient matrix, usually for nonlinear coupling of modes

$\nabla$  vector differential operator;  $\nabla \cdot$  =divergence, etc.

# Chapter 1

## Introduction

The study of strong pressure waves in cylinders is motivated by combustion instabilities, which are unwanted pressure waves in continuous flow propulsion and power conversion devices. The study of combustion instability, in turn, is motivated by the desire for better propulsion and power conversion devices.

High-power-density internal-flow devices are pervasive throughout the world today. Most commercial aircraft use them: turbofan engines, turbojet engines, and afterburners. All space launch vehicles use them: solid rocket motors and liquid rocket engines. The majority of electricity used today is produced with them: gas turbines for natural gas, and steam turbines for coal and nuclear. Modern society depends on rockets, jets, and turbines to maintain a fleet of communications, navigation, and weather observation satellites; to keep homes and businesses lit and warm; to travel for business and pleasure.

As with many technologies, the rockets, jets and turbines available today could be used without improvement. But there is strong economic motivation for improving these devices. The increasing and volatile costs of energy drive engineers to design higher-performance power plants and aircraft engines. A rising international concern with environmental impact drives the development of low-emission devices. The need to replace an aging fleet of navigation and weather satellites, combined with the incredible cost per launch, drives engineers to find ways to squeeze more performance out of rockets. With this aggressive pursuit of improved devices comes large, expensive development programs, which have high risks of unexpected combustion instabilities.

This generates a desire to predict and understand combustion instabilities as cheaply and reliably as possible. Through the use of fluid dynamics, thermodynamics, and chemistry, it is possible to create theories for predicting these instabilities. The present work is part of the effort to improve the theories, by examining one class of poorly understood phenomena: the nonlinearity of strong waves in cylindrical geometries.

### 1.1 The Combustion Instability Problem

*Combustion instabilities* (CIs), also called *thermo-acoustic instabilities*, are a class of phenomena common to nearly all high-power-density internal-flow devices. They often present themselves as an oscillating pressure wave inside the

device. Combustion is not a requirement to observe these instabilities. However, since flow energy is required to drive oscillations, combustion devices (with their high power density) are more susceptible to these instabilities than other internal flow devices.

The pressure oscillations of combustion instabilities often create problems. In some cases, they directly induce mechanical vibrations in surrounding structures that can have catastrophic effects (such as guidance system failures or severe tissue damage to passengers), costly effects (such as lowering the lifetimes of expensive turbine components), or possibly no significant effect at all (depending on how severe the vibration is). In other cases, the pressure oscillations can couple to thrust production, causing more severe vibrations.

The F-1 engine of the Saturn V launch vehicle is often used as the canonical case-in-point of combustion instability. During its development, an instability was observed with pressure wave amplitudes in excess of 1000 psi over the mean pressure of 5000 psi, as shown in Figure 1.1. The vibration environment would have incapacitated the astronauts and disabled the guidance system, and possibly would have caused structural weakening or failure. Over 2700 full-scale firings were performed in a test program that is valued at billions of US dollars today [1].

Combustion instabilities (CIs) are potential problems for any engine and turbine development program. Despite more than half a century of research, CIs remain unpredicted nearly every time they occur. Mitigation efforts rarely succeed simply, quickly, or cheaply, primarily due to the lack of reliable tools to predict or analyze CIs. Programs have been cancelled when CIs were observed in test articles, for fear of budget overruns and schedule slips (e.g. Sargent, see [2]). Program managers are very wary of CIs, preferring to avoid systems that have the slightest history of instability. CIs can occur at almost any phase of a system's life cycle; they have appeared years after the deployment of a missile system (Minuteman II stage 3, see [2] [3]).

A reliable and relatively inexpensive method for understanding, predicting and mitigating CIs is highly desirable for future engine development. To this end, an energy balance theory has been developed which may ultimately deliver this inexpensive, reliable engineering prediction and analysis tool. [4] The present work helps extend and validate the nonlinear portion of this theory in the high-amplitude regime for nontrivial geometries. Though ultimately focused on one particular class of waves—strong cylindrical waves, as described in Section 1.2—the present work develops

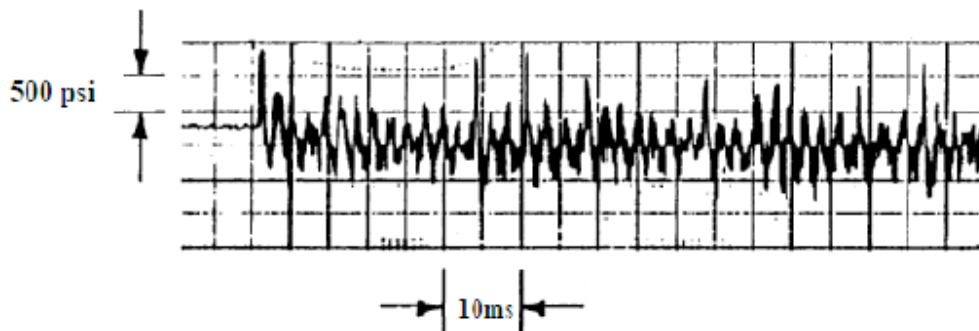


Figure 1.1: An F-1 engine instability [1].

techniques that apply generally to more complicated geometries.

## 1.2 Strong Cylinder Waves

Combustion instabilities are *standing waves* in a *compressible fluid* within a contained geometry. There are many types of fluid dynamic waves possible in chambers, including: *pressure waves*, *vorticity waves*, and *entropy waves*. Though each type of wave is labelled with only one of the fluid dynamic variables, all three wave types involve oscillations in several variables. This work will use the term *pressure wave* to refer to irrotational oscillations between the pressure and velocity variables.<sup>1</sup>

Here, interest is focused on the strong pressure waves of cylindrical geometries. Understanding these waves begins with understanding three things:

- standing weak pressure waves theory (the theory of acoustic resonances);
- standing weak pressure waves in cylinders (the acoustic resonances of cylinders);
- strong pressure waves.

This section presents an overview of the essential concepts from traditional acoustics, and introduces much of the notation important to combustion instability theory.

### 1.2.1 Standing Pressure Waves

To understand strong cylinder waves, it is first necessary to understand weak pressure waves. Weak pressure waves are experienced as sound. Lord Rayleigh laid out the connection between the two phenomena (pressure and sound) in his Theory of Sound [5].

The theory of weak pressure waves, or *acoustic theory*, begins with the theory of gas dynamics, i.e., compressible fluid flow in a gas. The fluid motion is described in Eulerian terms by specifying the fluid velocity at each point in space and time,  $\vec{u}(\vec{r}, t)$ , and a complete set of thermodynamic properties at every point in space and time: density  $\rho(\vec{r}, t)$ , temperature  $T(\vec{r}, t)$ , and pressure  $p(\vec{r}, t)$ . These variables are governed by fluid dynamic conservation laws (conservation of mass, momentum, and energy), as well as thermodynamic equations of state describing how the medium responds to changes in pressure and temperature.

Under certain assumptions (ideal gas, irrotational flow, negligible heat conduction and viscosity), the governing equations can be reduced to a single equation governing one scalar variable, such as pressure  $p$ , speed of sound  $a$ , or velocity potential  $\Phi$  (with  $\vec{u} = -\nabla\Phi$ ). Enflo [6] derives this equation in terms of  $\Phi$  as

$$\frac{\partial^2}{\partial t^2} \Phi - a_0^2 \nabla^2 \Phi = \frac{\partial}{\partial t} \left[ (\nabla\Phi \cdot \nabla\Phi) + \frac{\gamma - 1}{2a_0^2} \left( \frac{\partial\Phi}{\partial t} \right)^2 \right] \quad (1.1)$$

where  $\rho_0$  is the average density,  $\gamma$  is the ratio of specific heats of the gas, and  $a_0$  is the average speed of sound (as given by  $a_0^2 = \gamma RT_0$  with  $R$  the specific gas constant of the fluid).

<sup>1</sup>The combustion instability community often uses the term “acoustic” to refer to this kind of wave, but “acoustic” implies that the waves are weak, where combustion instabilities can be very strong waves.

Acoustic theory makes one further assumption: the wave is “weak”. This is equivalent to saying that the variation of fluid properties due to the wave is much smaller than the average value of those fluid properties. With  $p_0$  the average pressure,  $p_{max}$  and  $p_{min}$  the maximum and minimum pressures, the weak assumption states:

$$\frac{\Delta p}{p_0} = \frac{p_{max} - p_{min}}{p_0} \ll 1 \quad (1.2)$$

Under this assumption, Equation 1.1 becomes the wave equation of classical acoustics (for details, see e.g. Rayleigh [5]):

$$\frac{\partial^2}{\partial t^2} \Phi - a_0^2 \nabla^2 \Phi = 0 \quad (1.3)$$

This is the traditional form of a linear wave equation. Solutions to this equation break down, broadly, into two categories. The first is *travelling waves* in free space. Most acoustic theory is concerned with waves of this type: pressure waves as *radiation*. In theories of radiation, waves begin at a source, propagate away from that source, and decay. Sometimes waves interact with material transitions, causing reflections, refractions, and transmissions. Waves are considered to be propagating through a space much larger than the wave.

The second class of solutions to the wave equation are *cavity waves*.<sup>2</sup> These waves are confined in some way, and the geometry of constraint dictates what kinds of waves are possible. Combustion instabilities are pressure waves confined to combustion chambers or other internal flow geometries, and are thus closely related to the weak cavity waves of classical acoustics.

When a wave is strictly confined, some set of surfaces do not allow the fluid to flow freely. For these irrotational pressure waves, the no-slip condition cannot be enforced consistently. Instead, the normal component of the fluid velocity vector must vanish ( $\vec{u} \cdot \hat{n} = 0$ , with  $\hat{n}$  the unit normal vector), meaning that the fluid cannot flow through the surfaces of the cavity. This sets up the boundary value problem:

$$\frac{\partial^2}{\partial t^2} \Phi - a_0^2 \nabla^2 \Phi = 0 \quad (1.4)$$

$$\hat{n} \cdot \nabla \Phi = 0 \quad \text{along the boundaries} \quad (1.5)$$

This boundary value problem is an eigenvalue problem. For a given geometry, only kinds of certain solutions are allowed (called the eigenmodes, natural modes, or simply *modes*), and those solutions have a well-defined frequency of oscillation (called the eigenfrequency or *resonant frequency*).<sup>3</sup>

To see how these modes and resonant frequencies arise, consider the *longitudinal* geometry. The longitudinal geometry is any 3D geometry which has one long dimension, and which has a constant cross-sectional area and shape along that dimension. Examples include tubes, slab-shaped solid rocket motors, and long boxes. Figure 1.2 shows a typical geometry with length  $L$ , demonstrating the 1-D coordinate system in  $x$  with bounds at  $x = 0$  and  $x = L$ . For

<sup>2</sup>Section 1.2.4 will explore the distinction between “cavity” and “chamber”. Here, the physics usage of “cavity” is used to denote “the geometry containing the primary wave”.

<sup>3</sup>This remains true for more general boundary conditions, so long as the boundary conditions constrain the system.

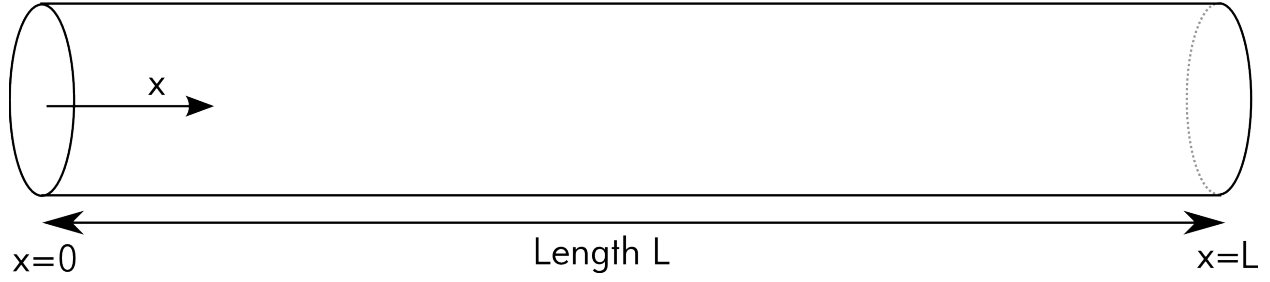


Figure 1.2: Longitudinal geometry

these geometries, modes in the longitudinal direction are governed by the one dimensional wave equation:

$$\frac{\partial^2}{\partial t^2} \Phi - a_0^2 \frac{\partial^2}{\partial x^2} \Phi = 0 \quad (1.6)$$

$$\frac{\partial \Phi}{\partial x} \Big|_{x=0} = \frac{\partial \Phi}{\partial x} \Big|_{x=L} = 0 \quad (1.7)$$

This equation can be solved by a separation of variables, assuming  $\Phi(x, t) = X(x)Y(t)$ :

$$\frac{\partial^2}{\partial t^2} (XY) - a_0^2 \frac{\partial^2}{\partial x^2} (XY) = 0 \quad (1.8)$$

$$X \frac{\partial^2 Y}{\partial t^2} - a_0^2 Y \frac{\partial^2 X}{\partial x^2} = 0 \quad (1.9)$$

$$\frac{1}{Y} \frac{\partial^2 Y}{\partial t^2} - \frac{a_0^2}{X} \frac{\partial^2 X}{\partial x^2} = 0 \quad (1.10)$$

$$(1.11)$$

With the first term dependent only on time, and the second dependent only on space, each term must be equal to the same constant (which is selected to be the square of an unknown constant  $\omega$ ):

$$\frac{1}{Y} \frac{\partial^2 Y}{\partial t^2} = \omega^2 \quad (1.12)$$

$$\frac{1}{X} \frac{\partial^2 X}{\partial x^2} = \frac{\omega^2}{a_0^2} \equiv \kappa^2 \quad (1.13)$$

Both these equations have sine and cosine solutions, with a frequency  $\omega$  for the time-dependence and a wave number  $\kappa$  for the space-dependence. Therefore, the total solution is given by:

$$\Phi(x, t) = X(x)Y(t) \quad (1.14)$$

$$= (A \cos(\kappa x) + B \sin(\kappa x))(C \cos(\omega t) + D \sin(\omega t)) \quad (1.15)$$

Thus far,  $\omega$  and  $\kappa$  are unconstrained, except that  $\omega = a_0\kappa$ . Applying the boundary condition at  $x = 0$ :

$$\begin{aligned}\frac{\partial\Phi}{\partial x}(x = 0, t) &= (-\kappa A \sin(\kappa 0) + B\kappa \cos(\kappa 0))(C \cos(\omega t) + D \sin(\omega t)) \\ &= B\kappa(C \cos(\omega t) + D \sin(\omega t)) \\ &= 0\end{aligned}$$

requiring  $B = 0$ . Then applying the boundary condition at  $x = L$ :

$$\begin{aligned}\frac{\partial\Phi}{\partial x}(x = L, t) &= (-\kappa A \sin(\kappa L))(C \cos(\omega t) + D \sin(\omega t)) \\ &= 0\end{aligned}$$

If  $A \neq 0$  (as required for a nontrivial solution), then  $\sin(\kappa L) = 0$ , which requires that  $\kappa L = n\pi$  for some nonnegative integer  $n$ . Negative integers would be allowed, but do not give unique solutions:  $\sin(-n\pi x/L) = -\sin(n\pi x/L)$ , which can be absorbed into the nonnegative  $n$  solutions. Absorbing the constant  $A$  into  $C$  and  $D$ , the complete solutions becomes (with  $\tau_n$  the period of oscillation):

$$\begin{aligned}\Phi_n(x, t) &= \cos(\kappa_n x) (C \cos(\omega_n t) + D \sin(\omega_n t)) \tag{1.16} \\ \omega_n &= \frac{n\pi a_0}{L} \\ \tau_n &= \frac{2\pi}{\omega_n} \\ \kappa_n &= \frac{\omega_n}{a_0} = \frac{n\pi}{L} \\ n &= 0, 1, 2, 3, \dots\end{aligned}$$

The *mode shapes* are the spatial distribution functions corresponding to each mode; in this case,  $\cos(\kappa_n x)$ . At any given point in time, the distribution of pressure through the chamber will look like the mode shape times some constant. Figure 1.3 shows the shapes for several modes, and Figure 1.4 shows the time variation of one of those modes.

Since governing Equation 1.7 is linear, the *superposition principle* applies: if  $\Phi_A$  and  $\Phi_B$  are solutions, so then so is  $C_A\Phi_A + C_B\Phi_B$  for any two constants  $C_A, C_B$ . Therefore, the complete solution to the longitudinal wave is

$$\Phi(x, t) = \sum_{n=0}^{\infty} \cos(\kappa_n x) (C_n \cos(\omega_n t) + D_n \sin(\omega_n t)) \tag{1.17}$$

where  $C_n, D_n$  describe the *amplitude* and *phase* of each mode. The solution can be rewritten

$$\Phi(x, t) = \sum_{n=0}^{\infty} R_n \cos(\kappa_n x) \cos(\omega_n t + \phi_n) \tag{1.18}$$

where now  $R_n$  is the amplitude, and  $\phi_n$  the phase, of each mode.

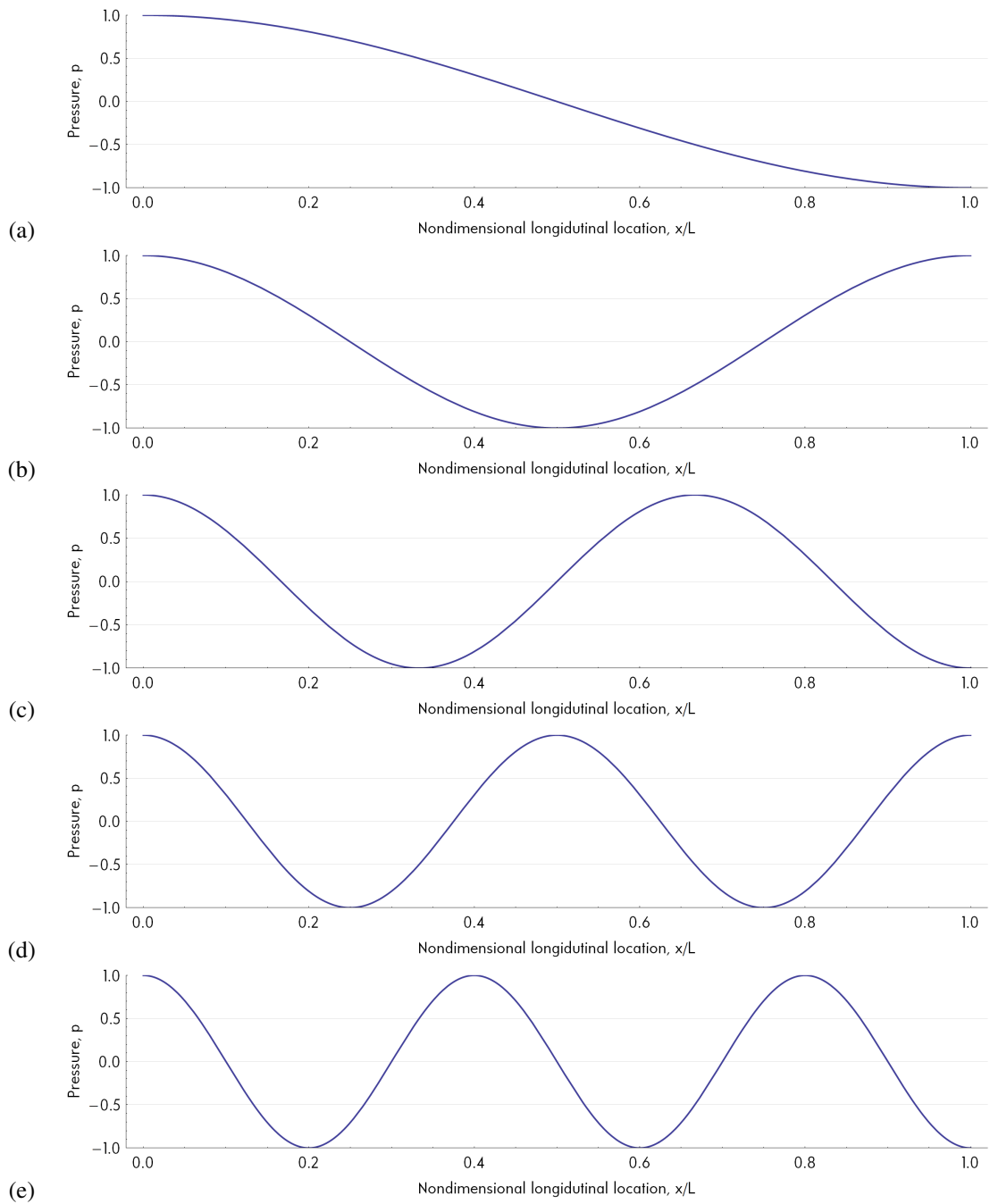


Figure 1.3: Longitudinal modes shapes for the first five modes of a long thin cavity. (a) Mode 1, (b) Mode 2, (c) Mode 3, (d) Mode 4, (e) Mode 5.



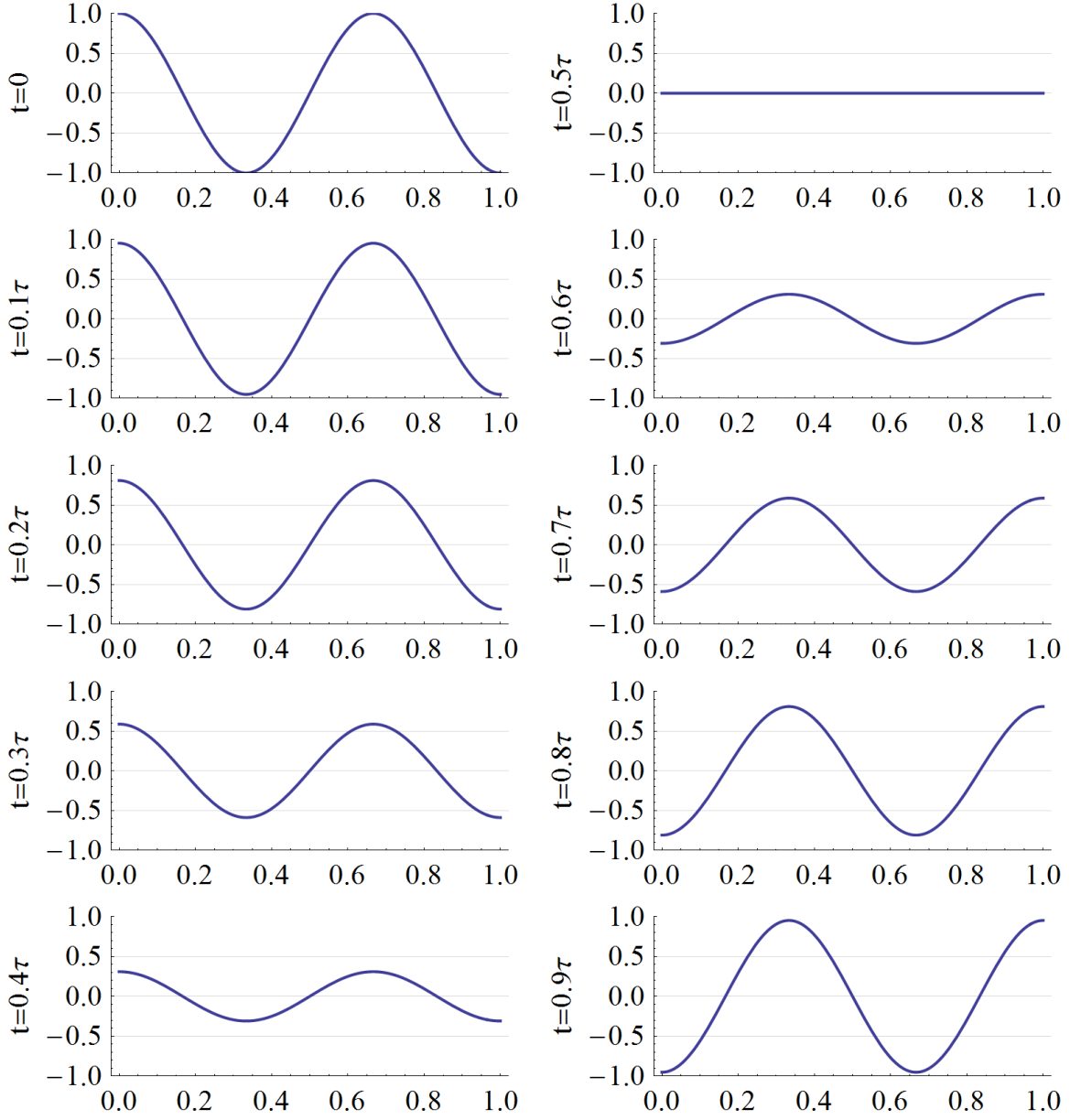


Figure 1.4: Time history of the  $3^{rd}$  longitudinal mode. Vertical axis is pressure, horizontal axis is nondimensional longitudinal coordinate  $x/L$ .  $\tau$  is the period of oscillation, and individual plots are labelled by the time offset from the top-left figure.

Although this solution is in terms of an abstract concept—the velocity potential  $\Phi$ —the physical variables, pressure and velocity, related by:

$$p(x, t) = -\rho_0 \frac{\partial \Phi}{\partial t} = \rho_0 \sum_{n=0}^{\infty} \omega_n \cos(\kappa_n x) (C_n \sin(\omega_n t) - D_n \cos(\omega_n t)) \quad (1.19)$$

$$\vec{u}(x, t) = -\nabla \Phi = \sum_{n=0}^{\infty} \kappa_n \sin(\kappa_n x) (C_n \cos(\omega_n t) + D_n \sin(\omega_n t)) \hat{x} \quad (1.20)$$

This longitudinal example models an important geometry that is seen in real world problems. It contains features common to all geometries (mode shapes, resonant frequencies, superposition). But most real world problems contain (at minimum) a more complicated transverse geometry which has its own resonant mode solutions. In many cases, as in the case studied here, that transverse geometry is circular.

## 1.2.2 Cylinder Waves

Liquid rocket combustion chambers, turbojet afterburners, and turbine combustors are most commonly circular in cross-section. The acoustic mode structure of cylinders is different from that of boxes.

As with longitudinal modes, the modes of circular cavities are derived using the acoustic wave equation confined to a particular geometry. Figure 1.5 shows such a geometry with radius  $R$ , for a polar coordinate system in  $r$  and  $\theta$ . In this geometry, the boundary value problem of Equation 1.5 becomes:

$$\frac{\partial^2}{\partial t^2} \Phi - a_0^2 \left( \frac{1}{r} \frac{\partial}{\partial r} \left( r \frac{\partial \Phi}{\partial r} \right) + \frac{1}{r^2} \frac{\partial^2 \Phi}{\partial \theta^2} \right) = 0 \quad (1.21)$$

$$\hat{r} \cdot \left( \frac{\partial \Phi}{\partial r} \hat{r} + \frac{1}{r} \frac{\partial \Phi}{\partial \theta} \hat{\theta} \right) \Big|_{r=R} = 0 \quad (1.22)$$

An additional boundary condition arises from the requirement that the solution be continuous in  $\theta$ , given  $\theta$  as a periodic coordinate variable:

$$\Phi(r, \theta) = \Phi(r, \theta + 2\pi n), \quad n \text{ an integer} \quad (1.23)$$

A similar procedure of separation of variables, followed by the application of boundary conditions, again results in an eigenvalue problem. The detailed derivation can be found in, e.g., Arfken and Weber [7], and results in a sinusoidal equation in  $t$ , a sinusoidal equation in  $\theta$ , and a Bessel equation in  $r$ . The mode shapes that satisfy these equations are

given as:

$$\Phi_{n,m}(r, \theta, t) = \begin{cases} (A \sin(\omega_{nm}t) + B \cos(\omega_{nm}t) \cos(n\theta))J_n(\lambda_{nm}r/R) \\ (A \sin(\omega_{nm}t) + B \cos(\omega_{nm}t) \sin(n\theta))J_n(\lambda_{nm}r/R) \end{cases} \quad (1.24)$$

$$n = 0, 1, 2, \dots \quad \text{azimuthal mode number} \quad (1.25)$$

$$m = 0, 1, 2, \dots \quad \text{radial mode number} \quad (1.26)$$

$$\frac{\partial J_n}{\partial r}(\lambda_{nm}) := 0 \quad \lambda_{nm} \text{ is defined as the } n^{\text{th}} \text{ root of } J'_n \quad (1.27)$$

$$\omega_{nm} = \frac{a_0 \lambda_{nm}}{2\pi R} \quad \text{the resonant frequency (in radians per second)} \quad (1.28)$$

$$f_{nm} = \frac{\omega_{nm}}{2\pi} \quad \text{the resonant frequency (in Hertz)} \quad (1.29)$$

$$\tau_{nm} = \frac{1}{f_{nm}} \quad \text{the period of oscillation (in seconds)} \quad (1.30)$$

The two mode numbers,  $n$  and  $m$ , have a geometric significance. The *azimuthal* mode number  $n$  (the *tangential* mode number to the CI community) indicates the number of nodal diameters: lines across the chamber where the pressure does not change. The *radial* mode number  $m$  indicates the number of nodal circles: circular lines where the pressure does not change. A particular circular mode is often referred to as, for instance, the “1T 2R” mode, meaning it has  $n = 1$  and  $m = 2$ . Figure 1.6 shows the pressure distributions associated with the several of these circular modes.

Note in Equation 1.24 that both  $\sin(n\theta)$  and  $\cos(n\theta)$  distributions are possible for a particular set of mode numbers  $n, m$ . This is often referred to as a spatial *degeneracy*, as there are two distinct modes that can ring at the same frequency (the term arises from the study of matrix eigenvalues, see e.g. Arfken and Weber [7]). If two degenerate modes are ringing 90 degrees out-of-phase with each other, a special condition is set up where the mode shape appears

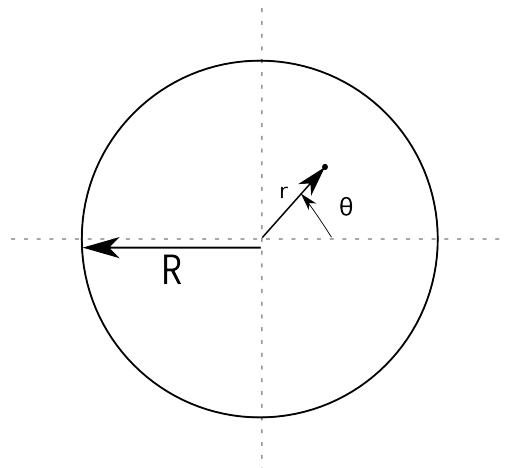


Figure 1.5: Circular geometry

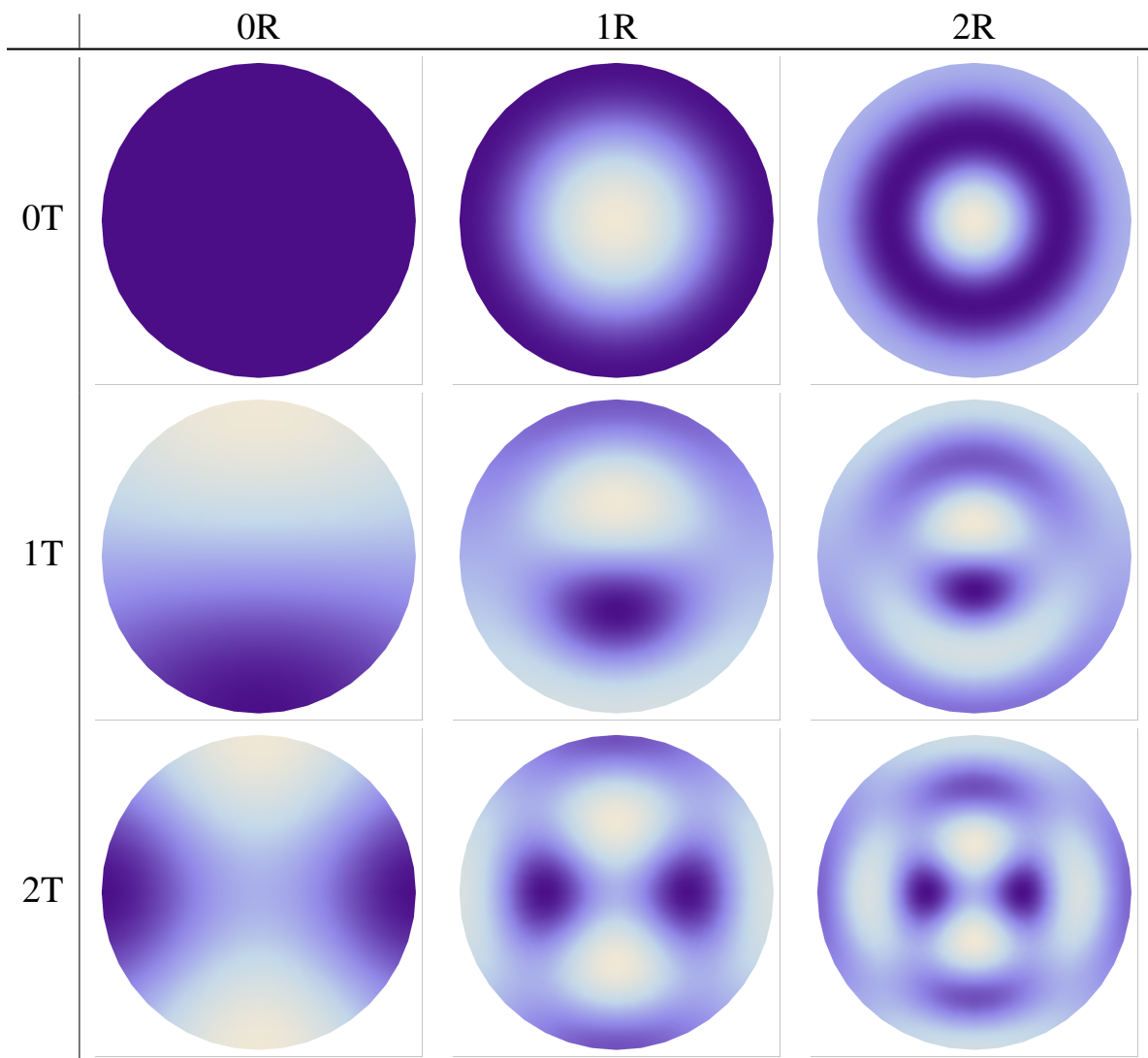


Figure 1.6: Circular mode shapes, showing the pressure distribution across the circular chamber for different values of the two mode numbers

to spin or travel around the chamber. For the 1T modes, the solution becomes:

$$\Phi_{1T,0R}(r, \theta, t) = J_n(\lambda_{10}r/R) \cos(\theta + \omega_{10}t) \quad (1.31)$$

Figure 1.7 shows a comparison of the two types of waves.

Although it is useful to use the space/time separated decomposition of Equation 1.24, another decomposition is possible where the degeneracy is handled by one “traveling mode”  $\cos(n\theta + \omega_{nm}t)$  and one “sloshing mode” ( $\cos(n\theta)\cos(\omega_{nm}t)$ ) for each set of mode numbers. The two descriptions of the mode structure are mathematically equivalent. The spinning/sloshing description is perhaps more useful for understanding observed phenomena qualitatively; the sloshing/sloshing description is often more useful for calculations as it contains a complete space/time variable separation.

The mode shapes laid out in this section are called the *linear* or *acoustic* mode shapes, as they are the solutions to the linear acoustic problem of Equation 1.5. One of the essential assumptions of this problem, and therefore of these solutions, is that the wave amplitudes are weak. However, waves in many devices are strong enough to violate that assumption. This leads to so-called “strong” pressure waves.

### 1.2.3 Strong Waves

*Strong waves*, also called *finite amplitude* waves, are waves whose amplitudes are large enough for nonlinear gas dynamic effects to become apparent. These nonlinear effects distort the wave shapes. In free plane waves, this leads to “N-waves”, or shocks [6]. A similar shock-shape is seen when longitudinal modes reach high amplitudes [8].

The traditional explanation for this phenomena comes from a consideration of the speed-of-sound across a wave. For very weak waves, the speed of sound is nearly constant throughout the wave. But for strong waves, the temperature and speed-of-sound significantly deviate from their mean values. The parts of the wave with higher speed-of-sound “catch up” to the slower regions, until the wave becomes a travelling weak shock instead of classical acoustic wave. This process is called *steepening*.

The CI community has developed some alternate explanations for this process, and they are described in Section 1.3.

### 1.2.4 Some Issues with Terminology

Combustion instabilities are *standing gas dynamic waves* within a contained geometry. Two distinct communities work on such phenomena, and they have two distinct terminologies. Acousticians have one set of terms, often inherited from the physics community. Combustion instability experts, on the other hand, inherit much of their terminology from the propulsion community. The overloading of terms can cause confusion, so some clarifications are needed.

As mentioned before, three kinds of waves can occur. The kind described in Section 1.2 are irrotational waves in (primarily) pressure and velocity. Though the waves can, at high enough amplitudes, induce variations in temperature, entropy, and speed-of-sound, those effects are secondary to the pressure/velocity effects. Often, the CI community use

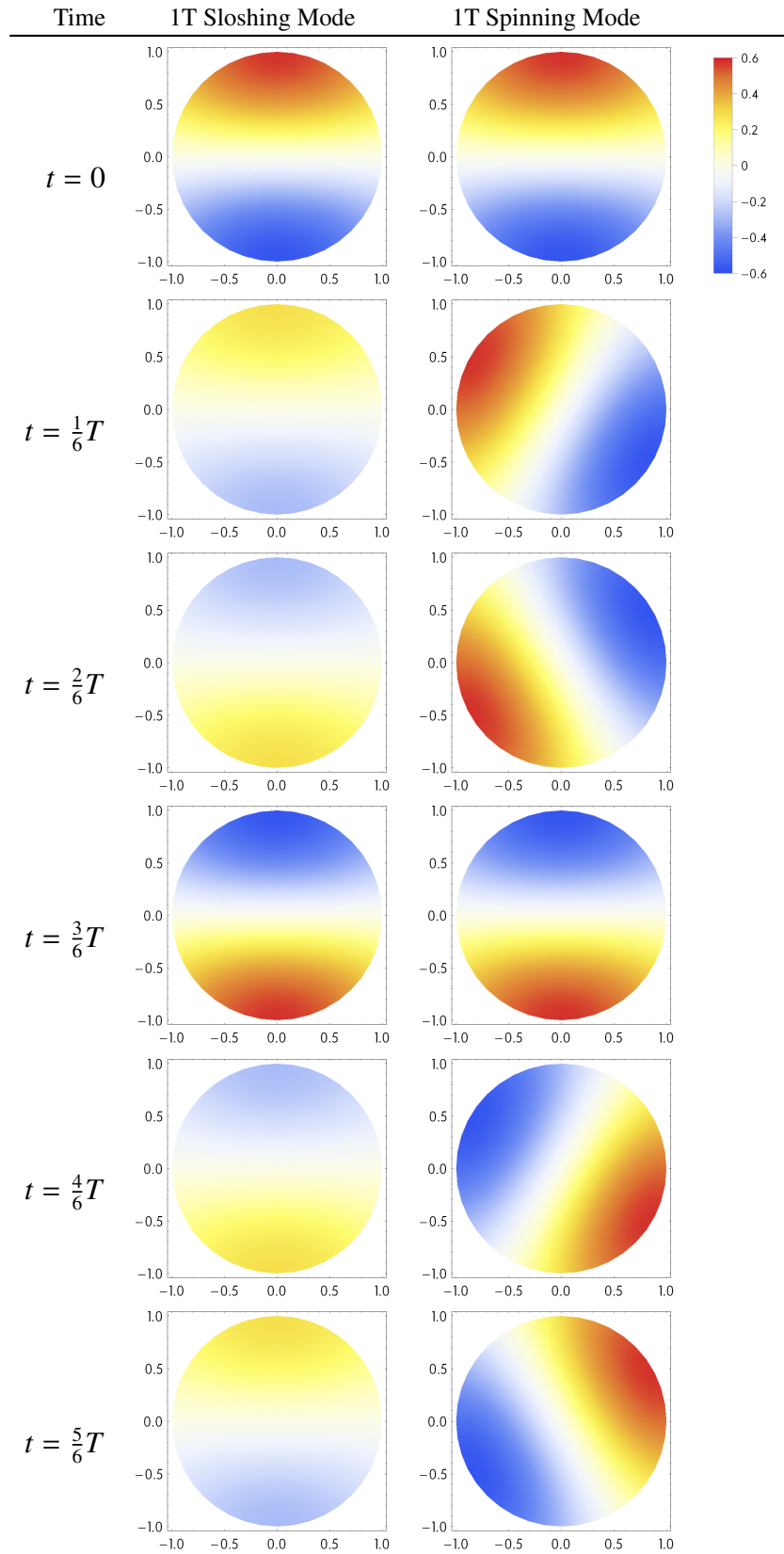


Figure 1.7: Comparison of sloshing and spinning modes. Surface height is proportional to pressure deviation from normal for a unit wave as described in Equation 1.24 with  $B = 1, A = 0$ .

the term “acoustic wave” to denote these irrotational pressure/velocity waves. But “acoustic” denotes weak waves in the acoustics community, even in so-called “nonlinear acoustics”, yet the irrotational pressure/velocity waves discussed here can have very high amplitudes. Since this type of wave can be described by just one fluid variable, and since the other wave types have little or no direct effect on pressure, these waves are referred to in the present work as *pressure waves*.

Physicists (and acousticians) refer to contained and standing waves as “cavity waves”, as in Section 1.2 above. In propulsion terminology, however, the term “cavity” often refers to devices that are secondary to the main geometry (Helmholtz resonator “cavities”, for instance). From this point on, the term “cavity” will be avoided, and “chamber” will be used for the primary wave containing geometry.

Acousticians regularly deal with “traveling waves”, by which they mean plane (or spherical, or cylindrical) waves propagating through free space. Occasionally they work with “standing waves”, which are confined waves in chambers. As the CI community rarely works with free waves, propulsion analysts are more likely to use the term “traveling wave” to refer to the “spinning wave” solutions in cylindrical geometries, and “standing wave” to refer to “sloshing modes” (see Section 1.2.2). Here, the terms *spinning* and *sloshing* are used to refer to the two different types of cylindrical waves, and *standing* and *travelling* are used to describe radiation waves and waves in chambers, respectively.

In the combustion instability community, *transverse waves* are standing waves transverse to the direction of mean flow. In a typical rocket or jet, the mean flow travels axially down the cylindrical chamber. These waves are therefore sloshing across the cylinder or travelling around the rim. In the CI literature, the terms “transverse waves” and “*tangential waves*” are used nearly interchangeably to refer to the azimuthal and radial modes of a cylindrical geometry. However, in acoustics literature (for example, the 3D acoustics work done by Coppens et al. [9]), “transverse” simply means “transverse to the longest chamber direction” and can refer to any geometry (a rectangular box, for instance). To avoid confusion, the terms “transverse” and “tangential” will be avoided. “Cylindrical waves” and “cylindrical modes” will be used to refer to standing waves and modes specific to cylindrical geometries: the radial and azimuthal modes.

In propulsion, modes that slosh along the direction of mean flow are called *axial modes*. This generally aligns with the acoustics community usage: “axial” being “the direction along the longest chamber dimension”. Sometimes, however, both communities use the term “axial mode” to refer to the one dimensional Cartesian solution (the solution laid out in Section 1.2.1). Some propulsion systems and acoustic chambers have constant area along one dimension, but many do not. Yet these still have “axial modes” in the sense of “sloshing modes along the direction of mean flow” or “sloshing along the longest chamber direction”. Hereafter, as in Section 1.2.1, the term *longitudinal modes* will be used to describe 1-D Cartesian solutions, and “axial” will be reserved for more general geometries.

Finally, it is important to have clearly defined distinctions between the terms “harmonics”, “overtones” and “resonance frequencies”. *Overtones* and *harmonics* are defined relative to some *fundamental* frequency  $f$ . Overtones are any frequencies higher than the fundamental that appear in a signal. Harmonics are special overtones that are integer multiples of the fundamental frequency:  $2f, 3f, 4f$ , et cetera. Note that the  $n^{\text{th}}$  harmonic of a frequency is actually  $(n + 1)f$ , as a frequency is not considered a harmonic of itself. Harmonics arise naturally from any periodic function

Table 1.1: Sample set of harmonics

Harmonic	Frequency	Multiplier
fundamental	44 Hz	1
1	88 Hz	2
2	132 Hz	3
3	176 Hz	4
4	220 Hz	5

through Fourier analysis. Any sufficiently well-behaved periodic function<sup>4</sup> can be decomposed into a superposition of sines and cosines ringing at harmonics of the fundamental frequency (the inverse of the period of the function). Table 1.1 shows a list of harmonics of a fundamental frequency.

In contrast, a *resonance frequency* is defined relative to a particular geometry under particular mean conditions. A resonance is a mode solution of the linear acoustics problem of Section 1.2, with an associated resonance frequency, or *natural frequency*. The natural frequencies of the longitudinal geometry are the first mode’s frequency and its harmonics. The cylindrical geometry does not have this property, as shown in Table 1.2.

### 1.3 State of the Art

The propulsion research community has been actively pursuing a means of predicting and modelling combustion instabilities for the better part of a century. At present, several approaches are used to model and analyze combustion instabilities.

Some working groups pursue direct computational fluid dynamic (CFD) solutions for particular systems (e.g., Xia [10]). With modern advancements in computer hardware and recent developments in CFD theory, these solutions are increasingly accurate. However, accurate solutions for turbulent, combusting devices are still expensive, often requiring months on supercomputer-grade hardware. Those solutions, once acquired, are device and condition specific, allowing diagnostics of only one particular system under one particular set of operating conditions. Moreover, CFD provides no direct information on what is causing the instability, just an “answer” to whether a particular setup exhibits an instability. This limits the applicability of this technique to very large programs or dedicated research projects.

Several working groups pursue models based upon classical acoustic modes. These are often described as “analytical models” or “analytical frameworks”, though all employ various numerical techniques. There are two primary approaches, a nonlinear wave equation method and an unsteady energy balance method. Both employ a procedure pattern similar to this:

- Compute the linear acoustic modes and frequencies of the system.
- Identify all physical processes that can drive / damp acoustic vibration.
- For each mode: sum all the damping and driving processes to determine *linear stability*.

---

<sup>4</sup>One sufficient condition is: the function is continuous at all but a finite number of points.



Table 1.2: Natural frequencies of a cylinder. The multiplier is the ratio of the mode’s frequency to the 1T 0R mode frequency.

Mode number	Frequency	Multiplier
1T 0R	2025 Hz	1
2T 0R	3360 Hz	1.66
0T 1R	4215 Hz	2.08
1T 1R	5865 Hz	2.90
2T 1R	7377 Hz	3.64
0T 2R	7717 Hz	3.81
etc.		

- Use a nonlinear model to *couple* the modes together and determine *limit cycle* behaviour.

For a detailed overview of this procedure, the reader is referred to the AGARD text of Culick [3]. The unsteady energy balance method makes fewer assumptions than the nonlinear wave equation approach, and thus captures more effects. The combustion instability community primarily uses one of these approaches in the practical diagnostics of real systems, as they require less computational resources and often offer greater insight into the causes of instability.

Recently, one group has applied the techniques of CFD to a single-variable nonlinear wave equation [11]. This approach models the physical processes that can damp or drive acoustic waves in much the same way as the analytic models. However, instead of performing the various calculations outlined above, the system is directly modeled numerically using a finite-difference technique. This approach shows some promise, though its results are as yet preliminary.

### 1.3.1 CFD Instability Modelling

There are too many recent papers on CFD models for particular instability problems to detail them all. One working group’s work will be considered as indicative of the current state-of-the-art in CFD CI models: the Purdue group working jointly on a single-element combustor experiment and a detailed CFD model of the same experiment [10].

At present, the working group has produced repeatable experimental data for the high-frequency instability of a combustor, and several CFD solutions. The final CFD model, a three-dimensional, turbulent, combusting DES-like simulation, compared well against the experiment, and showed most if not all the major behaviors observed in the experiment. The work shows how it is possible to achieve a very accurate solution accounting for all effects.

However, the work also shows how much effort is required to achieve that solution for a system with multiple time and space scales (associated with multiple physical processes). The simulations required several months of computer time on a 100-600 processor computer cluster.

### 1.3.2 Linear Combustion Instability Theory

Linear combustion instability theory uses the experimental observation that combustion instabilities appear at acoustic mode frequencies and have spatial distribution similar to acoustic modes. This observation was quantified over the years, as various experiments were performed that measured mode shapes as well as frequencies.

The linear theory begins with a modal decomposition of the chamber which experiences an instability. The theory assumes that any “instabilities” are, in fact, acoustic modes being driven by some process. The oscillating pressure is assumed to be

$$p_1(\vec{r}, t) = p_0 \sum_n R_n(t) \sin(\omega_n t + \phi_n) \psi_n(\vec{r}) \quad (1.32)$$

where  $\psi_n$  and  $\omega_n$  correspond to an acoustic mode,  $p_0$  is the mean chamber pressure,  $R_n$  is the amplitude of oscillation of each mode  $n$ , and  $\phi_n$  is the phase of each mode. The  $R_n$  and  $\phi_n$  are allowed to change in time (as chamber conditions change, etc.).

The various theories proceed in various ways, either with unsteady energy balances (Flandro et al. [4]) or with inhomogeneous wave equations (Culick et al. [12], Crocco et al. [13]). These theories each capture different effects, but at a certain point they all proceed in roughly the same way to roughly the same results. The unsteady pressure expansion, along with expansions for the other field variables in terms of  $R_n, \psi_n, \omega_n$ , are inserted into governing equations. Various techniques such as Galerkin, spatial averaging, and time averaging are employed. The complicated physical processes are all reduced to a single equation for each mode that are given as:

$$\frac{dR_n}{dt} = \left( \sum_m \alpha_{n,m} \right) R_n \quad (1.33)$$

Each  $m$  on the right hand side corresponds to a physical process, such as viscosity, nozzle damping, or pressure-coupling to the combustion process. Collapsing the sum to a single number  $\alpha_n$ ,

$$\frac{dR_n}{dt} = \alpha_n R_n \quad (1.34)$$

the solution becomes

$$R_n(t) = e^{\alpha_n t}. \quad (1.35)$$

If  $\alpha_n$  is negative, then any disturbances will decay away exponentially, and mode  $n$  is called *linearly stable*. If  $\alpha_n$  is positive, then disturbances will grow exponentially, and the mode is termed *linearly unstable*. Assuming all sources of driving and damping can be accounted for, then adjusting various device parameters to make a mode linearly stable will guarantee that any disturbance will decay. For this reason, the majority of research in the combustion stability world has focused on identifying these sources and sinks of unsteady energy. However, if a mode is not linearly stable, the linear theory predicts unbounded growth. Nature does not permit unbounded growth, which leads to nonlinear combustion instability theory.

### 1.3.3 Nonlinear Combustion Instability Theory

Linear CI theory will predict the stability of a mode, if and only if all effects are captured correctly. Jacob has shown how nonlinear interactions can cause the linear theory to give incorrect conclusions regarding experiments [14]. Without the ability to validate against experiments, CI theories will continue to be murky at best. Therefore, a full understanding of the nonlinear effects is required.

The linear assumption of acoustics fails if a mode is unstable, because the amplitude of a disturbance becomes large and the linear theory no longer applies. If the procedure described for the linear CI theory is repeated, but with nonlinear gas dynamics included, then terms will appear that couple the modes together. Jacob [15] derives these terms as:

$$\frac{dR_n}{dt} = \alpha_n R_n + \sum_m \sum_l E_{nml} R_m R_l \quad (1.36)$$

This model describes the nonlinear steepening of a wave as a “cascade” of energy to other modes. As one mode rises in amplitude, it starts to drive other modes, which in turn drive (or damp) other modes. Most modes are linearly stable (as viscosity is always present), so the energy cascades through the system until the nonlinear driving/damping of each mode balances against the linear driving/damping. This condition, where none of the amplitudes are changing significantly in time, is called a *limit-cycle*. Accurately predicting the limit-cycle amplitudes of each mode is the goal of the nonlinear theory of combustion instability.

Note that this approach to the nonlinear behaviour continues to make the assumption that the linear acoustic mode shapes, with simple sinusoidal time dependence, are able to capture the nonlinearity. This leads to the first of two questions addressed in the presented work:

1. How much error is created by the mode/frequency assumption of Equation 1.32?

This theory was used with moderate success over the years to produce two- or three-mode approximations to various solutions. In the past decade Flandro, French, and Jacob have successfully incorporated many more modes into numerical simulations [16] [17] [18]. Wilson and Jacob recently validated this nonlinear model quantitatively against experiment, showing that the model can predict limit cycle amplitudes and spectra of longitudinal waves [19] [20].

Part of the success of the longitudinal predictions, however, came from two properties of longitudinal modes coinciding. Experimentally, finite-amplitude waves in longitudinal geometries steepen into shock-like shapes, i.e., a periodic waveform that (when decomposed with a Fourier analysis) contains a certain harmonic structure relative to the fundamental frequency. Because the natural frequencies of the chamber and harmonics of the wave are the same, the decomposition of Equation 1.32 is both easy-to-use and effective.

The natural frequencies of cylindrical modes are *not* harmonically related, yet experimental evidence (see Chapter 2) shows that the limit-cycles of strong, cylindrical waves are periodic, with harmonics of the fundamental frequency. This leads to the other principal question investigated in this work:

2. Why do waves steepen into apparent harmonics, despite the natural resonances being nonharmonic?

### 1.3.4 Strong Cylindrical Instabilities

Steepened cylindrical waves look very different from steepened longitudinal waves (see Chapter 2). The nonlinear theory predicts that energy cascades from one mode into higher modes. However, the resonant frequencies of cylindrical modes are not integer harmonics of each other. Traditional CI theories perform a simple time average of the governing equations and prevent reconciling the nonharmonic natural frequencies to the harmonic frequencies observed in experiments.

The oldest and best known attempt to model steepened cylindrical waves is the seminal paper by Maslen and Moore in 1956 [21]. Before the development of CI theory (both linear and nonlinear) as it is practiced today, Maslen and Moore used a perturbation method to obtain a solution for isentropically steepened cylindrical waves. The solution was thorough and widely accepted, but quantitative experimental validation was not reported in the literature.

Various descendants of Crocco have worked on the problem. Zinn and Powell used two- and three-mode approximations [22], and relaxed the assumptions regarding the time dependence of each mode. They obtained reasonable results, although unlike Maslen and Moore's. Culick [12], Yang [23] and Burnley [24] developed a general nonlinear equation governing an arbitrary number of modes, which they implemented for a small number of modes (less than 5). French [16] incorporated Burnley's nonlinear analysis into the Standard Stability Prediction (SSP) code, and was able to show many modes locking onto harmonics of the primary instability. None these studies were compared with experiment to determine whether it accurately captured limit-cycle spectra and amplitudes.

Flandro and Jacob were the first to compare waveforms quantitatively against experiment [18]. In modelling the Corporal rocket engine as tested at Caltech, Jacob was able to show agreement between theory and experiment in growth-rate, limit-cycle amplitude, and limit-cycle waveform shape [25]. Figure 1.8 shows those results. That work assumed, with some motivation from experiment, that the traditional cylindrical modes rang at integer multiples of the first mode's natural frequency. This assumption led to excellent results, and partially motivated the present work to fully reconcile theory and experiment.

## 1.4 New Contributions

The goal of the present work was originally to address two questions concerning steepened cavity waves in cylinders.

1. Why do waves steepen into apparent harmonics, despite the natural resonances being nonharmonic?
2. How much error is created by the mode/frequency assumption of Equation 1.32?

The current state-of-the-art had several open problems that were addressed in the present work. First, the theories that might address the questions were lacking in experimental validation. Second, no clear consensus had emerged for how and why cylindrical waves steepen. Third, it was unclear from the experiments whether the harmonics have shifted mode-shapes, or whether the classical acoustic mode shapes still apply. These were all successfully addressed in this dissertation.

As the work progressed, two additional contributions emerged. First, an experiment performed in the 1960s at NASA Lewis was discovered that seems to have been overlooked for its importance to the theory of strong waves.

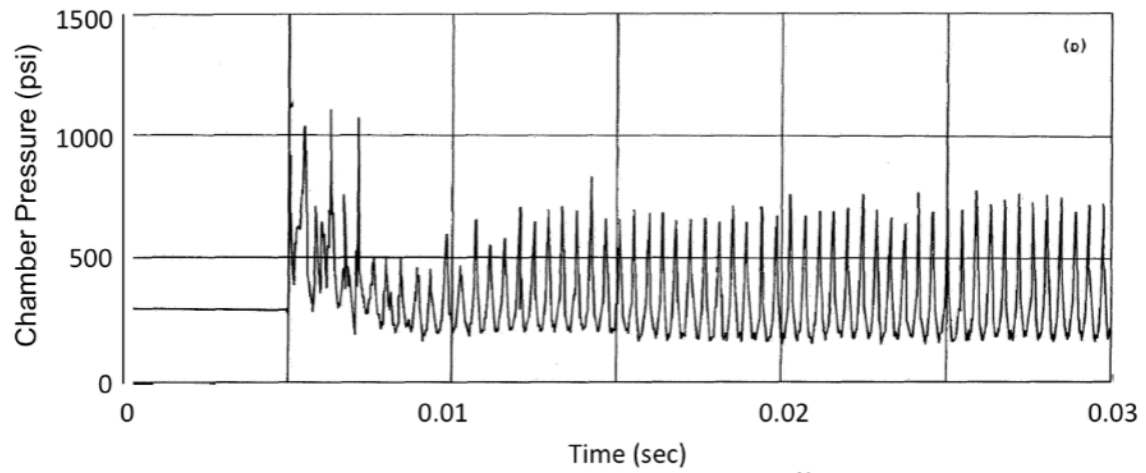


Figure 10. RMIR Corporal pressure data<sup>20</sup>

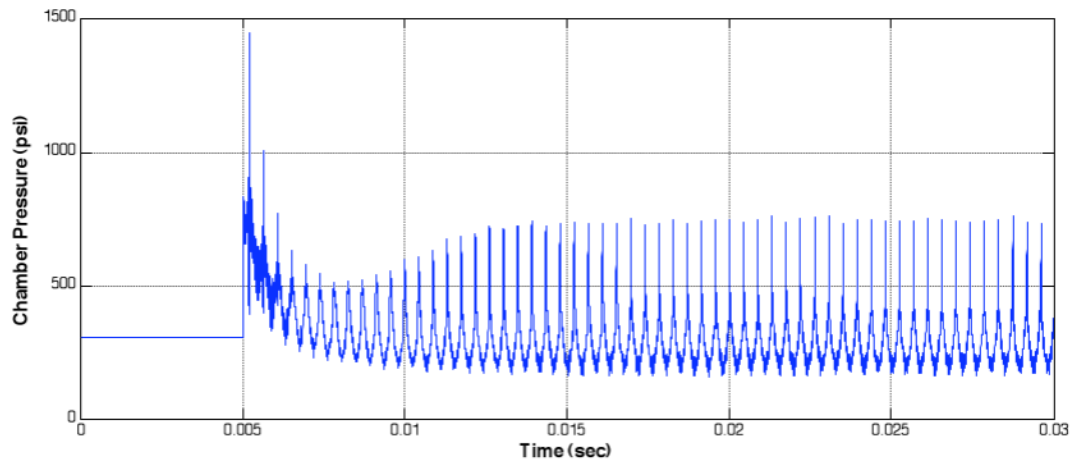


Figure 11. UCDS recreation of RMIR Corporal pressure data

Figure 1.8: Prediction of Corporal data by Jacob [25]

Second, a spatially-dependent but time-independent (zero-frequency) pressure shift was confirmed in several theories, a phenomenon which would appear to have importance for the interpretation of experimental data but which seems to have been overlooked by the community.

### 1.4.1 Experiment

In an effort to assure that any theoretical developments explored would be connected to physical reality, experimental validation was pursued for all models used. Different data sets were explored, and one experiment was located which had all the properties of steepened cylindrical waves (see Chapter 2). This experiment was used as the problem modeled with each theory, and the experimental data used to validate each theory.

The experiment, performed by Heidmann at NASA Lewis in the 1960s [26], has not been discussed in the literature. Yet the experiment exhibited all the hallmarks of an excellent diagnostic experiment: high repeatability, excellent range of variable parameters, exhibits behaviors only usually seen sporadically in more complex systems. Upon closer inspection, the experiment seemed to have produced the highest (fractional) amplitude pressure waves ever created. Chapter 2 explores why this experiment might have been overlooked, and why it could be valuable to the CI community going forward.

### 1.4.2 Why Waves Steepen

No consensus had previously emerged for why and how cylindrical waves steepen to have harmonics. This is partly explained by the differences among the various theories. Three theories offer three different explanations, and *each explanation is correct*. This is similar to the differences among the theories of motion: force balance (Newtonian), conservation (energy/momentum), action minimization (Lagrangian). All correctly describe the motion of particles, but each offers a different explanation for “how” and “why”.

Some analogous happens with steepening theories. The theory of steepening by wave distortion into a changed periodic shape was given by Maslen and Moore [21]. Flandro and Jacob have developed the energy balance model to include frequencies, which explains mode frequency shift as a form of energy storage similar to mode amplitude [15]. The nonlinear oscillator equations of Crocco et al. [13] and Culick et al. [12] [23] [24] admit of another explanation, which has not been explored before: a “harmonic cascade” through nonlinearly coupled harmonic oscillators. All three explanations, two given by others and one given here for the first time, are presented in their respective Chapters (3, 4 and 5).

### 1.4.3 The Mode/Frequency Assumption

The traditional decomposition of combustion stability theory is Equation 1.32, repeated here:

$$p_1(\vec{r}, t) = p_0 \sum_n R_n(t) \sin(\omega_n t + \phi_n(t)) \psi_n(\vec{r}) \quad (1.37)$$

Applying this decomposition to the nonlinear theory assumes two things.

First, the nonlinearity only acts to change the amplitudes and phases, not the mode shape. It is important to note that Maslen and Moore assumed the exact opposite: that the nonlinearity acts to shift the shape of one mode, and does not couple the modes.

Second, the nonlinearity acts to change the amplitudes, frequencies and phases, but does not change the shape of the time dependence. Though experiment suggests that the total time dependence must be periodic, it does not guarantee that each mode is ringing at only one frequency. Each mode could have content at multiple harmonics of the fundamental frequency. This violates the linear acoustic equation—where the speed of sound locks each mode shape onto a single corresponding frequency. But nonlinearity often introduces new frequencies into problems.

To examine these questions, four theories were used:

1. An energy balance model due to Flandro and Jacob (Chapter 3);
2. Maslen and Moore’s perturbation technique (Chapter 4);
3. A nonlinear oscillator theory due to Culick (Chapter 5);
4. A finite volume CFD solver (Chapter 6).

The first theory makes the traditional assumption—that the solution can be represented with a superposition of acoustic modes ringing at single frequencies—and was able to predict the waveform shape for each of the experimental test cases reasonably well. The three other theories do not make the assumption, and were therefore used to determine whether the assumption leads to errors. The errors associated with the assumption were found to be low over a wide range of wave amplitudes.

#### **1.4.4 DC Shift Valley**

An effect in nonlinear signal processing is *DC shift*. The term derives from “direct current” (DC) and “alternating current” (AC), terms that refer to steady and oscillating electric signals. In electronics, an oscillating (AC) signal passing through a nonlinear system will have its harmonic content altered as well as a steady offset—the “DC shift”. The term is used in the CI community to refer to a change in mean chamber pressure during an instability.

While verifying that the decomposed solutions correctly recomposed back to the same solution, a result was observed that was not anticipated at the outset of this research. The recomposed solutions were incomplete; there was a consistently different shape to the original solution. It was determined that the difference was due to a zero-frequency (or time-independent) spatially distributed offset to the solution. This offset was the first radial mode times a negative constant, making it a valley shape.

It became clear that this effect is present in all theories that allow it. Maslen and Moore’s solution includes a radially dependent function in the second order. The nonlinear oscillator solution permits arbitrary time functions, and the first radial mode’s time dependence include a constant offset. The CFD solution certainly permits constant spatial distributions, and when the decomposition takes zero-frequency components into account, the DC valley appears.

However, the literature is nearly silent about this feature of steepened cylindrical waves. Maslen and Moore’s solution, though widely cited, was never numerically evaluated for particular systems, so it seems likely no one realized the valley feature existed. The nonlinear oscillator approach was nearly always applied with a small number of

modes (which rarely if ever includes radial modes) and often assumed a sinusoidal dependence for the modes included. Perhaps CFD solutions have had this feature. However, observing the feature requires a modal decomposition analysis, and has thus never been remarked in CFD solutions.

This feature is examined in more detail in Chapter 7, including ways that this might impact real propulsion systems and what to look for in experimental data.

## **1.5 Summary of Procedure**

This work encompasses many different analytic, numeric and computational techniques. The experiment required specific tools to recover and digitize the test cases. Each of the four theories required their own techniques. The general procedure for each theory was as follows:

1. The model problem was identified.
2. The theory was evaluated for the model problem.
3. Numerical evaluation techniques were set up to simulate the model problem.
4. The dominant model parameter that governs limit-cycle wave amplitude was located.
5. Solutions were obtained for a range of wave amplitudes.
6. Solutions matching the specific wave amplitudes of the test data were located.
7. The theory was validated against the experimental test data.
8. All solutions were decomposed spatially into acoustic modes.
9. For each solution, each spatial mode's time dependence was decomposed into fundamental/harmonic coefficients.
10. An error quantity was evaluated for each solution using its double-decomposition.
11. The solution was investigated for the DC valley component.

### **1.5.1 Model Problem**

The model problem selected was: a spinning 1T mode in a 2D cylindrical geometry. The 1T mode is the most commonly observed cylindrical instability, and data is available for validation of this case. Chapter 2 contains more details for why this was selected as the model problem.

### **1.5.2 Evaluating Theories**

Each of the theories has its own procedure for simulating the model problem. The theories also have different properties that limit the maximum amplitude attainable. These are detailed in the respective chapters for each theory.



### 1.5.3 Experimental Validation

To compare with experiment, each theory was evaluated at conditions which gave a solution whose total wave amplitude ( $p_{max} - p_{min}$ ) matched the amplitude of a known test case. The experimental data considered had five such test cases over a wide range of amplitudes.

In the experimental data, the steepened shape of a wave depended on the amplitude of the wave. To be considered valid for these waves, each theory was required to predict the correct waveform shape. To evaluate the quality of each prediction, the solution was used to plot a pressure-versus-time curve at the spatial location corresponding to the experimental data, which was jointly plotted. This provided a means of visually comparing the two predictions and determining whether the solution was lining up with experiment.

Additionally, the solutions were evaluated at every point in time available for each test case. The fractional RMS error of solution against experiment was calculated for each test case:

$$\text{RMS Error}_{\text{experiment}} = \frac{1}{N} \sum \left( \frac{p_{\text{experiment}} - p_{\text{solution}}}{p_{\text{experiment}}} \right)^2 \quad (1.38)$$

where  $N$  is the number of data points available for a particular test case. This RMS error quantified the match between experiment and prediction.

### 1.5.4 Mode/Harmonic Decomposition

Once a solution technique was validated, a decomposition was applied to probe the properties of the acoustic modes and harmonics of the system.

The decomposition works as follows: Consider a periodic solution to the boundary conditions  $p(\vec{r}, t)$  such that  $\nabla p \cdot \hat{n} = 0$  along the boundaries. At any given moment in time  $t$ , the solution can be expressed as a decomposition of the acoustic modes  $\psi_n$  (which form an orthogonal basis for the problem) as so:

$$p_1(\vec{r}, t) = \sum_{n=1}^{\infty} \eta_n(t) \psi_n(\vec{r}) \quad (1.39)$$

where  $\eta_n(t)$  is the integral

$$\eta_n(t) = \frac{\int_V p(\vec{r}, t) \psi_n(\vec{r}) dV}{\int_V \psi_n^2 dV} \quad (1.40)$$

So long as these  $\eta_n$  are reasonably well-behaved (continuous at all but a finite or possibly countable number of points) and periodic, they can be decomposed using a discrete Fourier transform:

$$\eta_n(t) = \sum_{m=1}^{\infty} a_{n,m} \sin(m\omega t) + b_{n,m} \cos(m\omega t) \quad (1.41)$$

where  $\omega = 2\pi f$  is the angular frequency corresponding to the original periodic frequency  $f$ . By integrating over the

period  $T = \frac{1}{f}$ , the coefficients are found as

$$a_{n,m} = \frac{\int_T \eta_n(t) \sin(m\omega t) dt}{\int_T \sin^2(m\omega t) dt} \quad (1.42)$$

$$b_{n,m} = \frac{\int_T \eta_n(t) \cos(m\omega t) dt}{\int_T \cos^2(m\omega t) dt} \quad (1.43)$$

which gives a “double-decomposition” of the original solution  $p$ —a representation decomposed in space and time:

$$p_1(\vec{r}, t) = \sum_{n,m=1}^{\infty} (a_{nm} \sin(m\omega t) + b_{nm} \cos(m\omega t)) \psi_n(\vec{r}) \quad (1.44)$$

Each theory yields this decomposition slightly differently. The CFD solution yields discrete space-time data that can be interpolated to a function  $p$ ;  $p$  can then be substituted directly into this procedure and the resulting integrals performed numerically. The perturbation/analytic method of Maslen and Moore allows direct harmonic decomposition, requiring only spatial integrals of certain numerical functions. The nonlinear oscillator approach actually yields the  $\eta_n$  directly, so computing  $a_{nm}, b_{nm}$  requires only the discrete Fourier transform. The energy balance method yields  $a_{nm}, b_{nm}$  directly through the limit-cycle amplitudes and frequencies applied to each spatial mode, though only certain harmonics  $m$  are allowed by the theory (i.e., many of the coefficients are zero by assumption).

### 1.5.5 Error Energy

With this decomposition, the quality of the mode/frequency assumption can be quantified by using energy concepts. For each mode  $n$ , the fraction of energy not in the “dominant” harmonic  $M$  is expressed as

$$Err_n = \frac{\sum_{m \neq M} a_{nm}^2}{\sum_m a_{nm}^2} \quad (1.45)$$

This can be further reduced to a single number: the ratio of energy in nondominant harmonics to the total energy in the system. This, however, requires careful inclusion of some constants. While integrating over the sine/cosine functions produces a single constant that drops out of the equation, the spatial mode shapes are not normalized. So the total error is given as:

$$Err_{\text{harmonics}} = \frac{\sum_m \sum_{n \text{ not dominant}} \left( \int_V \psi_n^2 \right) a_{nm}^2}{\sum_m \sum_n \left( \int_V \psi_n^2 \right) a_{nm}^2} \quad (1.46)$$

This error quantifies the quality of the assumption that each mode is ringing at only one frequency. If this error is zero or small compared with 1, then the assumption was considered to be reasonable.

Similarly, for each harmonic  $m$ , the fractional energy not in the “dominant” mode  $N$  is expressed as

$$E_{m,\text{err}} = \frac{\sum_{n \neq N} a_{nm}^2}{a_{Nm}^2} \quad (1.47)$$

As with the harmonics, this can be reduced to a single error quantity representing the quality of the unshifted-mode-shapes assumption:

$$Err_{\text{mode shapes}} = \frac{\sum_n \sum_{m \text{ not dominant}} \left( \int_V \psi_n^2 \right) a_{nm}^2}{\sum_n \sum_m \left( \int_V \psi_n^2 \right) a_{nm}^2} \quad (1.48)$$

The maximum of these two errors was taken as the error for meeting the combined mode/frequency assumption, as it represents the maximum error of the system with respect to the mode/frequency assumption. This is best understood in the context of a particular system, and several examples are given in Appendix D to demonstrate how this decomposition and energy error work.

## 1.6 Summary of Work

To restate briefly: The desire to use acoustic decompositions in combustion stability theories has generated a tension. Observed cylindrical instabilities show harmonics, but CI theories use the nonharmonic resonant frequencies. The desire to use linear acoustic modes conflicts with observed frequency shifts. The quality of an underlying assumption—that the linear acoustic modes can represent the nonlinear solution—is thus questioned. The general lack of experimental validation of the theories make it difficult to tell where and how the theories require work.

In the present work, several theories were validated against experiment, and used to address the tension between harmonics and resonance frequencies. The quality of the underlying assumption was quantified using these theories, showing the assumption to be valid in a wide range of nonlinear steepened cylindrical waves.

Finally, a time-independent, spatially distributed feature common to several theories was observed. Though it arises from long-standing theories, it has not been remarked upon by the community. Its potential significance as a feature of cylindrical combustion instabilities is noted, including potential consequences to propulsion system design and operation.

## Chapter 2

# Steepened Wave Experiments

Propulsion and power conversion devices, the devices which exhibit combustion instabilities, are a staple of experimental evidence for the phenomenon. The difficulty of interpreting engine data motivated fundamental academic experiments, focused on understanding the physics of the problem rather than producing a commercially viable device. Other experiments relevant to CI were originally motivated by acoustic investigations.

To examine the properties of strong cylindrical waves, it was necessary to locate or create an experiment with detailed measurements of such waves. The experiment needed to be repeatable under well-defined operating conditions, to have sufficient available data, and to exhibit the nonlinear steepening associated with strong cylinder waves.

During a survey of the experimental work related to combustion instability, one such experiment emerged: Heidmann's rotating gas jet [27], discussed in Section 2.2.

## 2.1 Survey of Experimental Work

Experimental work in combustion instability is broadly split into three categories: measurements made during device development programs, focused academic experiments into combustion instability, and acoustics experiments.

### 2.1.1 Device Development Programs

Each industry that is concerned with combustion instability has its own history of experimental observations. Designers of electric power turbines, aircraft jet engines, solid rocket motors and liquid rocket engines work with different devices. Though the theories that govern combustion instability are the same across all devices, the different industries have not always communicated well on the topic.

The work presented here was largely motivated by rocket engine development. Harrje and Reardon reviewed most of that work that relates to liquid rocket engines in the NASA document which established liquid rocket engine instability tests and requirements in 1972 [28]. The F-1 liquid rocket engine is, perhaps, the touchstone of that industry. With a severe instability and an expensive test program, the F-1 engine remains legendary in the combustion instability

community [1].

Unfortunately, nearly all large liquid rocket development programs in the US predate 1990. Sackheim presented a time line of these programs [29], shown in Figure 2.1. The lack of *large* engine development is significant to combustion instability progress. Large engines have lower resonant frequencies than small engines. Lower frequency instabilities are easier to measure, and sometimes high frequency instabilities cause fewer system level problems (no effort is made to measure or understand them).

The available experimental data from programs and experiments before 1990 is sparse at best. There may be several reasons for this. The political environment of the era prevented detailed information on potentially threatening technologies from being published. Data acquisition techniques of the time limited how data could be captured and stored; paper and magnetic tape records may have been accidentally destroyed, thrown out as programs moved on, deteriorated beyond use, or simply lost. Some of this has been documented for particular cases, as Yang and Oefelein did for the F-1 engine [1]. However, most of this is conjecture; the general state of affairs is that the data is simply unavailable with no reasons offered.

Blomshield summarized the historical efforts related to solid rocket motors [2]. Again, many of the development programs predate 1990, with the commensurate lack of available data. Blomshield's review also shows that many of the observed instabilities were intermittent (i.e. non-repeatable).

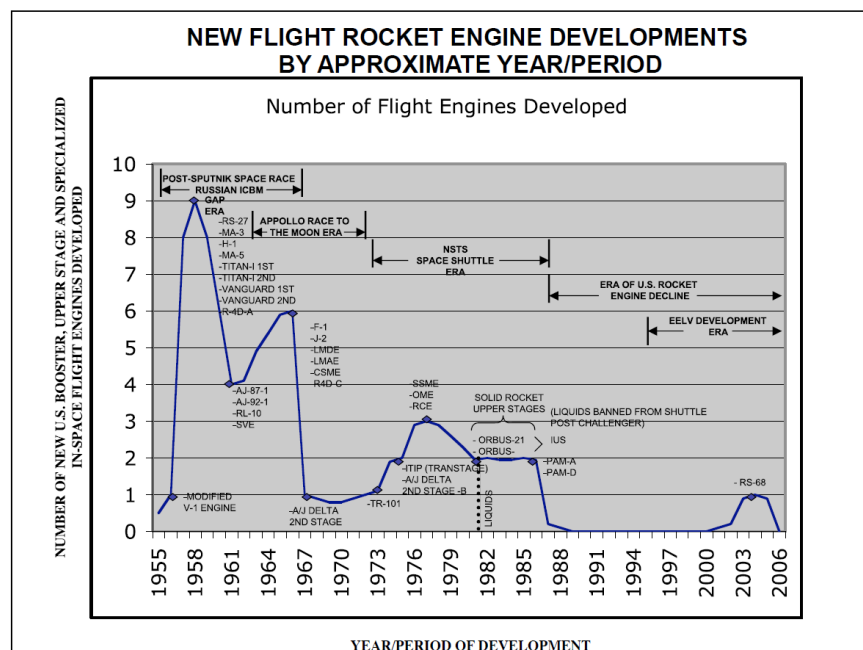


Figure 2.1: Timeline of large liquid rocket programs, from Sackheim [29]

### 2.1.2 Academic CI Research

Some efforts have been made to research combustion instability directly (not as part of an engine development program).

Brownlee and Marble (1959) performed a series of experiments where they achieved repeatable results with tactical-missile size solid rocket motors [30]. Krieg (1964) focused on measuring radial and azimuthal shapes of cylindrical instabilities [31]. Reardon, Harrje, and Crocco (1962) worked to validate the  $n - \tau$  hypothesis, and observed longitudinal, 1T and 2T modes [32]. Swithenbank, Clayton, Sotter (1969) instrumented a Corporal engine and took extensive measurements across the diameter as well as down the length of the engine [33].

Further experimental work has been done in combustion instability, but much or most of it focused on particular aspects: combustors, injectors, acoustic liners, etc. Few full-scale rocket engines have been instrumented for the study of combustion instabilities. Blomshield, who tested full-scale tactical missile motors in the 1990's [34], stands as the primary counterexample to the trend away from testing with full-scale systems.

As with notable engine development programs, most of these efforts were made before 1970. Many of the advancements in combustion instability theory postdate these efforts. The data from these well executed experiments is mostly inaccessible. This state of affairs makes it difficult to validate recent developments in combustion instability theory.

### 2.1.3 Longitudinal Wave Experiments

Though the primary interest here is in cylindrical waves, the evidence of strong longitudinal waves provides a baseline for comparison.

At least as far back as Lord Rayleigh [5], the existence of shocks was predicted. Schlieren photography of attached shocks goes back nearly as far [35]. Saenger presents a history [36], tracing shock wave theory and experiment as far back as the eighteenth century, and therefore that survey will not be repeated here. However, the direct observance of steepened travelling waves requires instrumentation that can capture high-speed transient effects and present them on timescales and spatial scales appropriate to human senses. It was not until the twentieth century that pressure transducers and high-speed recording apparatus allowed direct measurement of unsteady pressure.

In the late 1950's, Saenger drove resonant waves in a long thin tube using a camshaft-piston arrangement [36]. He made high-speed measurements of pressure at several points along the tube, showing the *travelling shock waves* (Figure 2.2) anticipated by Riemann and others.

Temkin expanded the work in the direction of varying amplitudes, using a powerful magnetic driver with a rigid piston [37]. Using a frequency analyzer, he showed that *increasing amplitudes led to more harmonic content*. Figure 2.3 shows the first and second harmonics rising with increased driving amplitude. This data, presented in great detail in a technical contract report [38], has been overlooked for its importance in validating high-amplitude wave theories of all kinds.

Recently, Jacob [20] and Wilson [39] extended this work. Jacob [20] connected the existence of a *DC shift* in a

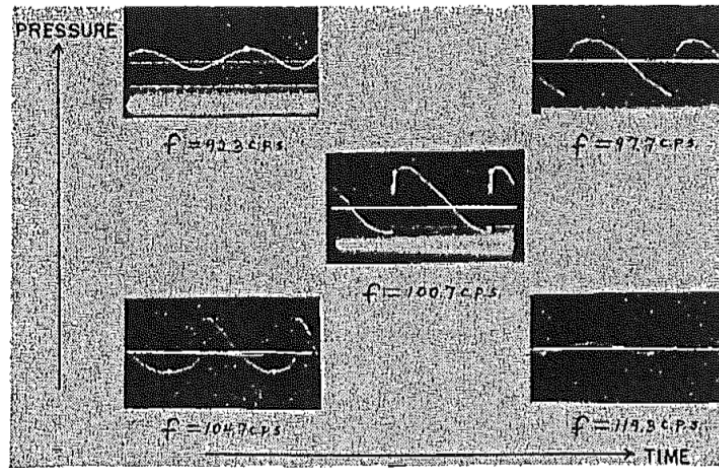


Figure 2.2: Saenger's steepened pressure traces [36]. Each photograph is a plot showing the pressure variation at the end of the tube for different driving frequencies.

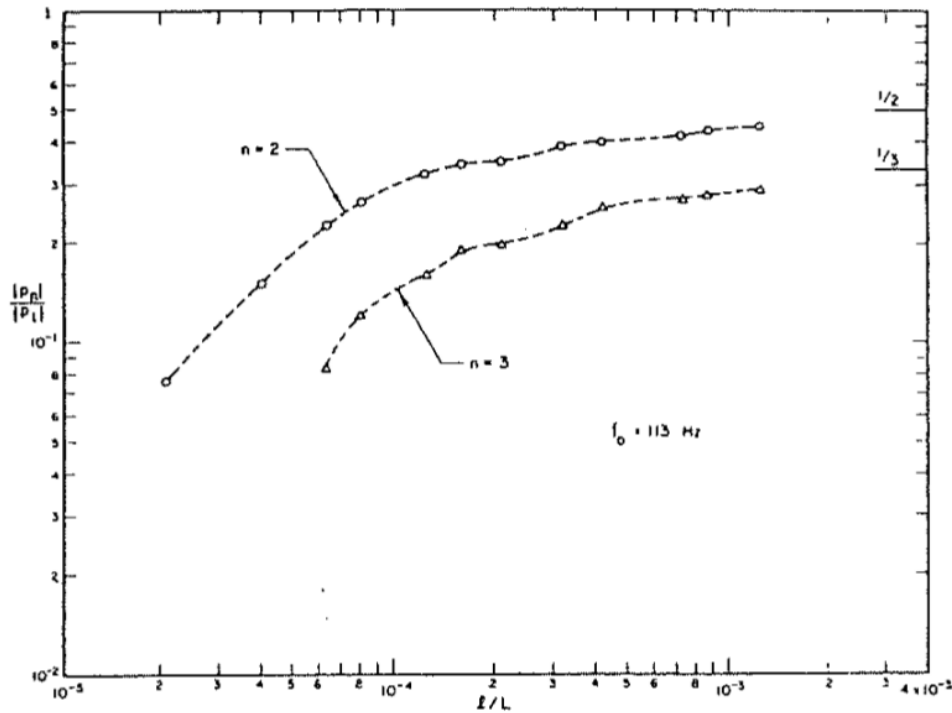


Figure 2.3: Temkin's steepened harmonics [38]. Each line plots the relative amplitude of a harmonic versus the nondimensional piston driving length. The relative amplitude is the pressure amplitude of the harmonic ( $p_n$ , in Temkin's notation) divided by the pressure amplitude of the fundamental  $p_1$ .

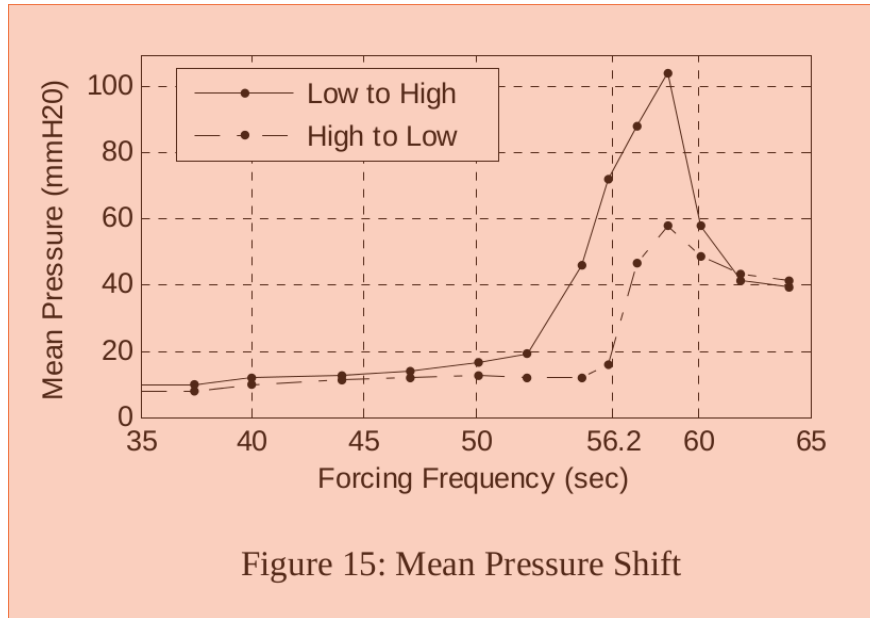


Figure 2.4: Jacob’s measured mean pressure shift [20]. Mean pressure is plotted versus driving frequency, showing a sharp rise around 56.2 Hz, which is a resonant frequency of the tube.

piston-driven tube—also observed by Saenger [36]—with the same phenomenon observed in rocket motors. DC shift is a change in the mean pressure caused by nonlinearity in the unsteady solution. Figure 2.4 shows the observed DC shift in pressure versus driving frequency. Wilson further developed the same apparatus, and quantified the  $\gamma$  dependence of the nonlinear steepening effect [39].

### 2.1.4 Cylindrical Wave Experiments

Despite being one of those subjects that is “well understood”, there is little in the experimental literature concerning waves in cylindrical chambers (outside of the combustion instability work). Like longitudinal modes, cylindrical acoustic modes were understood mathematically long before instrumentation was able to measure them directly. The author was only able to find three pieces of experimental work on strong waves in cylindrical chambers: Caap and Monkewitz [40] (radial modes), Phillips [41] (sloshing azimuthal modes and radial modes), and Heidmann [42] (spinning modes).

Caap and Monkewitz attempted to drive finite amplitude nonlinear radial waves. [40] Although they were unable to push the amplitudes into the strongly nonlinear regime, they did observe and report the presence of the first harmonic at maximum driving. They also reported detailed wave shape measurements for an isolated radial mode (Figure 2.5), something the author has been unable to find elsewhere in the literature.

Phillips developed an apparatus similar to that of Temkin [41]. Phillips, however, focused on cylindrical geometries. He was able to excite many different modes, as shown in Figure 2.6, and drove the amplitudes well into the



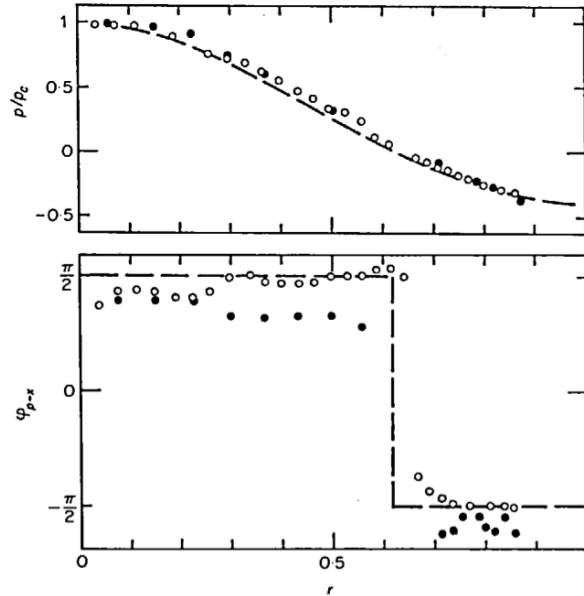


Figure 2.5: Caap and Mokewitz’s radial mode shape [40]. The top plot shows relative peak-to-peak pressure amplitude versus radial location. The bottom plot the phase of measured waves relative to the driving signal, again plotted versus radial measurement location.

nonlinear regime.

Heidmann (reputedly working with Priem [43]) developed an apparatus that produced powerful cylindrical waves [42] (apparatus in Figure 2.7). He used an unusual apparatus that could only drive spinning waves (a cylindrical chamber with a spinning gas jet at the center). Though he could only drive spinning waves, he published waveforms with amplitudes as high as 24 psi peak-to-peak with “near atmospheric” mean pressure (14.7 psi), and mentioned observing amplitudes as high as 38 psi. Figure 2.8 shows his chamber response to different driving frequencies, at various driving amplitudes. Note that Heidmann was able to identify the first three cylindrical spinning modes (1T, 2T, 3T), labelled “transverse mode” on Figure 2.8.

## 2.2 The Case for Heidmann’s Experiment

Of the experiments surveyed, Heidmann’s stood out. Unlike many combustion driven waves, the rotating gas jet experiment demonstrated repeatable results under defined conditions. All the known nonlinear properties of strong cylindrical waves mentioned in the literature were observable in the reported results. The experiment attained the highest peak-to-peak amplitude resonant waves of any the author has encountered: 200% of the mean pressure or higher.

Yet Heidmann’s work seems to have been largely overlooked by the community of combustion instability researchers of the time. Heidmann’s work was published in two NASA technical reports [44] [42] and one AIAA

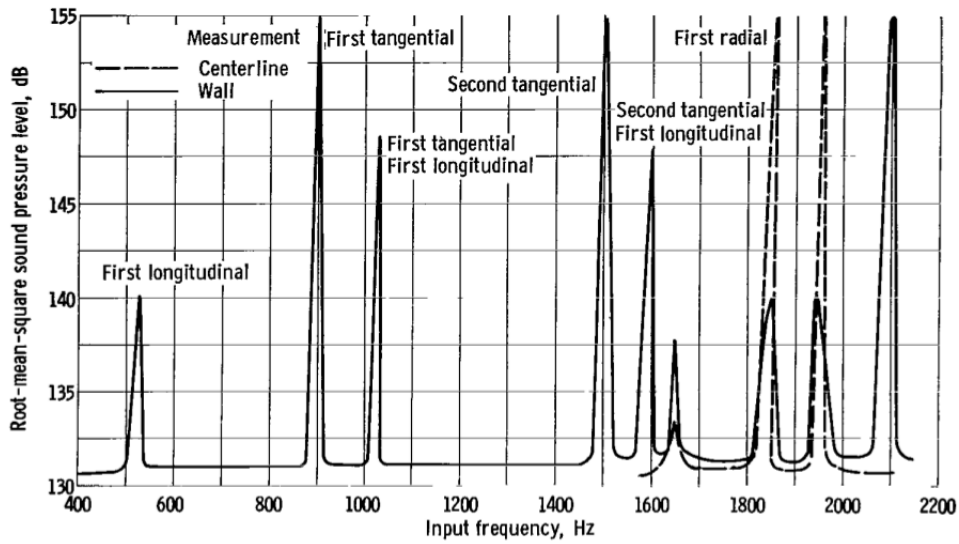


Figure 12. - Frequency response at test section with blank liner and both ends closed.

Figure 2.6: Phillips' chamber response [41]. The plot shows the measured sound pressure level versus driving frequency. When the driving frequency is at a resonant frequency, the corresponding mode is excited and observed pressure waves are much stronger.

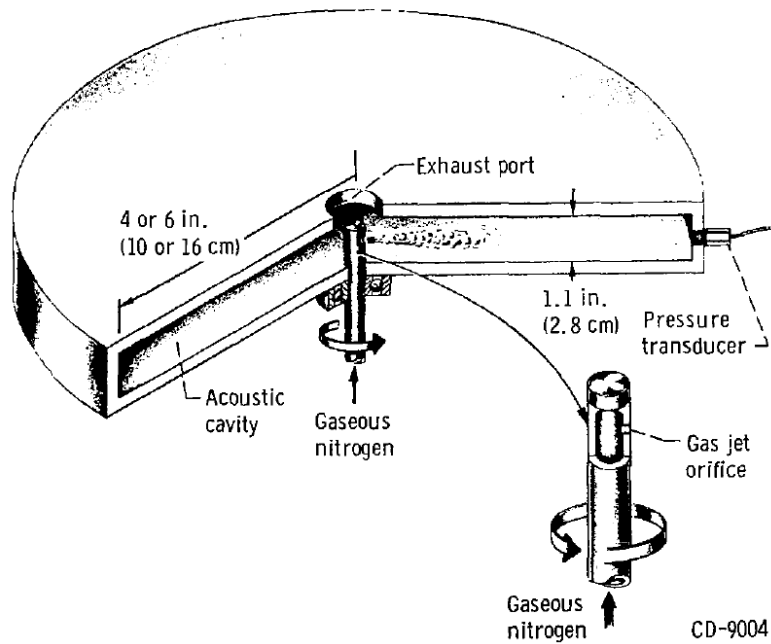


Figure 5. - Schematic of acoustic generator.

Figure 2.7: Heidmann's apparatus [44].

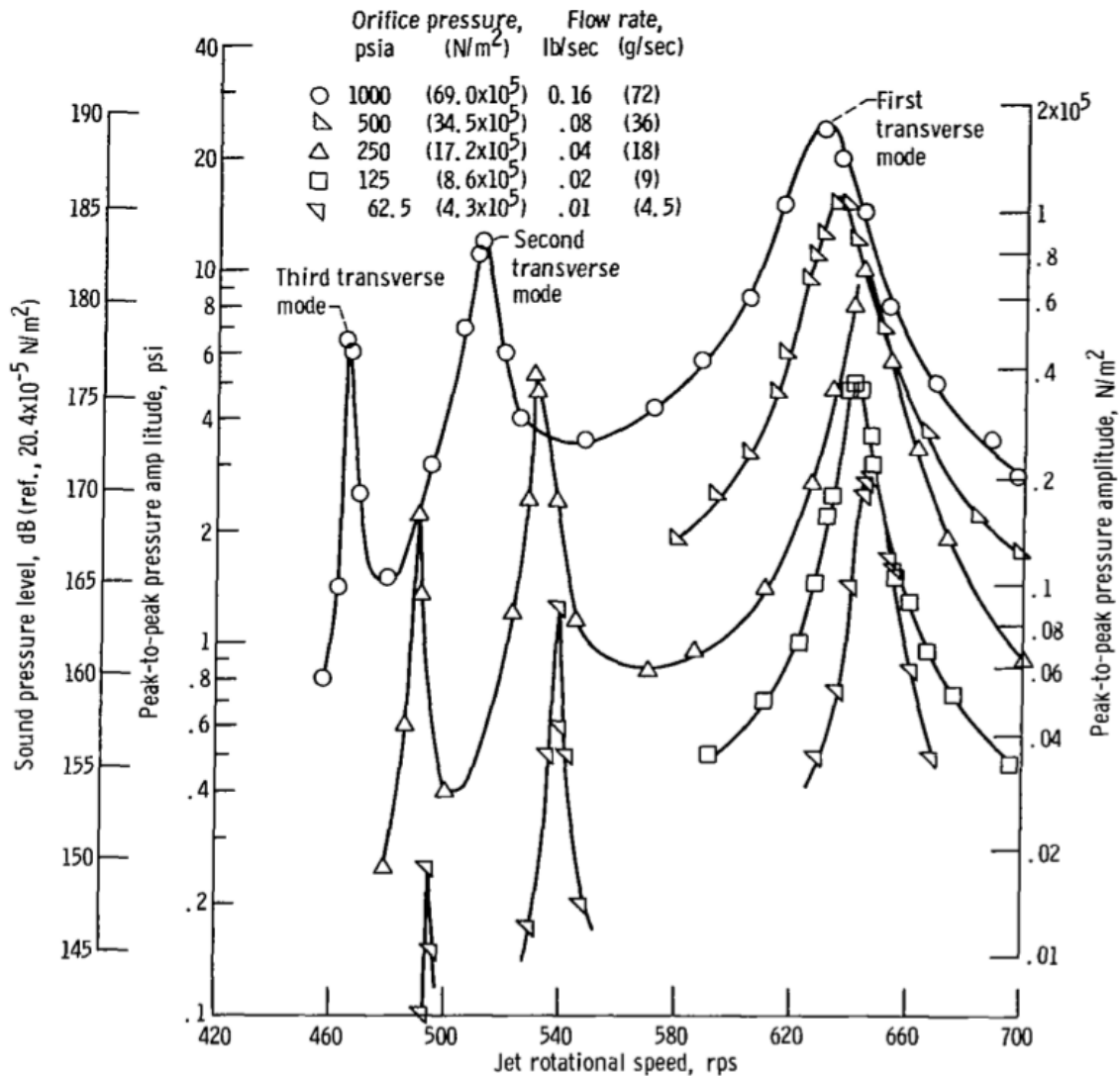


Figure 9. - Response of 3/32-inch (0.238-cm) diameter orifice in 12-inch (30.5-cm) diameter cavity.

Figure 2.8: Heidmann's chamber response to various excitations [42]. The vertical axis (labelled in three different unit sets) shows the dimensional peak-to-peak wave amplitudes. The horizontal axis denotes different driving frequencies in cycles per second (cps). The different symbols and lines each correspond to a flow rate for the jet, i.e., indicates how strongly the wave is being driven.

Journal note [26]. A survey of Web of Science at the time of writing showed that Heidmann's AIAA Journal note on the work [26] was cited only once, by Caap and Monkewitz [40]. A Google Scholar search showed the technical reports cited three times: once by a combustion instability technical report [45], once by Heidmann in a later note [46], and once by Heidmann in the second technical report [42]. This lack of references by the combustion instability theorists (Culick, Yang, Flandro etc.) indicates that, for one reason or another, they did not find the experiment valuable in their work.

It was apparently thought that Heidmann's experiment did not accurately reflect the conditions inside a rocket engine. The flat pancake shaped chamber was thought to have powerful and cross-interacting acoustic boundary layers on the two cylindrical surfaces. These strongly interacting boundary layers have no analogue in rocket engines, causing the CI community to consider the work irrelevant. [43]

Heidmann's attitude regarding this work was perhaps as significant as the CI community's dismissal. Heidmann did not see his work on rotating gas jets as a significant fluid dynamic experiment. He apparently viewed his work as evaluating a novel tool that could one day be used to do "real" combustion instability experiments. One NASA technical note from the work was entitled "Performance Evaluation of a Rotating Gas Jet..." [44], implying that the work was a type of technical calibration of equipment. The other NASA technical document was entitled "Empirical Characterization of Some Pressure Wave Shapes..." [42]', again indicating that the work was empirical without connection to theory. The one published note related to the work [26] begins:

Recent experiments have demonstrated a method of generating strong...(spinning) acoustic modes... A generator of this type could...[be] used to study the dynamic behaviour of physical and chemical phenomena related to propulsion systems (drop breakup, vaporization, burning, solid-propellant burning, acoustic absorption).

This statement indicates that the experiment was intended to prove a tool for the development of other experiments, not provide evidence in the validation (or invalidation) of theories.

Perhaps it was thought that nonlinearity and steepening were solved. Then, as now, Maslen and Moore's work was often cited, but no papers reproduced the solution for cases other than the one mode presented in the original 1956 work. It was considered to cover everything necessary about nonlinearity in cylindrical waves. Work was beginning to focus on the linear combustion instability analysis: identifying sources and sinks of unsteady energy.

Whatever the reason, Heidmann's work was ignored. Considering Jacob's recent finding (that modelling nonlinearity is critical to understanding experiments [14]) the experiment should no longer be ignored. With the need to validate nonlinear theory as in the present work, the rotating gas jet experiment of Heidmann offers an opportunity to compare nonlinear theory with well understood experimental waves at very high amplitudes, without the complexities of combustion devices.

Although the experiment does *not* accurately reflect the environment of a rocket engine, it does achieve high-amplitude cylindrical waves. With peak-to-peak amplitudes at 200% of mean pressure, Heidmann may have observed the strongest standing pressure waves ever recorded. No stronger waves were found in cold flow experiments during the extensive literature search for such experiments.

Table 2.1: Summary of Heidmann experiment parameters [44].

Chamber diameter	6	in	Two configurations were used: 4” and 6”. The 6” chamber was used for these tests.
Chamber height	1.1	in	
Mean temperature	60	F	STP (standard temperature and pressure)
Ratio of specific heats, $\gamma$	1.4		nitrogen working fluid

Heidmann’s experiment is not a rocket engine experiment. However, it exhibits the 1T and 2T spinning cylindrical modes. These modes are among the most common experienced by production engines, as they have the lowest frequencies and low frequency oscillations experience less viscous damping (see, for instance, Wilson [39]). The experiment achieves relative amplitudes ( $\Delta p/p_0$ ) as high as any combustion instability. It exhibits gas dynamic steepening, just as combustion instabilities do.

So for any nonlinear theory which claims to predict the limit cycle amplitude and/or the steepened waveform shape of a rocket engine or any other combustion device:

*Theories that predict the nonlinearity of combustion instabilities should be able to predict the nonlinearity of this experiment.*

This experiment therefore offers an opportunity to *validate* such theories in the context of a system that might be much easier to model than more typical combustion instability experiments (i.e., engines).

## 2.3 Model Problem: Spinning Wave

Heidmann’s experiment meets all the criteria sought: cylindrical modes, observed nonlinearity, repeatability, available data. None of the other experiments offered sufficient data at sufficiently high amplitudes to use for validation of cylindrical steepening theories.

Therefore, the 1T spinning mode of Heidmann’s apparatus was selected as a model problem. Each theory was used to model the geometry and flow conditions of this experiment, and each theory was validated against the data made available in Heidmann’s reports [44] [42].

### 2.3.1 Description of Experiment

Heidmann’s experiment consists of a shallow cylindrical chamber (Figure 2.7). At the center of one end, a small pipe protrudes into the chamber. This pipe has an opening on one side, and rotates. By pumping air through the pipe while it is spinning, a gas jet that rotates around the chamber is created. When this gas jet rotates around the chamber at the same speed as one of the antinodes of a resonant spinning wave, the resonant mode is excited. Table 2.1 presents the primary geometric and flow parameter characteristics known or presumed for Heidmann’s experiment.

In *Performance Study of Rotating Gas Jet Generator for Strong Travelling Transverse Acoustic Modes* [44], plots

of the pressure variation of 5 1T cylindrical waves at different peak-to-peak amplitudes are recorded with detailed flow conditions. Figure 2.9 shows each of these test cases. Nominal jet flow rates for each of the jet pressures were reported in the text of the report, and from Figure 2.10 it was possible to determine the mean pressure conditions for each test. The known flow parameters that are particular to these five test cases are presented in Table 2.2.

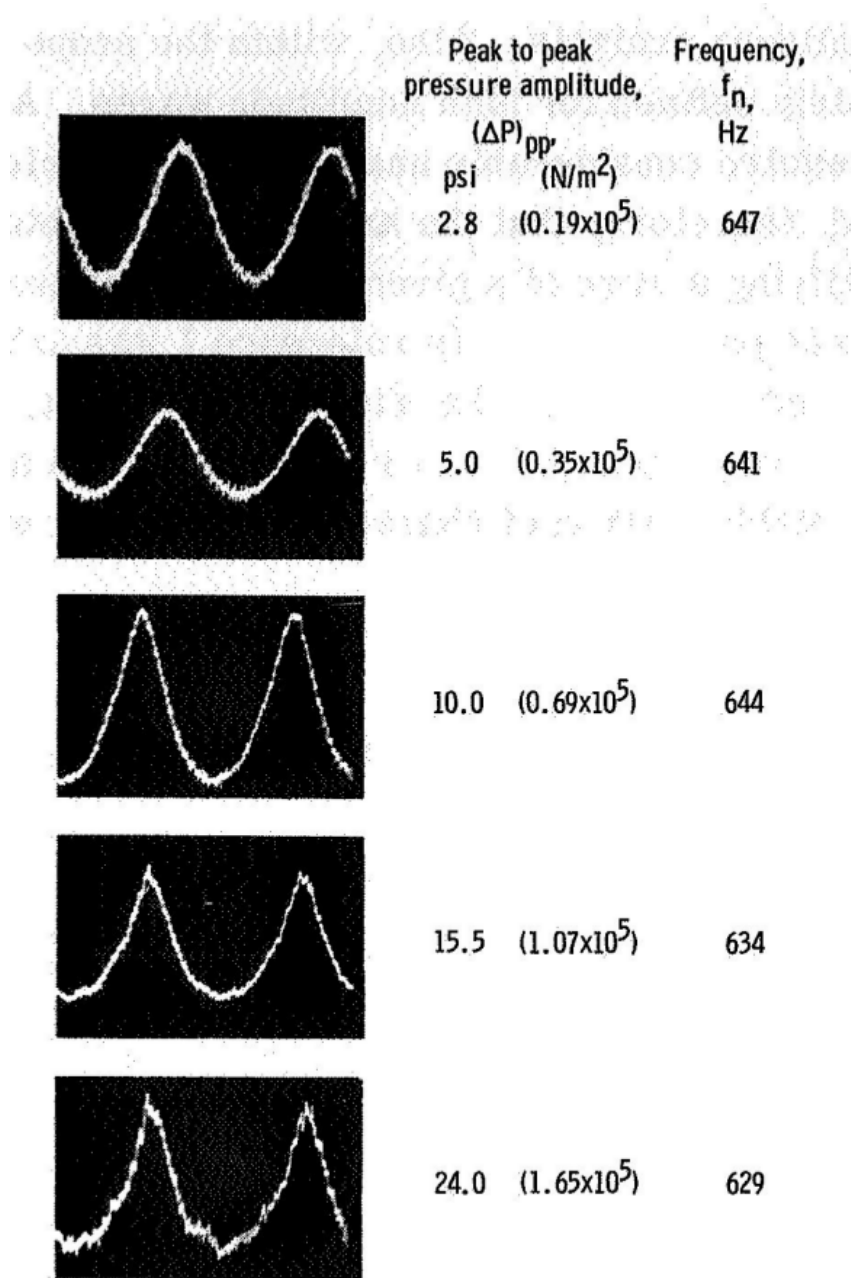


Figure 2.9: 1T spinning mode test cases [44].

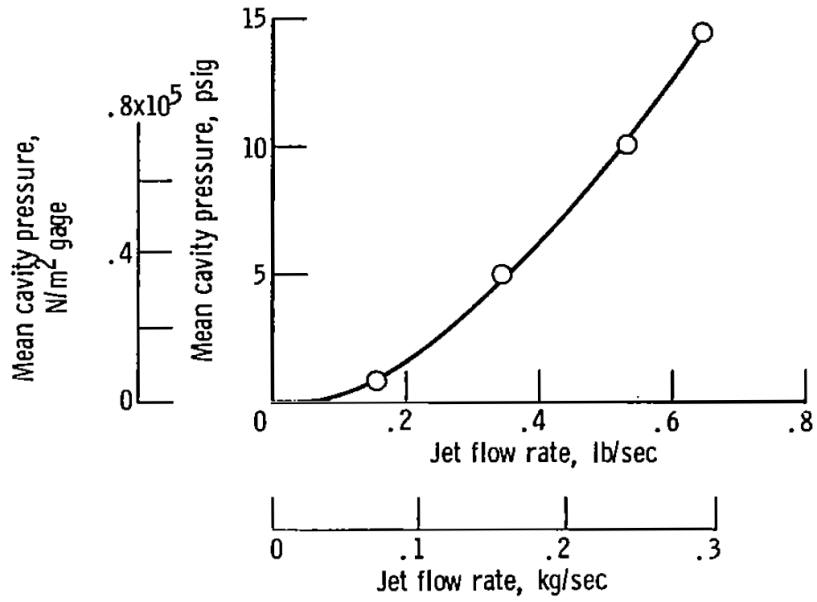


Figure 8. - Increase in cavity pressure with jet flow rate.

Figure 2.10: Mean pressure in experiment chamber versus jet flow rate [44].

Table 2.2: Summary of Heidmann experiment cases [44]

Case	Amplitude $\Delta p$	Frequency $f$	Gas jet pressure	Jet flow rate	Mean $p_0$	Relative amplitude $\frac{\Delta p}{p_0}$
1	2.8 psi	647 Hz	62.5 psi	0.01 lb/sec	14.7 psi	.19
2	5.5 psi	641 Hz	125 psi	0.02 lb/sec	14.8 psi	.37
3	10.0 psi	644 Hz	250 psi	0.04 lb/sec	14.9 psi	.67
4	15.5 psi	634 Hz	500 psi	0.08 lb/sec	15.3 psi	1.01
5	24.0 psi	629 Hz	1000 psi	0.16 lb/sec	15.7 psi	1.52

### 2.3.2 Data Analysis of Spinning Wave

To transform the pressure-time information of Figure 2.9 into digital information (a list of time-pressure pairs of numbers), the “Digitize Image” feature of Origin 8.6 was used with the following procedure:

1. Identify the two adjacent peaks in the graphic.
2. Establish the horizontal coordinate scale based on frequency (see Figure 2.11).
3. Identify the uppermost and lowermost extremes of the plot.
4. Establish the vertical coordinate scale based on pressure amplitude (see Figure 2.12).
5. Select some number of points on the graphic corresponding to the curve.
6. Export the identified points under the identified coordinate system to file.
7. Scatter-plot the digitized data and compare with the original graphic.

Figure 2.13 shows scatter plots of the resulting digital information, side-by-side with scans of Heidmann’s plots. This digitized data was used to validate each theory that was used to model strong cylindrical waves.

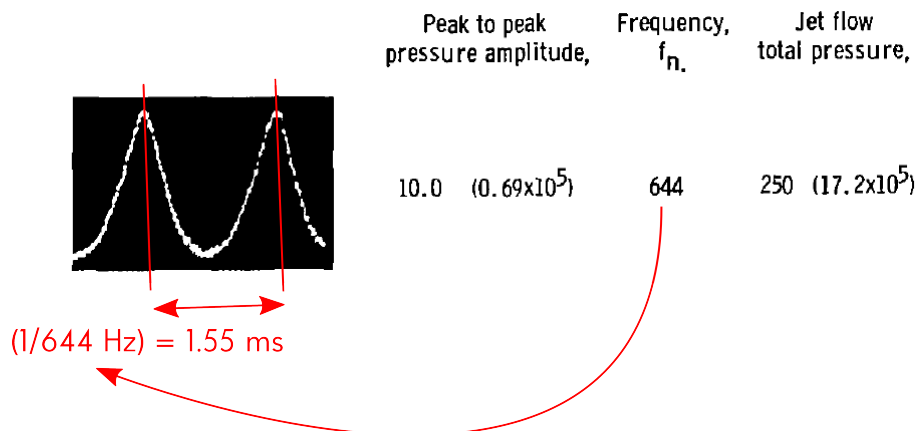


Figure 2.11: Frequency information and periodic waveform are used to establish horizontal dimensions.

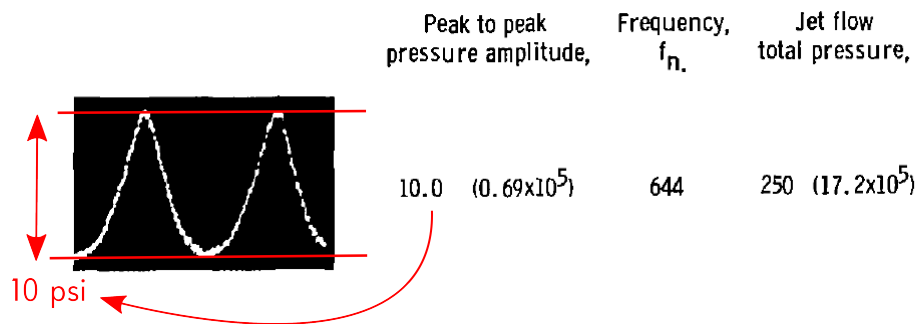


Figure 2.12: Peak/trough in plot and pressure amplitude are used to establish vertical plot dimensions.



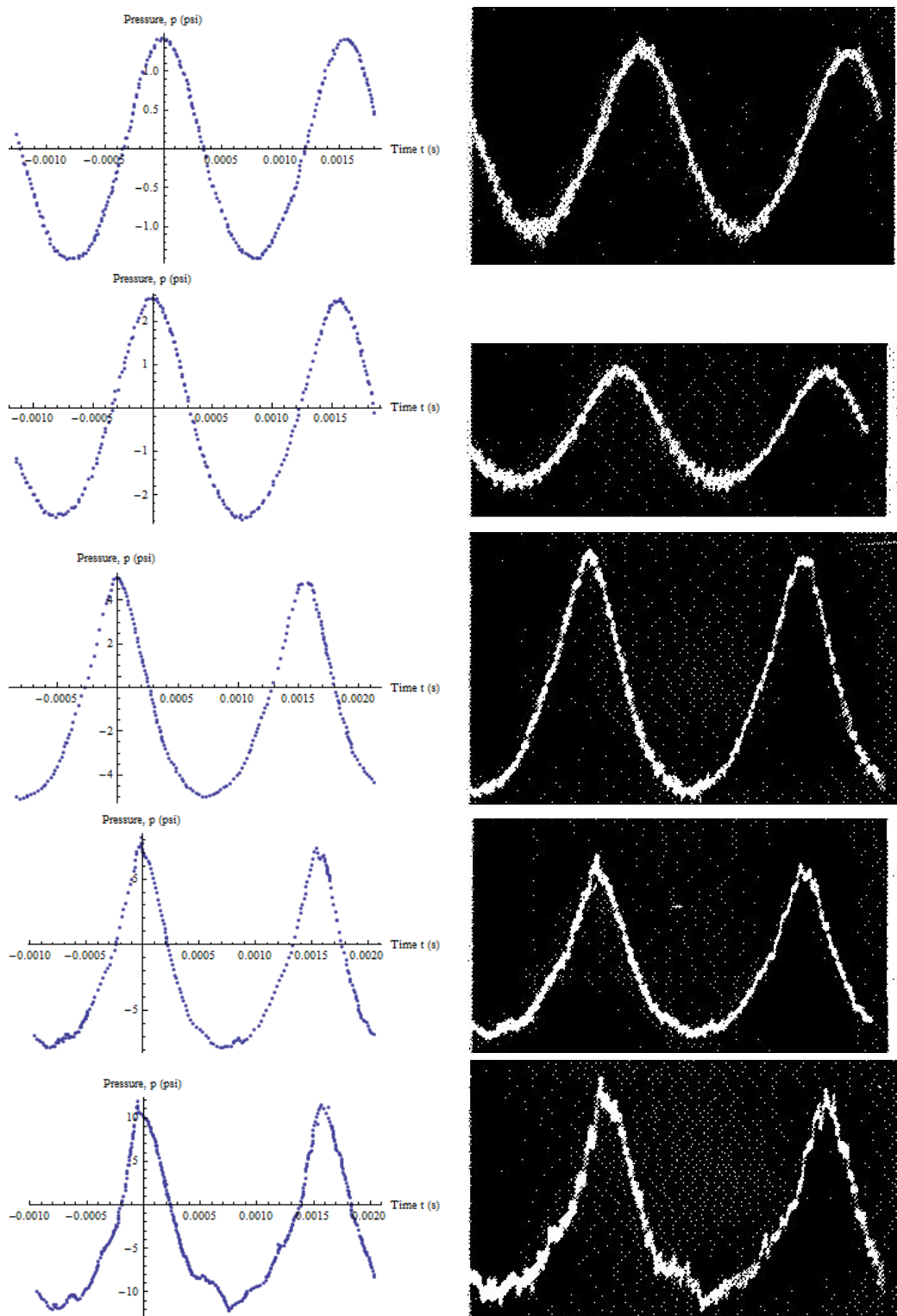


Figure 2.13: The digitized data for each test case is scatter plotted next to the original plot. In top-down order: 647 Hz, 2.8psi peak-to-peak, 641 Hz, 5.0psi peak-to-peak, 644 Hz, 10.0psi peak-to-peak, 634 Hz, 15.5psi peak-to-peak, 629 Hz, 24.0psi peak-to-peak.

## 2.4 Summary

An extensive search was performed of the literature concerned with experiments in combustion instability and nonlinear chamber acoustics. Several experiments were identified as possibly providing cylindrical wave data for validation of theories.

Heidmann's work with a rotating gas jet was found to have all the characteristics desired for a validation experiment. Heidmann's data and the experiment (if re-implemented) were evaluated for use in the present and future validation of combustion instability theories.

Finally, Heidmann's experimental data was analyzed and digitized to provide a model problem and numerical values for validation of the theories under consideration in subsequent chapters.

# Chapter 3

## Theory 1: Energy Cascade

Energy balance methods have been a successful technique for modelling combustion instabilities. The original linear energy balance model calculated stability by determining the difference between the addition of energy to a resonant mode through positive feedback mechanisms, and the energy loss in the mode due to negative feedback mechanisms [4].

This model has been extended to treat nonlinear transfer of energy between modes [4]. Flandro [18] and Jacob [25] have predicted limit cycle waveforms and amplitudes using this method. Wilson and Jacob have partially validated this nonlinear model using the piston-driven shock tube experiment [19].

Here, this model was used in two ways. In extended form, it was used to examine the energy stored in frequency shifts, and to find a physical description of harmonics in cylindrical waves. In its traditional form, under the assumption that the nonlinear solution can be modeled by a superposition of linear acoustic modes with sinusoidal time dependence, it was used to simulate the model problem of Chapter 2, showing that it can predict experimental observations while making the assumption.

### 3.1 Theory

The theory used here was derived in detail by Jacob [15]. One additional term for non-feedback driving, as derived by Wilson [39], was added to the nonlinear equation for cylindrical modes derived by Jacob [15]. Appendix A shows that derivation in detail.

The unsteady pressure  $p_1(\vec{r}, t)$  was assumed to be an expansion in the linear acoustic modes with time-varying amplitude functions  $R_n(t)$ . The other unsteady variables  $(\rho_1, T_1, \vec{u}_1)$  are also given in terms of the acoustic modes and these amplitude functions (see Appendix A).

$$p_1(\vec{r}, t) = p_0 \sum_{n=1}^{\infty} R_n(t) \sin(\omega_n t) \psi_n(\vec{r}) \quad (3.1)$$

The  $R_n(t)$  were assumed to be slowly varying functions of time, i.e., they change on a time scale smaller than the

fundamental period,  $\tau_{1T}$ . Jacob has recently generalized this work to allow fast-time considerations [47]. Here, however, the phases were assumed to be zero as in previous work [25].

A complete set of governing equations for the unknowns  $R_n(t)$  were found by inserting this expansion into the third-order energy balance, then space- and time-averaging the resulting equations. The energy balance equation was transformed into a set of energy balance equations for each mode. Those energy balance equations became a first order, nonlinearly coupled set of ODEs:

$$\dot{R}_n(t) = \zeta_n - \alpha_n R_n(t) - \frac{\gamma - 1}{2\gamma} \omega_n \sum_{m,l=1}^{\infty} F_{nml} R_m(t) R_l(t) \quad (3.2)$$

with  $\zeta_n$  a non-feedback driving coefficient, and  $\alpha_n$  the linear growth constant (see Appendix A). The coupling matrix  $F_{nml}$  for cylindrical modes was derived as:

$$\begin{aligned} F_{nml} &= \frac{\pi}{\kappa_m \kappa_l} (M_{nml}(\delta_1 + \delta_2 + \delta_3) + N_{nml}(-\delta_1 + \delta_2 + \delta_3)) \\ M_{nml} &= \int_0^1 J_n(\kappa_n r) J_m(\kappa_m r) J_l(\kappa_l r) \frac{1}{r} r dr \\ N_{nml} &= \int_0^1 J_n(\kappa_n r) \left( \frac{1}{r} J_m(\kappa_m r) - \kappa_m J_{m+1}(\kappa_m r) \right) \left( \frac{1}{r} J_l(\kappa_l r) - \kappa_l J_{l+1}(\kappa_l r) \right) r dr \\ \delta_1 &= \delta(n - m - l) \\ \delta_2 &= \delta(n + m - l) \\ \delta_3 &= \delta(n - m + l) \end{aligned}$$

where

$$\delta(m) = \begin{cases} 0 & \text{if } m \neq 0 \\ 1 & \text{if } m = 0 \end{cases}$$

## 3.2 Physical Explanation

One of the two questions posed at the start of this work was:

Why do cylindrical waves steepen into apparent harmonics, despite the natural resonances being nonharmonic?

The answer to that question resulting from the energy balance theory was:

Waves steepen into harmonics no matter the geometry or natural frequencies, because of energy stored in the frequency shift of each mode, and the balance of linear gains/loses and nonlinear coupling to other energy in the system.

### 3.2.1 Amplitude Energy Balance

To understand the energy balance of the frequency shifts, it was first necessary to understand the energy cascade model as it applies to amplitudes. In the expansion of Equation 3.1, each mode is governed by a time-dependent amplitude,  $R_n(t)$ . That amplitude is governed by an energy balance, comes down to Equation 3.2:

$$\frac{dR_n(t)}{dt} = \zeta_n - \alpha_n R_n(t) - \frac{\gamma - 1}{2\gamma} \omega_n \sum_{m,l=1}^{\infty} F_{nml} R_m(t) R_l(t) \quad (3.3)$$

In this equation, different terms are competing to change the energy of the mode.  $\zeta_n$  provides a constant increase or decrease of energy (depending on its sign).  $\alpha_n$  provides a feedback increase or decrease, increasing or decreasing the mode's energy depending on the mode's current energy. And the final term allows other modes to drain energy from, or add energy to, this mode.

If one mode is unstable (i.e., has positive  $\alpha_n$ )—or is being driven by a positive  $\zeta_n$ —then that mode's amplitude and energy will increase until  $\alpha_n R_n$  is equal to the other terms on the right hand side. When this happens, the time derivative vanishes, and the mode's energy stops increasing, but it also does not decrease. The energy sources and sinks are *in balance*, and a stable limit cycle is achieved.

This process is illustrated in Figure 3.1. The figure, made by Flandro [18], shows the process whereby a strong mode redistributes energy into higher modes as it increases in amplitude. With an unstable mode, or a powerfully driven mode, the nonlinear coupling terms start draining energy out of this mode and into other modes. Each of those modes starts to have its own energy balance fight. If those modes are linearly stable and are not directly driven (often the case, as usually viscous damping dominates other processes at high frequencies), then those modes experience a balance between the nonlinear energy coupling (which adds energy to the mode) and linear viscous damping (which drains energy from the mode).

This energy balance description explained the presence of harmonics in longitudinal geometries as the excitation of higher modes—which happen to have natural frequencies that are harmonically related to each other. For cylindrical geometries, this amplitude-only model predicted the excitation of higher modes with their natural frequencies—not harmonics.

### 3.2.2 Burnley's Optimal Energy Transfer

Burnley offered a physical description of the harmonic frequencies [24], using a two-mode expansion for cylindrical waves derived by Yang and Culick [23] which includes a time-dependent phase relationship between the two modes.

Burnley derived a form for the energy evolution of these two modes:

$$\frac{dE_{1T}}{dt} = 2\alpha_{1T} E_{1T} + 2a_T E_{1T} R_{2T} \cos X_T \quad (3.4)$$

$$\frac{dE_{2T}}{dt} = 2\alpha_{2T} E_{2T} + 2b_T E_{2T} \frac{R_{1T}^2}{R_{2T}} \cos X_T \quad (3.5)$$

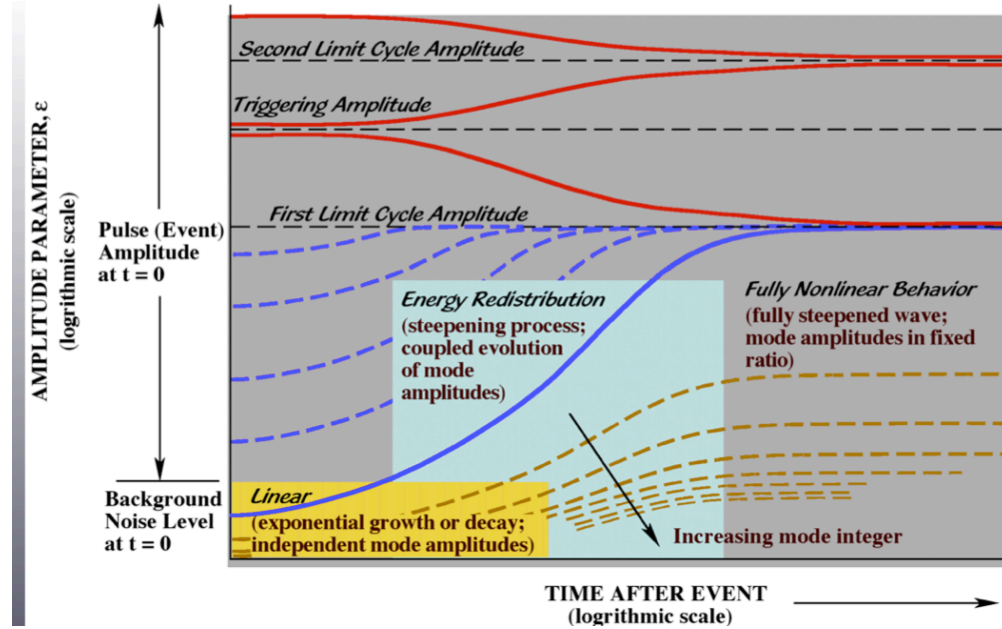


Figure 3.1: Nonlinear energy cascade in amplitude Flandro [18]. The blue lines describe the amplitude evolution of the dominant mode, the yellow lines show the amplitude evolution of higher modes.

where (in Burnley's notation)  $E_n$  is the energy in a mode,  $R_n$  is the amplitude of a mode,  $a_T, b_T$  are constants, and  $X_T(t)$  is a function of the frequencies and phases of both modes. The last term in these two equations represents energy transfer between the two modes. Burnley further demonstrated that this energy transfer is maximal when the second mode locks onto the first harmonic of the first mode.

This description has two shortcomings. First, this technique does not explain why all modes lock onto harmonics, since it only addresses two modes. Second, the description is a pair of observations: the experiments show integer harmonics, and energy transfer between modes is most efficient if the shifted frequencies are harmonic. Burnley does not offer a physical principle or mathematical justification for why "most efficient energy transfer" would be sought by the system.

Despite these shortcomings, the observations have merit. The experiments behave as though efficient energy transfer among modes is required, indicating that theoretical model involving energy transfer should explain the frequency shifts.

### 3.2.3 Extended Energy Balance

The energy balance technique of Flandro/Jacob was extended to discuss frequency energy. To do this, the expansion of Equation 3.1 was altered to allow shifted frequencies:

$$p(\vec{r}, t) = \sum_{n=1}^{\infty} R_n(t) \sin(\omega'_n(t)t) \psi_n(\vec{r}) \quad (3.6)$$

where  $\omega'_n(t) = \omega_n + \Delta\omega_n(t)$  is some time-dependent shifted frequency.

Inserting this new expansion into the energy balance equation, volume-integrating, and time-averaging (see the procedure of Appendix A), the total second-order unsteady energy became

$$\langle \int_V E_2 \rangle = \frac{\rho_0}{2} \sum_{n=1}^{\infty} A_n R_n(t)^2 \left( 1 + \frac{\omega'_n(t)^2 - \omega_n^2}{2\omega_n^2} \right) \quad (3.7)$$

This new form for the unsteady energy indicates that there is energy stored in the frequency shift of each mode. A complete derivation of an energy balance equation governing the frequency shift was attempted. It is likely that the further unpublished work of Jacob, which is much more general than that presented in this section, will complete this energy balance explanation [47].

### 3.3 Procedure

To solve Equation 3.2 for the model problem of Chapter 2, the following procedure was employed using Mathematica 9:

- Select and order a finite subset of modes to model the system.
- Calculate the coupling matrix  $F_{nml}$  for the selected modes.
- Determine the correct form of driving coefficients  $\zeta_n$  for the model problem.
- Use an ansatz technique to find appropriate values for  $\alpha_n, \zeta_n$ .
- Time-integrate the equations from initial conditions to limit cycle.
- Extract the limit cycle amplitudes and reconstruct the limit cycle waveform.
- Map the solution space: relative peak-to-peak pressure amplitude  $\Delta p/p_0$  versus driving parameter  $\zeta_n$ .

#### 3.3.1 Selection of Modes

To solve for the 1T spinning mode, a solution was first obtained for one 1T sloshing mode with 5 modes; one each of 1T0R, 2T0R, 3T0R, 4T0R and 5T0R modes (each mode number has the  $\sin(n\theta)$  versus  $\cos(n\theta)$  degeneracy, and only the cosine modes were used).

This is a limited set of modes. Large numbers of modes were attempted, but this was often found to cause stiffness and nonphysical results (such as negative amplitudes). Experience has shown that this restricted technique leads to fairly accurate results, as will be shown.

### 3.3.2 Determining Coefficients

A Mathematica script was written to compute the spatial coupling integrals:

$$M_{nml} = \int_0^1 J_n(\kappa_n r) J_m(\kappa_m r) J_l(\kappa_l r) \frac{1}{r} r dr \quad (3.8)$$

$$N_{nml} = \int_0^1 J_n(\kappa_n r) \left( \frac{1}{r} J_m(\kappa_m r) - \kappa_m J_{m+1}(\kappa_m r) \right) \left( \frac{1}{r} J_l(\kappa_l r) - \kappa_l J_{l+1}(\kappa_l r) \right) r dr \quad (3.9)$$

These coupling integrals also appear in the theories of Chapters 4 and 5. As this third-rank matrix is very expensive to compute ( $65^3 = 274,625$  integrals for 65 modes), the coefficients were computed once for 65 modes, and the results were saved.<sup>1</sup>

The use of Mathematica allowed most of the coefficients to be analytically evaluated to zero, as opposed to some small machine-precision approximation of zero. Knowing which coefficients are analytically zero allows equations containing them to be simplified analytically before being calculated, lowering the computational cost of simulations. There are other symbolic calculation programs, such as Maple, which would have allowed for this as well, but numeric integration routines would not.

The driving coefficients  $\zeta_n$  were set to zero for all but the 1T 0R mode, as only that mode is directly driven in the model problem. An ansatz value for  $\zeta_1$  was selected, and iterated against the growth constants  $\alpha_n$ .

Viscous damping is known to induce a frequency-squared dependence on  $\alpha_n$ :

$$\alpha_n \propto \omega_n^2 \quad (3.10)$$

An exact value was not computed. Instead, an ansatz was made for the first coefficient,  $\alpha_1$ , and the remaining coefficients were calculated as

$$\alpha_n = \alpha_1 \frac{\omega_n^2}{\omega_1^2} \quad (3.11)$$

These ansatz values for  $\alpha_1$  and  $\zeta_1$  were iterated until the solution reached a limit cycle in about .25 seconds. From there,  $\zeta_1$  was varied to achieve different limit cycle amplitudes. See Appendix A for a detailed description for why these ansatz values were chosen.

### 3.3.3 Solution

With computed coefficients and chosen values for  $\zeta$  and  $\alpha$ , the governing equations of Equation 3.2 were truncated to the fixed number of modes  $N$ :

$$\frac{dR_n(t)}{dt} = \zeta_n - \alpha_n R_n(t) - \frac{\gamma - 1}{2\gamma} \omega_n \sum_{m,l=1}^N F_{nml} R_m(t) R_l(t) \quad (3.12)$$

This equation set was then generated in Mathematica. An example of these equations is given in Figure 3.2.

<sup>1</sup>65 is the number of unique  $nT$   $mR$  modes up to  $n = 5, m = 5$ .



Mathematica's NDSolve routine was then used to integrate uniformly zero initial conditions ( $R_n(t = 0) = 0$ ) forward to a limit cycle ( $R'_n(t) \approx 0$ ) using, e.g., a Runge-Kutta integration routine. NDSolve can use many different algorithms, and a few were tried, with no significant differences among the solutions.

### 3.3.4 Amplitude vs. Driving

As the driving coefficient  $\zeta_1$  was increased from zero, the equations eventually became numerically unstable. Figure 3.3, which shows the maximum and minimum relative pressure values ( $p_{max}/p_0$  and  $p_{min}/p_0$ ) in the chamber, might indicate why this happened. As  $\zeta_1$  passed 1000, the minimum pressure approached 0. Negative pressures often cause solvers to crash.

Though the system became numerically unstable, it reached high amplitudes before failing. As Figure 3.4 shows, peak-to-peak wave amplitudes of 2.5 times the mean pressure were achieved in the simulation. All five test cases of Chapter 2, with a maximum wave amplitude of 1.6 times the mean pressure, were within the practical range of the model.

## 3.4 Experimental Validation

The theory was validated against experiment in two ways. First, for each test case, the experimental data and the solution with matching peak-to-peak amplitude were plotted together, as shown in Figure 3.5. The characteristic steepening shape—the shift from sinusoidal to a “U” shape—was apparent in both theory and experiment, and the two visually matched fairly well. Errors in the frequency might be causing the waveforms to appear shifted.

Second, an error was calculated between the predicted and observed waveforms. The error was taken as the root-mean-square of the fraction error of each pressure measurement  $i$  of the  $M$  test points available for a given test case:

$$\text{RMS error} = \sqrt{\frac{1}{M} \sum_i \left( \frac{P_{i,\text{experiment}} - P_{i,\text{theory}}}{P_{i,\text{experiment}}} \right)^2} \quad (3.13)$$

$$\begin{aligned} R(1)'(t) &= -344.919R(2)(t)R(1)(t) - 500.714R(1)(t) - 221.401R(2)(t)R(3)(t) \\ &\quad - 161.204R(3)(t)R(4)(t) - 125.537R(4)(t)R(5)(t) + 160. \\ R(2)'(t) &= 1384.97((R(1)(t))^2 - 781.804R(3)(t)R(1)(t) - 2002.86R(2)(t) \\ &\quad - 534.717R(2)(t)R(4)(t) - 404.731R(3)(t)R(5)(t) + 0. \\ R(3)'(t) &= 5941.68R(1)(t)R(2)(t) - 887.504R(5)(t)R(2)(t) - 4506.43R(3)(t) - 1248.24R(1)(t)R(4)(t) + 0. \\ R(4)'(t) &= 6056.59(R(2)(t))^2 + 10250.4R(1)(t)R(3)(t) - 8011.42R(4)(t) - 1728.47R(1)(t)R(5)(t) + 0. \\ R(5)'(t) &= 20143.2R(2)(t)R(3)(t) + 15670.7R(1)(t)R(4)(t) - 12517.8R(5)(t) + 0. \end{aligned}$$

Figure 3.2: Sample amplitude equations from Mathematica.

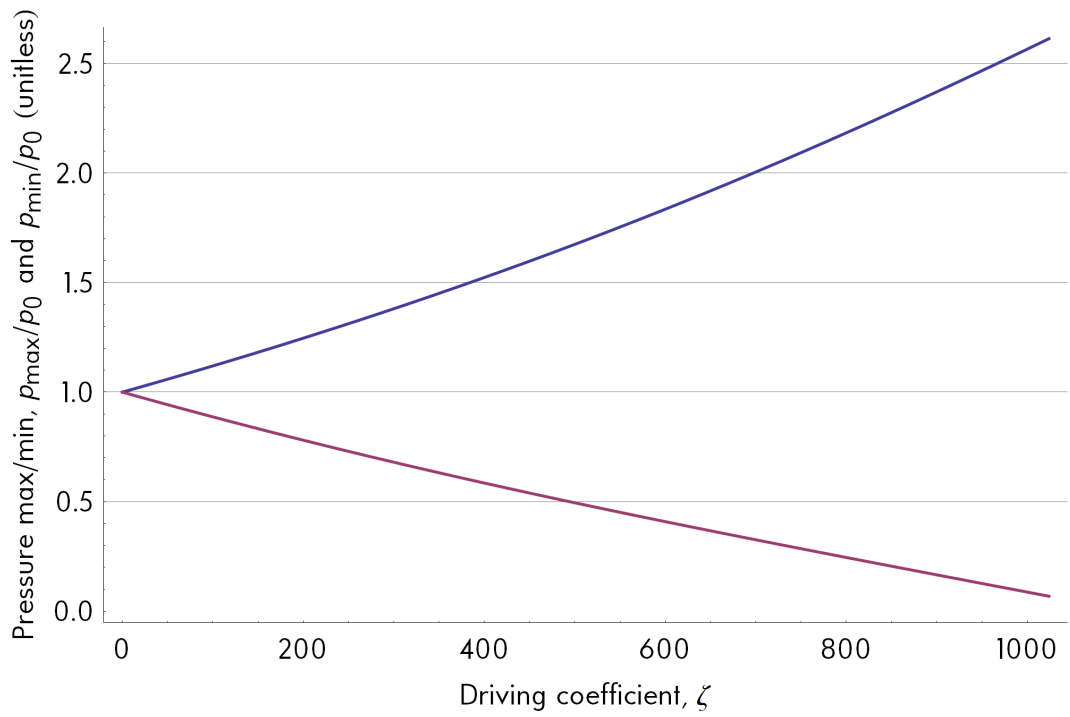


Figure 3.3: Minimum and maximum relative pressures ( $\frac{p_{max}}{p_0}, \frac{p_{min}}{p_0}$ ) of energy balance solution to 1T spinning wave

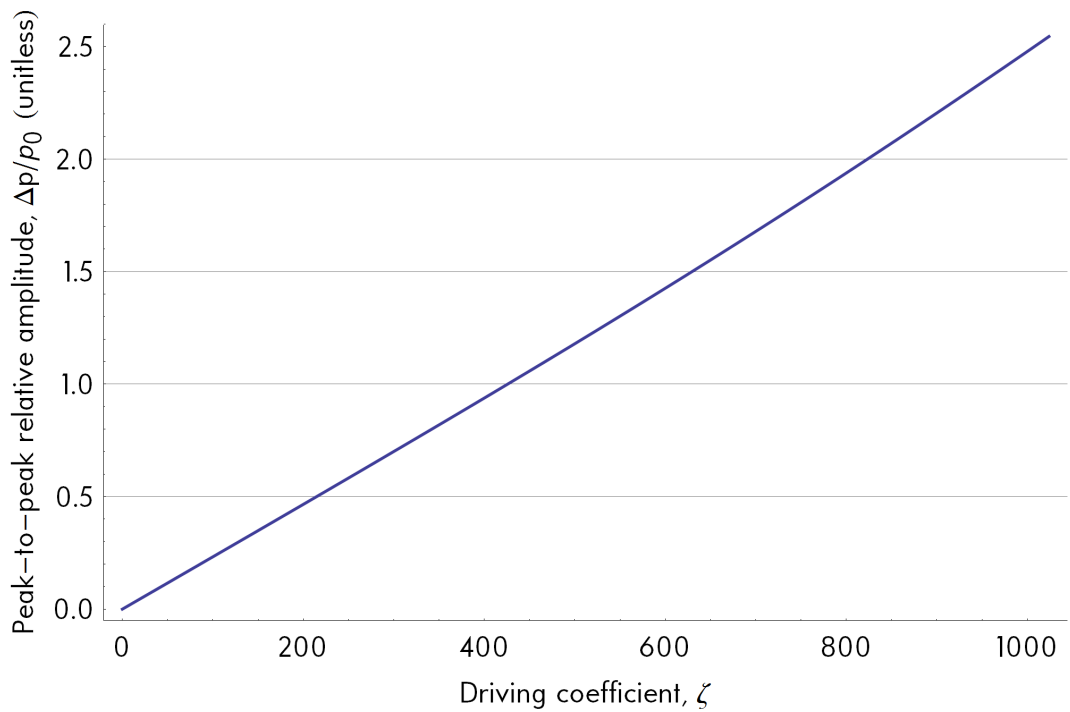


Figure 3.4: Peak-to-peak amplitudes ( $\frac{p_{max}-p_{min}}{p_0}$ ) of energy balance solution to 1T spinning wave

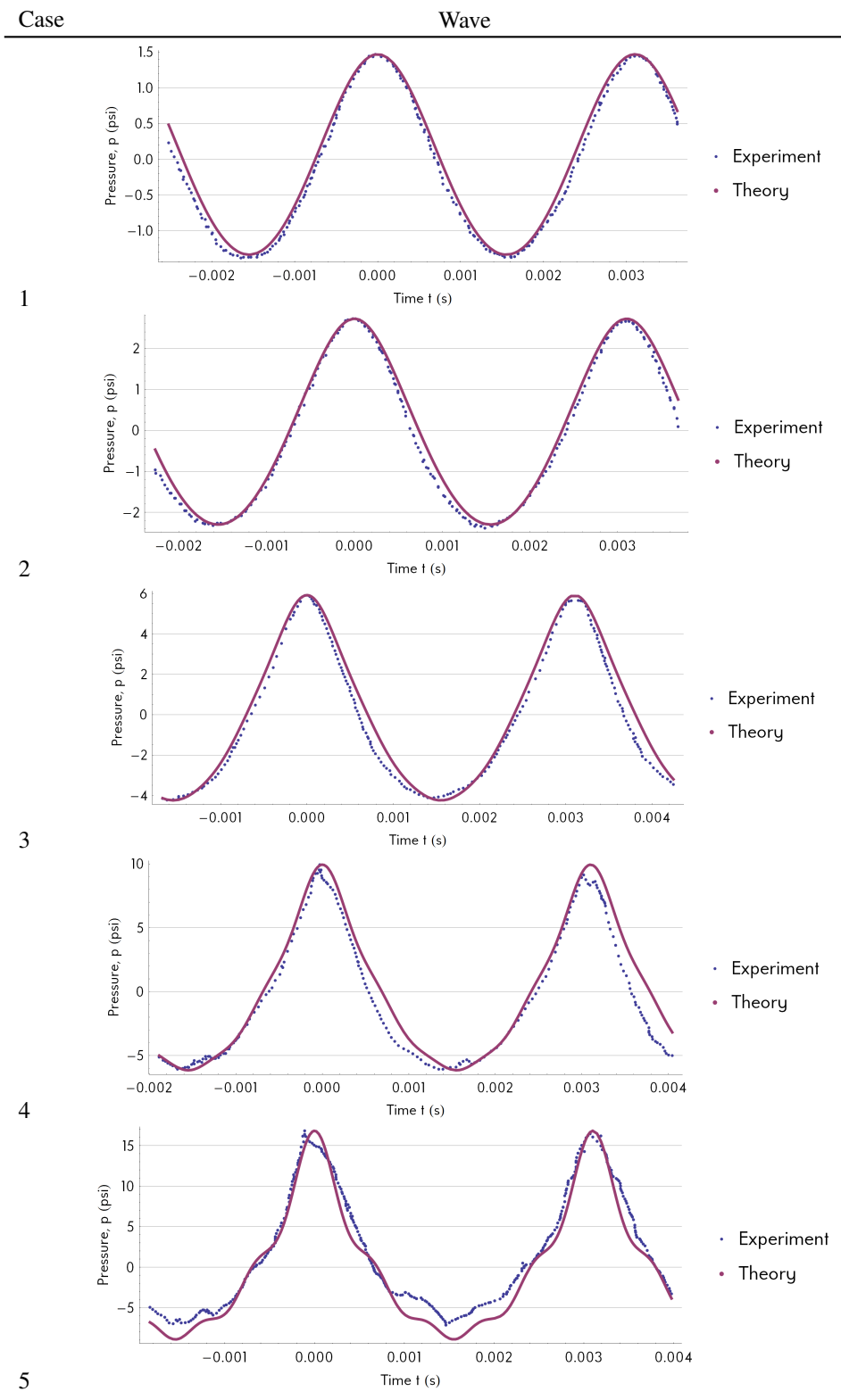


Figure 3.5: Pressure-time comparison of energy balance prediction (in red) to Heidmann experiment (in blue). See Table 2.2 for information on cases.

Table 3.1 shows this RMS error for each test point. The 4% to 9% RMS errors observed indicate good agreement.

### 3.5 Mode/Harmonic Decomposition

The mode/harmonic decomposition seeks to put the solution in terms of coefficients  $a_{nm}, b_{nm}$  as in Equation 1.44:

$$p(\vec{r}, t) = \sum_{n,m=1}^{\infty} (a_{nm} \sin(m\omega t) + b_{nm} \cos(m\omega t))\psi_n(\vec{r}) \quad (3.14)$$

However, the expansion assumed in Equation 3.1 is already in this form:

$$p_1 = p_0 \sum_{n=1}^{\infty} R_n(t) \sin(\omega_n t) \psi_n \quad (3.15)$$

with  $b_{nm} \equiv 0$  and  $a_{nm} = R_n(t_f)\delta_{nm}$  ( $t_f$  the time at limit cycle, and  $\delta_{nm}$  the Kronecker delta function). The first few coefficients are shown in Table 3.2. Note that since only a small number of purely tangential (azimuthal) modes were considered, most of the coefficients were zero by assumption.

The error energy of this decomposition is identically zero, indicating that this simulation shows exact agreement with the mode/frequency assumption. And it should, given that the assumption was made during the derivation of this model.

### 3.6 Summary

The energy balance theory was shown to provide a physical explanation of harmonics in strong cylindrical waves: shifted frequencies store energy and obey an energy balance, which drives the frequency shifts towards harmonics of the dominant frequency. Further unpublished work anticipated from Jacob [47] was expected to show the exact form of this energy balance.

The theory was then used in its traditional form—without frequency shifts—to model the experiment. The model was numerically solved to the maximum amplitude permitted numerically, which was 2.5 times the mean pressure.

Table 3.1: RMS error comparison of energy balance prediction to experiment

Peak-to-peak Case	Relative $\Delta p$	RMS err $\frac{\Delta p}{p_0}$	
1	2.8 psi	0.19	4.15%
2	5.5 psi	0.37	4.55%
3	10.0 psi	0.67	7.02%
4	15.5 psi	1.01	8.94%
5	24.0 psi	1.52	5.36 %

Table 3.2: Decomposition coefficients for energy balance. Modes  $n$  are ordered by natural frequency. sin/cos indicates the  $\theta$ -coordinate spatial degeneracy. Harmonics  $m$

			$m$	0	1	2	3	4	5	6
$n$			$a_{nm}$							
0	1T0R	cos		0	.30	0	0	0	0	0
1	1T0R	sin		0	0	0	0	0	0	0
2	2T0R	cos		0	0	.06	0	0	0	0
3	2T0R	sin		0	0	0	0	0	0	0
4	0T1R	-		0	0	0	0	0	0	0
5	3T0R	cos		0	0	0	.02	0	0	0
6	3T0R	sin		0	0	0	0	0	0	0

			$m$	0	1	2	3	4	5	6
$n$			$b_{nm}$							
0	1T0R	cos		0	0	0	0	0	0	0
1	1T0R	sin		0	.30	0	0	0	0	0
2	2T0R	cos		0	0	0	0	0	0	0
3	2T0R	sin		0	0	.06	0	0	0	0
4	0T1R	-		0	0	0	0	0	0	0
5	3T0R	cos		0	0	0	0	0	0	0
6	3T0R	sin		0	0	0	.02	0	0	0

The model was compared against the experiment, which it matched well: 4% to 9% waveform RMS error.

Finally, the solution was decomposed (trivially) to show what a decomposed system that meets the mode/frequency assumption looks like in coefficients.

## Chapter 4

# Theory 2: Steepening

The first approach to predicting flow behavior in a system is to derive analytical solutions from the governing equations. Maslen and Moore used the tools available to them to generate such a solution to the strong cylindrical wave problem in 1956 [21]. That solution was and is widely cited whenever strong cylindrical waves are considered.

Maslen and Moore's solution approach was explored and used to simulate the model problem. The solution was validated against Heidmann's experiment—possibly the first time Maslen and Moore's solution has been directly compared to experiment. The double-decomposition process was applied to the solution. Finally, a spatially distributed but time-independent component of the solution was identified as an aspect of strong cylindrical waves, possibly overlooked by the combustion instability community.

### 4.1 Theory

An attempt was made to derive a similar solution using more recent developments in nonlinear acoustics, see Appendix B. The governing equations derived this way agreed with Maslen and Moore's to second order, and contained fewer terms at third order. As Maslen and Moore's derivation made fewer assumptions than the nonlinear acoustics approach, their older solution was considered better for modeling the problem.

The procedure followed by Maslen and Moore [21] was:

1. State the governing equations (fluid, thermodynamic, state).
2. Reduce the number of field variables (potential flow assumption).
3. Derive a (nonlinear) wave equation (eliminate variables from the governing equations).
4. Reduce the nonlinear problem into a series of linear problems (perturb the wave equation).
5. Apply boundary conditions to solve the first order problem (find the eigenvalue / eigenfunction solution space).
6. Use the first order solutions to solve for second-order corrections to each eigenfunction.
7. Use the first- and second-order solutions to solve for third-order corrections to each eigenfunction.

Under this procedure, Maslen and Moore derived a nonlinear wave equation in velocity potential  $\Phi$  (with  $\vec{u} =$

$-\nabla\Phi$ ). Perturbing that wave equation, they obtained governing equations in the form of modified telegrapher's equations:

$$\Phi(\vec{x}, t) = \Phi_0 + \epsilon\Phi_1 + \epsilon^2\Phi_2 + \epsilon^3\Phi_3 + \dots \quad (4.1)$$

$$\epsilon = \text{strained/perturbation parameter} < 1 \quad (\ll 1 \text{ for analytic convergence}) \quad (4.2)$$

$$\Phi_0 = \text{constant} \equiv 0 \quad (\text{no mean flow}) \quad (4.3)$$

$$\frac{\partial^2\Phi_1}{\partial t^2} - c_0^2\nabla^2\Phi_1 = 0 \quad (4.4)$$

$$\frac{\partial^2\Phi_2}{\partial t^2} - c_0^2\nabla^2\Phi_2 = -\frac{\partial}{\partial t} \left[ \nabla\Phi_1 \cdot \nabla\Phi_1 + \frac{\gamma-1}{2a_0^2} \frac{\partial\Phi_1}{\partial t} \frac{\partial\Phi_1}{\partial t} \right] \quad (4.5)$$

$$\begin{aligned} \frac{\partial^2\Phi_3}{\partial t^2} - c_0^2\nabla^2\Phi_3 = & -\frac{\partial}{\partial t} \left[ 2\nabla\Phi_1 \cdot \nabla\Phi_2 + \frac{\gamma-1}{a_0^2} \frac{\partial\Phi_1}{\partial t} \frac{\partial\Phi_2}{\partial t} \right] \quad (4.6) \\ & - \frac{1}{2} \nabla\Phi_1 \cdot \nabla(\nabla\Phi_1)^2 \\ & + \frac{\gamma-1}{2} (\nabla\Phi_1)^2 \frac{\partial^2\Phi_1}{\partial t^2} \\ & - (\gamma-1)^2 \frac{\partial\Phi_1}{\partial t} \frac{\partial\Phi_1}{\partial t} \frac{\partial^2\Phi_1}{\partial t^2} \\ & - \frac{\partial}{\partial t} \left[ (\gamma-1) \nabla\Phi_1 \cdot \nabla\Phi_1 \frac{\partial\Phi_1}{\partial t} \right] \end{aligned}$$

Appendix B gives a derivation of similar equations that shows the process in greater detail.

They then state the solutions to these equations, in terms of well-known functions (such as sine and cosine) as well as some unusual functions  $P_{ij}(r)$  (the solutions to inhomogeneous Bessel equations stated in their articles). For spinning modes, those solutions are:

$$p = p_0 * (1 + \epsilon p_1 + \epsilon^2 p_2 + \epsilon^3 p_3 + \dots) \quad (4.7)$$

$$p_1 = -\gamma P_{10} \cos(\omega_n t + n\theta) \quad (4.8)$$

$$p_2 = -2\gamma P_{20} \cos(2\omega_n t + 2n\theta) - 2\gamma P_{23} \quad (4.9)$$

$$p_3 = -4\gamma P_{30} \cos(3\omega_n t + 3n\theta) - \gamma P_{34} \cos(\omega_n t + n\theta) \quad (4.10)$$

Maslen and Moore laid out, in complete detail, the exact equations and boundary conditions that govern these  $P_{ij}(r)$  functions [21], with only one notation difference. They used  $\alpha = r/R$ , the nondimensional radial coordinate variable:  $P_{ij}(\alpha)$ .

## 4.2 Physical Explanation

One of the two questions posed in the introduction concerns the “why” of cylindrical harmonics:

Why do cylindrical waves steepen into apparent harmonics, despite the natural resonances being nonharmonic?

The answer to that question resulting from the mode-steepening theory is:

Waves steepen into harmonics no matter the geometry or natural frequencies, because the wave is a single, coherent periodic fluid dynamic motion. Though it changes shape due to nonlinearity, it remains periodic and therefore spectral analysis will only reveal harmonics.

This explanation was found to be common to two ways of thinking about steepening: speed-of-sound variations, and nonlinear amplifiers.

### 4.2.1 Speed-of-Sound and Wave Reflections

Maslen and Moore introduced the subject of cylindrical waves steepening with a discussion of the traditional plane-wave steepening explanation. They described waves steepening due to the change in wave speed: part of the wave “catches up” to the leading edge of the wave, causing each pulse to steepen into a shock (see Figure 4.1).

Maslen and Moore stated that cylindrical waves do not behave in the same way, however, due to wave reflections. When a wave is turned, part of the wave scatters (Figure 4.2). In a cylindrical chamber, the wall is continuously turning the wave, leading to a changed waveform. This explanation seems reasonable, though no detailed mathematics were offered in support of it.

### 4.2.2 Nonlinear Amplifiers

The method of strained parameters offered yet another explanation. Each of the Equations 4.4 to 4.6 can be thought of as a linear operator equation in the form:

$$L[y] = f(x) \tag{4.11}$$

where  $L$  is the wave equation operator,  $y$  is the solution at the next order, and  $f(x)$  is some polynomial function of the previous orders. Looked at this way, each successive correction is a nonlinearly amplified version of previous orders. Since the nonlinearity is polynomial of finite order and the excitation is sinusoidal, each successive solution will only contain sum-and-difference frequencies of the excitation, i.e., harmonics.

All three points of view led to the same conclusion: the wave is transformed nonlinearly, but it remains a periodic wave, and can thus only contain harmonics.



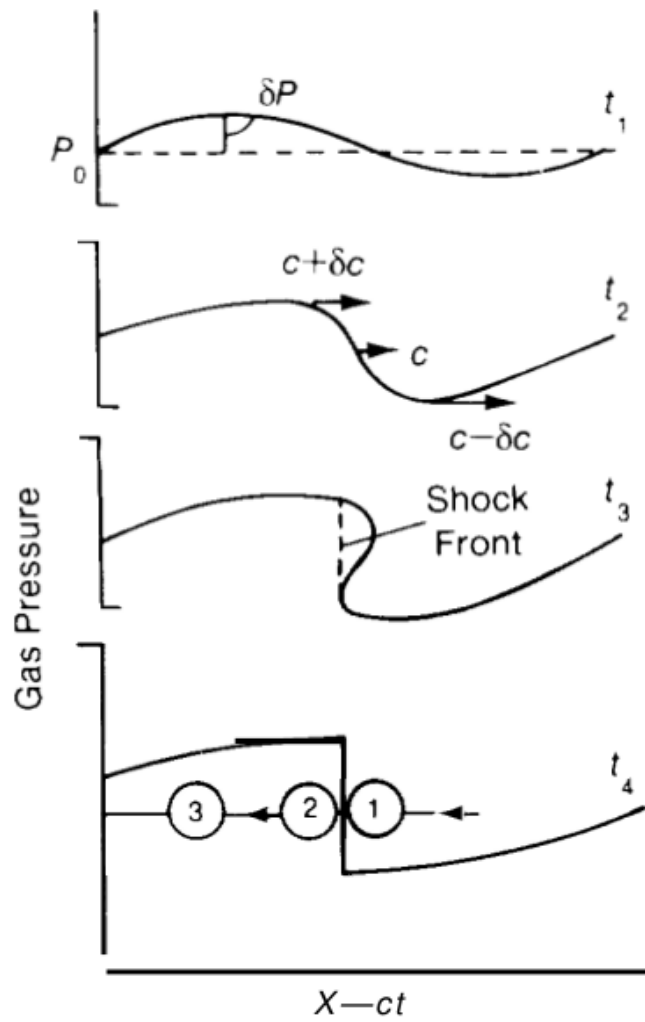


Figure 4.1: Longitudinal/planar steepening diagram. The horizontal axis is a distance coordinate  $x - ct$  for which the wave appears to be standing still. The progression from top to bottom shows how a wave tries to become multi-valued due to differing wave speeds, and collapses to a shock.

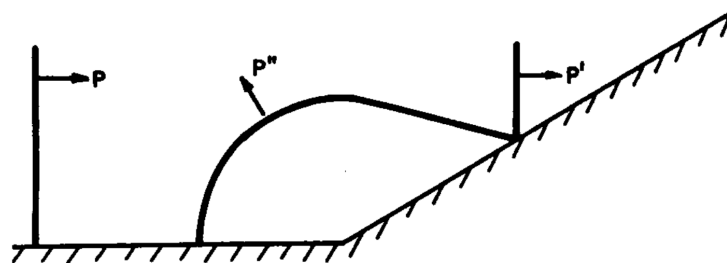


Figure 4.2: Turn-scattering of an acoustic pulse (from [21]). An initial pulse  $P$  becomes a continuing pulse  $P'$  plus a scattered pulse  $P''$ .

## 4.3 Procedure

To simulate the model problem of Chapter 2, the following procedure was used:

- The functions  $P_{ij}(r)$  were numerically evaluated using Mathematica.
- The Maslen/Moore pressure solutions of Equation 4.7 were calculated for a range of  $\epsilon$ 's, and peak-to-peak amplitudes calculated.
- The solutions were plotted and validated against the five test cases of Chapter 2.
- The solutions were analytically and numerically decomposed into modes/harmonics, and the frequency/mode assumption examined.
- The solution was plotted with and without the zero-frequency component, revealing a nontrivial contribution to the overall wave shape.

### 4.3.1 Numerical Solutions

With modern computers, numerically evaluating Maslen and Moore's solution seemed like a trivial task. However, the inhomogeneous Bessel equations that define the solution functions  $P_{ij}(r)$  are singular at  $r = 0$ . Solving them numerically was more difficult than anticipated.

One approach was to enforce the boundary conditions at  $r = \epsilon_0 \ll 1$  instead of at  $r = 0$ . This method was used in the solution that follows. At second order, this gave solutions similar to, but not identical to, Maslen and Moore's. At third order, many of the functions were quite different from Maslen and Moore's (see Figure 4.3).

It is unclear which of the two numerical evaluations is more accurate. The modern numerical solutions were used, as those solutions validated against experiment.

### 4.3.2 Amplitude vs. Epsilon

It is fairly common for perturbation solutions to be accurate well beyond the validity of the perturbation assumption. In this case, that corresponds to situations where  $\epsilon \ll 1$  does not hold. Solutions were tested up to  $\epsilon = 2$ . Throughout this range, the equations never became numerically unstable. Negative pressure appeared for  $\epsilon \geq 1.5$ , making the solution physically invalid for that range (Figure 4.4). For  $\epsilon < 1.5$ , the maximum pressure increased more rapidly than the minimum pressure declined, allowing the wave to reach amplitudes a purely sinusoidal wave could not reach. Pure sinusoidal variation around a mean value has a maximum valid peak-to-peak amplitude of twice the mean value.

As Figure 4.5 shows, peak-to-peak wave amplitudes of 3.5 times the mean pressure were achieved in valid simulations (i.e., no negative pressures, with  $\epsilon < 1.5$ ). As a point of comparison, this was the same maximum amplitude achieved with the method of Chapter 3. All five test cases of Chapter 2, with a maximum wave amplitude of 1.6 times the mean pressure, were within the practical range of the model.

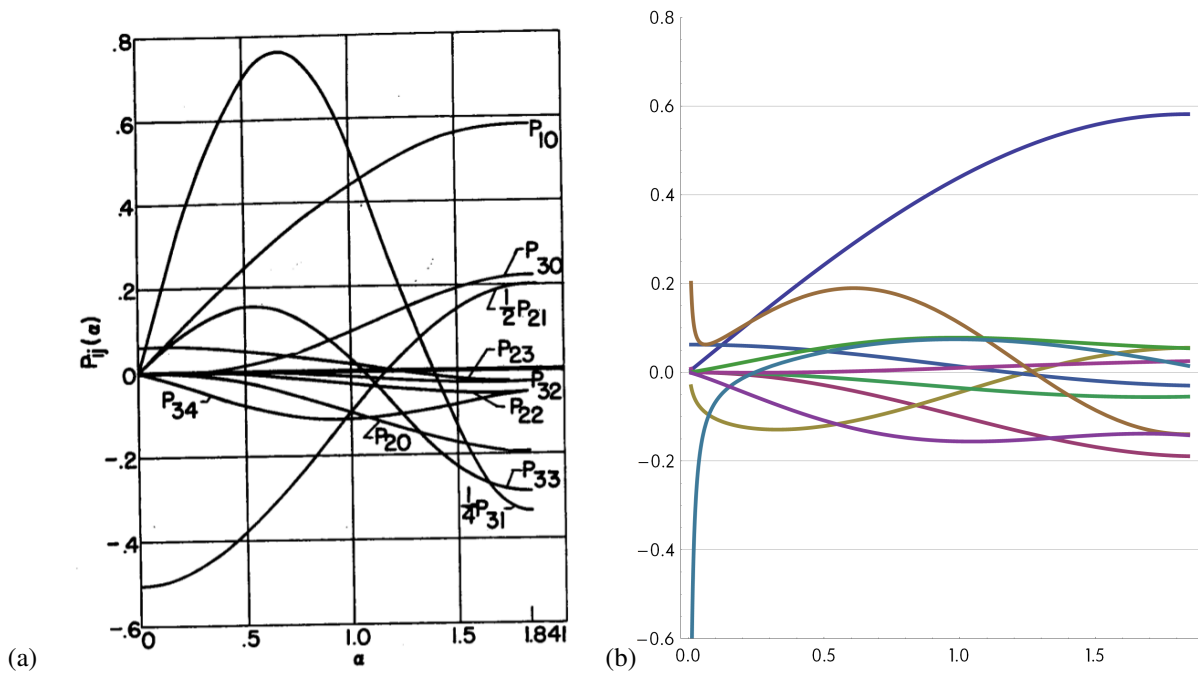


Figure 4.3: (a) Maslen and Moore's  $P_{ij}$  functions, evaluated for  $n = 1$ , as reported by Maslen and Moore. (b) The  $P_{ij}$  functions, as recreated by the author. Both plots have the same axes: a nondimensional solution function along the vertical, and the nondimensional radial coordinate variable  $r/R$  along the horizontal.

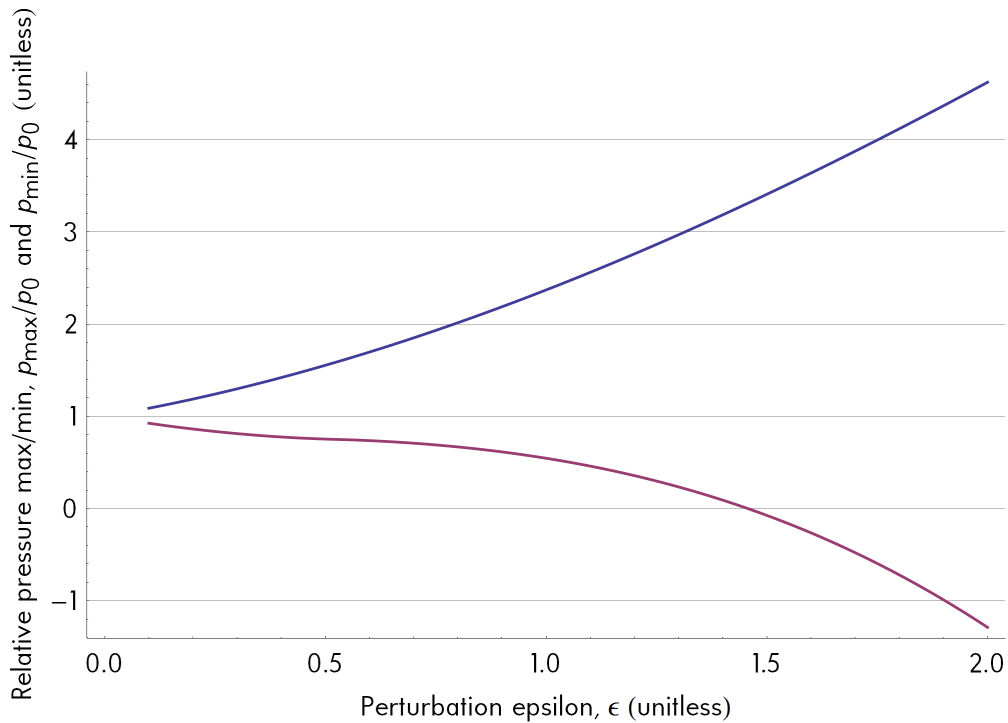


Figure 4.4: Minimum and maximum relative pressures ( $\frac{p_{max}}{p_0}$ ,  $\frac{p_{min}}{p_0}$ ) of Maslen/Moore 1T spinning wave solution.

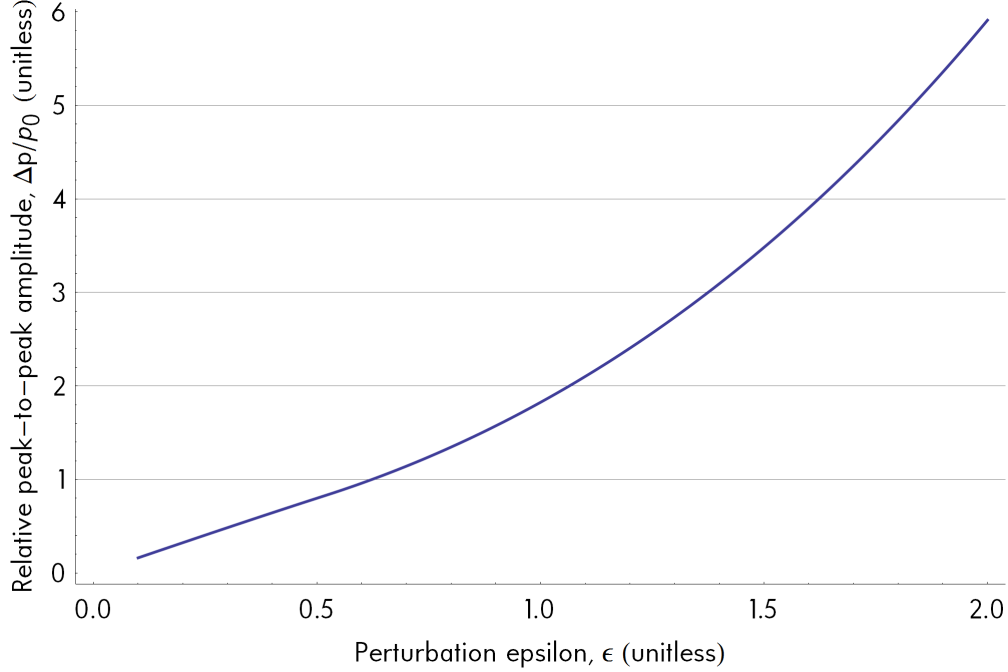


Figure 4.5: Peak-to-peak amplitudes ( $\frac{P_{max}-P_{min}}{p_0}$ ) of Maslen/Moore 1T spinning wave solution.

## 4.4 Experimental Validation

The theory was validated against experiment in two ways. First, for each test case, the experimental data and the solution with matching peak-to-peak amplitude were plotted together, as shown in Figure 4.6. The characteristic steepening shape—the shift from sinusoidal to a “U” shape—is apparent in both theory and experiment, and the two visually match fairly well through the first 3 test cases. At high amplitudes—corresponding to values of  $\epsilon$  above 0.5—it is probable that the shape began to deviate because of the truncation to third-order ( $\epsilon^5 = \epsilon^4 = \epsilon^3$  for  $\epsilon = 1$ , so higher-order terms should contribute nontrivially). Even so, the high-amplitude predictions were not as bad as would be expected, being in an invalid range of the perturbation expansion.

Second, an error was calculated between the predicted and observed waveforms. The error was taken as the root-mean-square of the fractional error of each pressure measurement  $i$  of the  $M$  test points available for a given test case:

$$\text{RMS error} = \sqrt{\frac{1}{M} \sum_i \left( \frac{P_{i,\text{experiment}} - P_{i,\text{theory}}}{P_{i,\text{experiment}}} \right)^2} \quad (4.12)$$

Table 4.1 shows this RMS error for each test point. The first three cases showed minimal error ( $< 4\%$ ), while the error grew sharply for the higher amplitude test cases: 7% and 10%.

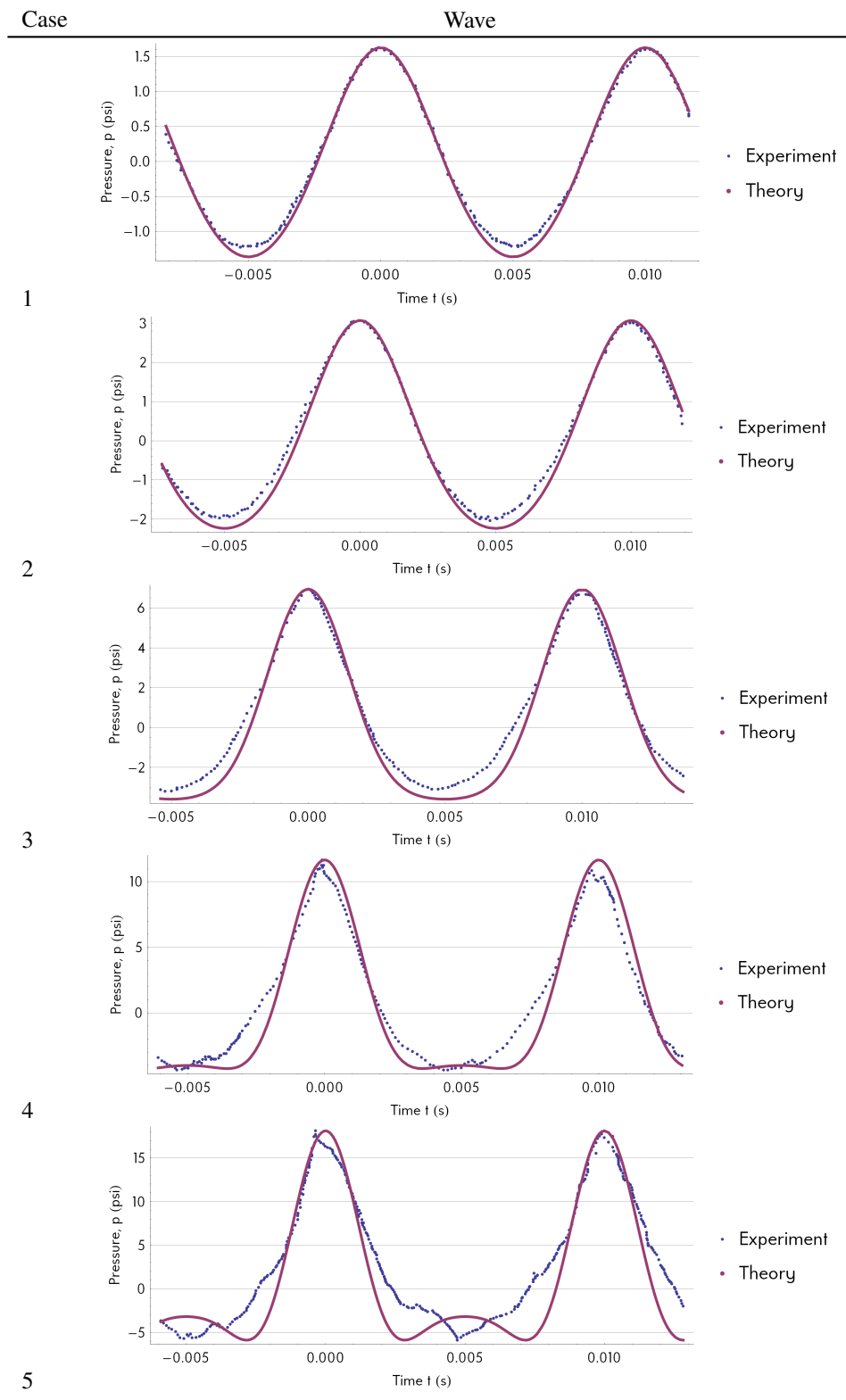


Figure 4.6: Pressure-time comparison of Maslen/Moore analytic prediction to Heidmann experiment. See Table 2.2 for information on cases.

Table 4.1: RMS error comparison of Maslen/Moore prediction to experiment

Case	Peak-to-peak $\Delta p$	(dimensionless) $\frac{\Delta p}{p_0}$	RMS err
1	2.8 psi	0.19	2.61%
2	5.5 psi	0.37	2.58%
3	10.0 psi	0.67	4.46%
4	15.5 psi	1.01	7.56%
5	24.0 psi	1.52	9.98%

## 4.5 Mode/Harmonic Decomposition

Maslen and Moore predicted a distorted shape for strong waves by directly distorting a single mode. More recent theories have predicted the distorted wave shape using a superposition of undistorted linear modes. As described in Chapter 1, a mode/harmonic deconstruction was used to address the question of whether Maslen and Moore's shifted mode shapes are different from a superposition of natural modes.

Maslen and Moore gave the pressure solution to Equation 4.1 for a spinning wave. In the following equations,  $P_{ij}$  are functions of the radial variable only, and depend on solutions to complicated inhomogeneous Bessel equations.

$$p = p_0 * (1 + \epsilon p_1 + \epsilon^2 p_2 + \epsilon^3 p_3 + \dots) \quad (4.13)$$

$$p_1 = -\gamma P_{10} \cos(\omega_n t + n\theta) \quad (4.14)$$

$$p_2 = -2\gamma P_{20} \cos(2\omega_n t + 2n\theta) - 2\gamma P_{23} \quad (4.15)$$

$$p_3 = -4\gamma P_{30} \cos(3\omega_n t + 3n\theta) - \gamma P_{34} \cos(\omega_n t + n\theta) \quad (4.16)$$

These can be analytically decomposed for their temporal harmonic content:

$$p = p_m(r, \theta) + p_0 \sum_{n=1}^3 p_{nc}(r, \theta) \cos(n\omega_n t) + p_{ns}(r, \theta) \sin(n\omega_n t) \quad (4.17)$$

$$p_m(r, \theta) = p_0 * (1 - 2\epsilon^2 \gamma P_{23}(r)) \quad (4.18)$$

$$(4.19)$$

$$p_{1c} = -\epsilon \gamma [P_{10}(r) + \epsilon^2 P_{34}(r)] \cos(n\theta) \quad (4.20)$$

$$p_{1s} = \epsilon \gamma [P_{10}(r) + \epsilon^2 P_{34}(r)] \sin(n\theta) \quad (4.21)$$

$$(4.22)$$

$$p_{2c} = -\epsilon^2 2\gamma P_{20}(r) \cos(2n\theta) \quad (4.23)$$

$$p_{2s} = \epsilon^2 2\gamma P_{20}(r) \sin(2n\theta) \quad (4.24)$$

$$(4.25)$$

$$p_{3c} = -\epsilon^3 4\gamma P_{30}(r) \cos(3n\theta) \quad (4.26)$$

$$p_{3s} = \epsilon^3 4\gamma P_{30}(r) \sin(3n\theta) \quad (4.27)$$

$$(4.28)$$

The decomposition coefficients  $a_{nm}, b_{nm}$  could then be evaluated as:

$$a_{nm} = \int p_{ms}(r, \theta) \psi_n(r, \theta) dr r d\theta \quad (4.29)$$

$$b_{nm} = \int p_{mc}(r, \theta) \psi_n(r, \theta) dr r d\theta \quad (4.30)$$

A complete set of example coefficients for a high-amplitude ( $\epsilon = 1.1$ ) simulation is given in Tables 4.2 and 4.3.

#### 4.5.1 Assumption Examined

The second of the two primary questions posed at the start concerned the quality of an assumption:

How much error is created by the mode/frequency assumption of Equation 1.32?

As described in Chapter 1, the mode/harmonic coefficients determined from Maslen and Moore's solution were used to address this question.

Note that from Tables 4.2 and 4.3, the solution does *not* exactly match a solution containing sinusoidally excited linear acoustic modes. That would require all but one element in each column to be very small or zero. However, there are multiple nontrivial coefficients in at least the  $m = 1$  column associated with the fundamental frequency. The solution *does* match the assumption that each linear acoustic mode is ringing at only one frequency: each *row* contains at most one nontrivial coefficient.

This indicated "shifted mode shapes": by summing the contributions for each column, a new mode shape was seen to be ringing at each frequency:

$$R'_m \psi'_m(\vec{r}) = \sum_n a_{nm} \psi_n(\vec{r}) \quad (4.31)$$

To quantify the change in the solution with and without the assumption, the coefficients were examined with an energy-error method as described in Chapter 1. Note that this error addressed a different question from the RMS experiment error. The RMS experiment error addressed the issue of whether the solutions agreed with physical evidence. This energy error addressed the question of whether the theory agrees with the mode/frequency assumption.

Table 4.2:  $a_{nm}$  decomposition coefficients for Maslen/Moore. Modes  $n$  are ordered by natural frequency. sin/cos indicates the  $\theta$ -coordinate spatial degeneracy. Harmonics  $m$  are numbered from  $m = 1$  for the fundamental frequency. Coefficients with values smaller than .001 are displayed as  $\lambda$ .

$m$		$m$ $a_{nm}$	0	1	2	3
0	1T0R	sin	$\lambda$	1.013060	$\lambda$	$\lambda$
1	1T0R	cos	$\lambda$	$\lambda$	$\lambda$	$\lambda$
2	2T0R	sin	$\lambda$	$\lambda$	-1.281840	$\lambda$
3	2T0R	cos	$\lambda$	$\lambda$	$\lambda$	$\lambda$
4	0T1R	-	-0.222832	$\lambda$	$\lambda$	$\lambda$
5	3T0R	sin	$\lambda$	$\lambda$	$\lambda$	0.411064
6	3T0R	cos	$\lambda$	$\lambda$	$\lambda$	$\lambda$
7	4T0R	sin	$\lambda$	$\lambda$	$\lambda$	$\lambda$
8	4T0R	cos	$\lambda$	$\lambda$	$\lambda$	$\lambda$
9	1T1R	sin	$\lambda$	-0.144673	$\lambda$	$\lambda$
10	1T1R	cos	$\lambda$	$\lambda$	$\lambda$	$\lambda$
11	2T1R	sin	$\lambda$	$\lambda$	0.028957	$\lambda$
12	2T1R	cos	$\lambda$	$\lambda$	$\lambda$	$\lambda$
13	0T2R	-	0.016478	$\lambda$	$\lambda$	$\lambda$
14	3T1R	sin	$\lambda$	$\lambda$	$\lambda$	-0.001445
15	3T1R	cos	$\lambda$	$\lambda$	$\lambda$	$\lambda$
16	1T2R	sin	$\lambda$	0.006040	$\lambda$	$\lambda$
17	1T2R	cos	$\lambda$	$\lambda$	$\lambda$	$\lambda$
18	4T1R	sin	$\lambda$	$\lambda$	$\lambda$	$\lambda$
19	4T1R	cos	$\lambda$	$\lambda$	$\lambda$	$\lambda$
20	2T2R	sin	$\lambda$	$\lambda$	-0.009517	$\lambda$
21	2T2R	cos	$\lambda$	$\lambda$	$\lambda$	$\lambda$
22	0T3R	-	-0.006684	$\lambda$	$\lambda$	$\lambda$
23	3T2R	sin	$\lambda$	$\lambda$	$\lambda$	0.004317
24	3T2R	cos	$\lambda$	$\lambda$	$\lambda$	$\lambda$
25	1T3R	sin	$\lambda$	0.011526	$\lambda$	$\lambda$
26	1T3R	cos	$\lambda$	$\lambda$	$\lambda$	$\lambda$
27	4T2R	sin	$\lambda$	$\lambda$	$\lambda$	$\lambda$
28	4T2R	cos	$\lambda$	$\lambda$	$\lambda$	$\lambda$
29	2T3R	sin	$\lambda$	$\lambda$	0.005385	$\lambda$
30	2T3R	cos	$\lambda$	$\lambda$	$\lambda$	$\lambda$
31	0T4R	-	0.005940	$\lambda$	$\lambda$	$\lambda$
32	3T3R	sin	$\lambda$	$\lambda$	$\lambda$	-0.015068
33	3T3R	cos	$\lambda$	$\lambda$	$\lambda$	$\lambda$
34	1T4R	sin	$\lambda$	-0.002542	$\lambda$	$\lambda$
35	1T4R	cos	$\lambda$	$\lambda$	$\lambda$	$\lambda$
36	4T3R	sin	$\lambda$	$\lambda$	$\lambda$	$\lambda$
37	4T3R	cos	$\lambda$	$\lambda$	$\lambda$	$\lambda$
38	2T4R	sin	$\lambda$	$\lambda$	-0.003615	$\lambda$
39	2T4R	cos	$\lambda$	$\lambda$	$\lambda$	$\lambda$
40	3T4R	sin	$\lambda$	$\lambda$	$\lambda$	$\lambda$
41	3T4R	cos	$\lambda$	$\lambda$	$\lambda$	$\lambda$
42	4T4R	sin	$\lambda$	$\lambda$	$\lambda$	$\lambda$
43	4T4R	cos	$\lambda$	$\lambda$	$\lambda$	$\lambda$



Table 4.3:  $b_{nm}$  decomposition coefficients for Maslen/Moore. Modes  $n$  are ordered by natural frequency. sin/cos indicates the  $\theta$ -coordinate spatial degeneracy. Harmonics  $m$  are numbered from  $m = 1$  for the fundamental frequency. Coefficients with values smaller than .001 are displayed as  $\lambda$ .

$m$	$m$	$b_{nm}$	0	1	2	3
0	1T0R	sin	0	$\lambda$	$\lambda$	$\lambda$
1	1T0R	cos	0	-1.013130	$\lambda$	$\lambda$
2	2T0R	sin	0	$\lambda$	$\lambda$	$\lambda$
3	2T0R	cos	0	$\lambda$	1.282640	$\lambda$
4	0T1R	-	0	$\lambda$	$\lambda$	$\lambda$
5	3T0R	sin	0	$\lambda$	$\lambda$	$\lambda$
6	3T0R	cos	0	$\lambda$	$\lambda$	-0.410909
7	4T0R	sin	0	$\lambda$	$\lambda$	$\lambda$
8	4T0R	cos	0	$\lambda$	$\lambda$	$\lambda$
9	1T1R	sin	0	$\lambda$	$\lambda$	$\lambda$
10	1T1R	cos	0	0.144722	$\lambda$	$\lambda$
11	2T1R	sin	0	$\lambda$	$\lambda$	$\lambda$
12	2T1R	cos	0	$\lambda$	-0.029253	$\lambda$
13	0T2R	-	0	$\lambda$	$\lambda$	$\lambda$
14	3T1R	sin	0	$\lambda$	$\lambda$	$\lambda$
15	3T1R	cos	0	$\lambda$	$\lambda$	0.001448
16	1T2R	sin	0	$\lambda$	$\lambda$	$\lambda$
17	1T2R	cos	0	-0.006157	$\lambda$	$\lambda$
18	4T1R	sin	0	$\lambda$	$\lambda$	$\lambda$
19	4T1R	cos	0	$\lambda$	$\lambda$	$\lambda$
20	2T2R	sin	0	$\lambda$	$\lambda$	$\lambda$
21	2T2R	cos	0	$\lambda$	0.009648	$\lambda$
22	0T3R	-	0	$\lambda$	$\lambda$	$\lambda$
23	3T2R	sin	0	$\lambda$	$\lambda$	$\lambda$
24	3T2R	cos	0	$\lambda$	$\lambda$	-0.004337
25	1T3R	sin	0	$\lambda$	$\lambda$	$\lambda$
26	1T3R	cos	0	-0.011484	$\lambda$	$\lambda$
27	4T2R	sin	0	$\lambda$	$\lambda$	$\lambda$
28	4T2R	cos	0	$\lambda$	$\lambda$	$\lambda$
29	2T3R	sin	0	$\lambda$	$\lambda$	$\lambda$
30	2T3R	cos	0	$\lambda$	-0.005356	$\lambda$
31	0T4R	-	0	$\lambda$	$\lambda$	$\lambda$
32	3T3R	sin	0	$\lambda$	$\lambda$	$\lambda$
33	3T3R	cos	0	$\lambda$	$\lambda$	0.015062
34	1T4R	sin	0	$\lambda$	$\lambda$	$\lambda$
35	1T4R	cos	0	0.002480	$\lambda$	$\lambda$
36	4T3R	sin	0	$\lambda$	$\lambda$	$\lambda$
37	4T3R	cos	0	$\lambda$	$\lambda$	$\lambda$
38	2T4R	sin	0	$\lambda$	$\lambda$	$\lambda$
39	2T4R	cos	0	$\lambda$	0.003672	$\lambda$
40	3T4R	sin	0	$\lambda$	$\lambda$	$\lambda$
41	3T4R	cos	0	$\lambda$	$\lambda$	$\lambda$
42	4T4R	sin	0	$\lambda$	$\lambda$	$\lambda$
43	4T4R	cos	0	$\lambda$	$\lambda$	$\lambda$

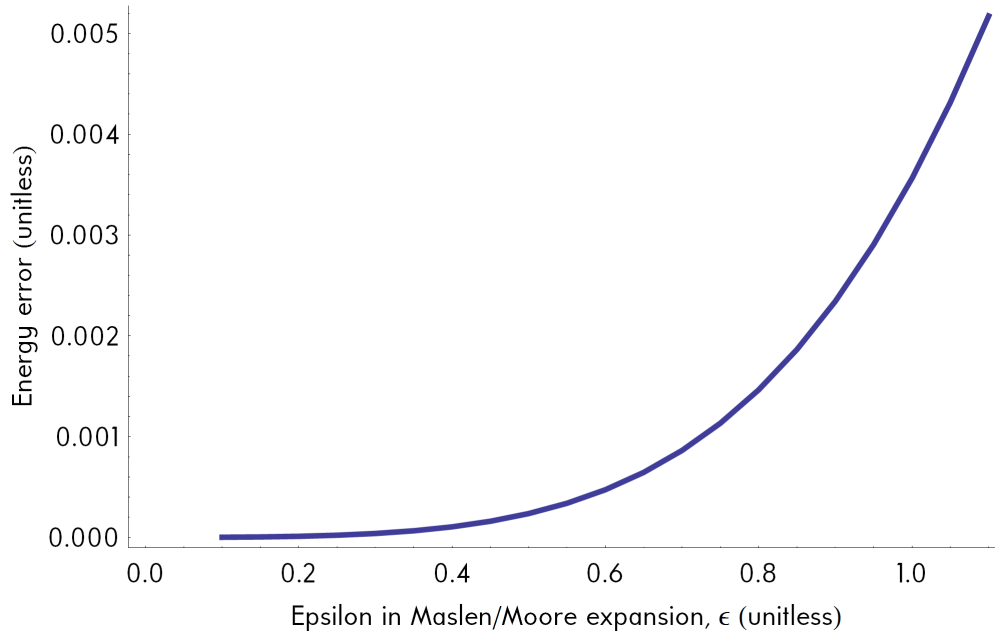


Figure 4.7: Plot of energy error versus perturbation  $\epsilon$ .

Figure 4.7 shows this energy-error varying with the perturbation parameter  $\epsilon$ . The maximum error shown, approximately 0.5%, indicated that at very large amplitudes, the energy stored in nondominant modes in Maslen and Moore's solution is minimal. This means that while the mode shapes do shift, those shifted mode shapes do not significantly change the solution.

## 4.6 DC Valley

The  $m = 0$  columns of Tables 4.2 and 4.3 show a nontrivial component of the solution with zero-frequency. This component was apparent from Equation 4.7, but was not anticipated by the other theories motivating this work.

To understand how this steady component contributes to the overall wave, the wave was plotted with and without this component, as in Figure 4.8. The oscillatory component of that figure spins around the chamber, while the steady component does not change with time. The effect of adding the steady component to the oscillatory component is to flatten out a saddle-shaped region near the center of the wave, making the wave a steeper surface.

## 4.7 Summary

Maslen and Moore's solution was examined and recreated, then applied to the model problem. The solution was validated to an accuracy of 4% within the validity of the perturbation expansion ( $\epsilon < .5$ ), and to an accuracy of 10% to the limit of physically accurately solutions ( $\epsilon = 1.5$ ).

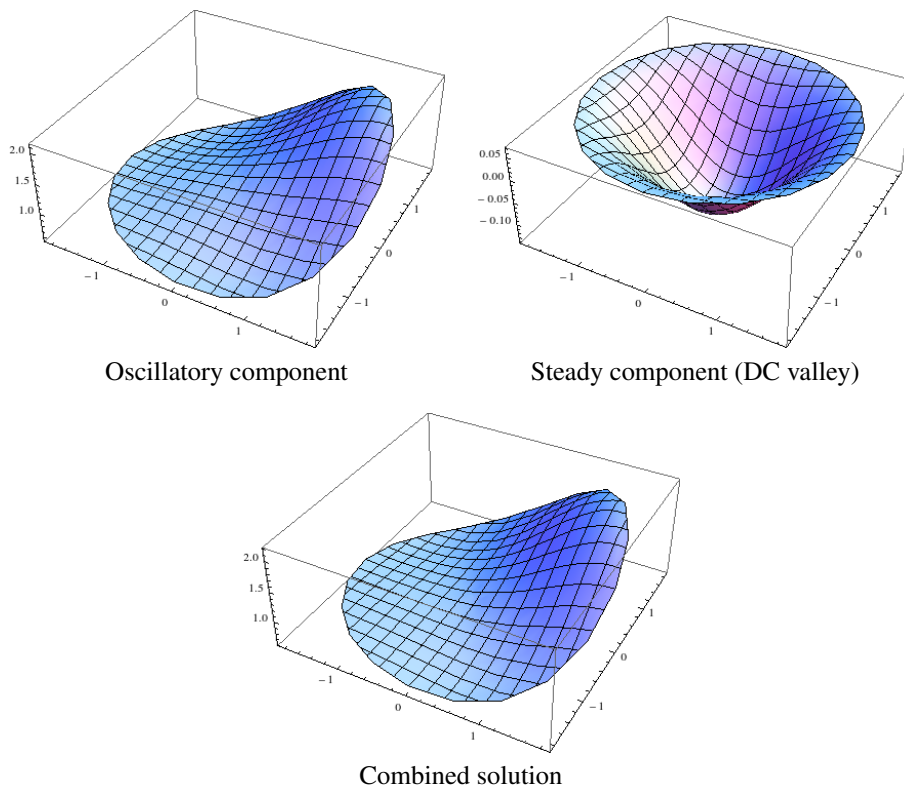


Figure 4.8: DC valley in Maslen and Moore. Surface height indicates pressure value (nondimensional:  $p/p_0$ ), horizontal axes are  $x, y$  coordinates.

Maslen and Moore's solution was found to be approximated well by a four-mode expansion with one frequency per mode:  $< 0.5\%$  of total energy is missed by such an expansion at  $\epsilon = 1.1$ .

Finally, the solution was noted to contain a time-independent, spatially distributed component given primarily by the OT1R mode.

# Chapter 5

## Theory 3: Oscillators

By assuming a general time dependence for each mode (instead of sinusoidal time dependence), several investigators [12] [23] [48] have found coupled, second-order ordinary differential equations governing the system.

These second-order equations take the form of a set of damped, driven, nonlinearly coupled harmonic oscillators. This led to a new physical explanation of the presence of harmonics in strong waves: a “harmonic cascade” through nonlinearly coupled oscillators.

Previously, there were few direct comparisons between this theoretical approach and experiment. Here, the theory was applied to the model IT spinning wave problem and validated against experiment.

This oscillator approach also allowed further evaluation of the mode/frequency assumption. The generalized time functions allowed the solutions to have shifted modes and multiple-frequencies-per-mode. Applying the double-decomposition of Chapter 1 to these solutions enabled quantification of the assumption to more harmonics than the solution offered by Maslen and Moore (Chapter 4).

### 5.1 Theory

The nonlinear oscillator equations of Culick and Yang [23] were used to simulate the model problem.

#### 5.1.1 Expansion

The fluid dynamic variables were assumed to take the form of an expansion in the linear acoustic modes:

$$p_1 = p_0 \sum_{n=1}^{\infty} \eta_n(t) \psi_n(\vec{r}) \quad (5.1)$$

$$\vec{u}_1 = \sum_{n=1}^{\infty} \frac{1}{\gamma k_n^2} \dot{\eta}_n(t) \nabla \psi_n(\vec{r}) \quad (5.2)$$

The other fluid dynamic variables were also computed in terms of  $\eta_n$  and  $\psi_n$ .

No assumption was made about the form of time dependence,  $\eta_n(t)$ . The goal of this approach was to find governing equations for these functions, then solve for them numerically. The resulting solutions to  $\eta_n(t)$  could have any structure allowed by the equations. It is not constrained (as is the usual practice) to a sinusoidal function with one frequency and slowly varying amplitude and phase. In particular,  $\eta_n(t)$  could have any number of harmonics, or it could even have continuous nonharmonic frequency content.

### 5.1.2 Governing Equations

Restated from Culick and Yang [23]:

$$\begin{aligned} \ddot{\eta}_n + \omega_n^2 \eta_n = & - \sum_{m,l=1}^{\infty} \dot{\eta}_m \dot{\eta}_l \frac{1}{\gamma A_n \kappa_l^2 \kappa_m^2} \left( \frac{1}{2} (\kappa_n^2 - \kappa_m^2 + \kappa_l^2) B_{nml} + \kappa_l^2 B_{nml} - \gamma \kappa_m^2 \kappa_l^2 C_{nml} \right) \\ & - \sum_{m,l=1}^{\infty} \eta_m \eta_l \frac{-a_0^2}{\gamma A_n} \left( -B_{nml} + \kappa_l^2 C_{nml} + B_{nml} - \gamma \kappa_l^2 C_{nml} \right) \end{aligned} \quad (5.3)$$

with the spatial dependence reduced to coefficients:

$$A_n = \int_V \psi_n^2 dV \quad (5.4)$$

$$B_{nml} = \int_V \psi_n \nabla \psi_m \cdot \nabla \psi_l dV \quad (5.5)$$

$$C_{nml} = \int_V \psi_n \psi_m \psi_l dV \quad (5.6)$$

Note that  $B_{nml}, C_{nml}$  are the same as  $M_{nml}, N_{nml}$  from Chapter 3. Values calculated for one theory were reused for the other.

## 5.2 Physical Explanation

One of the two questions posed in the introduction concerns the “why” of cylindrical harmonics:

Why do cylindrical waves steepen into apparent harmonics, despite the natural resonances being nonharmonic?

A new explanation was developed from the nonlinear oscillator theory:

When only one frequency is driven or has positive feedback in a set of nonlinearly coupled oscillators, the nonlinear coupling cascades harmonics of that frequency through the system as a form of driving on each individual oscillator.

## 5.2.1 The Harmonic Cascade

Consider Culick's nonlinear oscillator equation:

$$\ddot{\eta}_n + \omega_n^2 \eta_n - 2\alpha_n \dot{\eta}_n = \sum_{m=1}^{n-1} (A_{nm} \eta_m \eta_{n-m} + B_{nm} \dot{\eta}_m \dot{\eta}_{n-m}) + \sum_{m=1}^{\infty} (C_{nm} \eta_m \eta_{n+m} + D_{nm} \dot{\eta}_m \dot{\eta}_{n+m}) \quad (5.7)$$

Now suppose that the first mode,  $\eta_1$ , is being driven by  $\sin(\omega t)$ , making no assumptions about  $\omega$  (i.e., it might not be a natural frequency of the system at all). Assume all initial conditions are zero:  $\eta_n(0) = \dot{\eta}_n(0) = 0$ .

*Induction: Step 0.* Consider the first mode at  $t = 0$ . The equation of motion simplifies to

$$\ddot{\eta}_1 + \omega_1^2 \eta_1 - 2\alpha_1 \dot{\eta}_1 = \sin(\omega t) + \sum_{m=1}^{1-1} (A_{1m} \eta_m \eta_{1-m} + B_{1m} \dot{\eta}_m \dot{\eta}_{1-m}) + \sum_{m=1}^{\infty} (C_{1m} \eta_m \eta_{1+m} + D_{1m} \dot{\eta}_m \dot{\eta}_{1+m}) \quad (5.8)$$

$$= \sin(\omega t) \quad (5.9)$$

because the first sum has no terms, and in the second sum all terms are initially zero.<sup>1</sup> Solve this equation, to obtain the particular solution to the damped driven simple harmonic oscillator:

$$\eta_1(t) = a_1 \sin(\omega t + \theta_1) \quad (5.10)$$

Likewise, since all the higher modes simplify to a simple harmonic oscillator equation, but without forcing and with zero initial conditions, those modes have only the trivial solutions at this time:

$$\eta_n(t) = 0 \quad , n > 1 \quad (5.11)$$

*Induction: Step 1.* Consider the system at some incrementally later time,  $t'$ . The equation and solution for the first mode remain unchanged.

Consider the second mode. Since the first mode (and only the first mode) now has a non-zero solution, the equation of motion for the second mode becomes

$$\ddot{\eta}_2 + \omega_2^2 \eta_2 - 2\alpha_2 \dot{\eta}_2 = \sum_{m=1}^{2-1} (A_{2m} \eta_m \eta_{2-m} + B_{2m} \dot{\eta}_m \dot{\eta}_{2-m}) + \sum_{m=2}^{\infty} (C_{2m} \eta_m \eta_{2+m} + D_{2m} \dot{\eta}_m \dot{\eta}_{2+m}) \quad (5.12)$$

$$= A_{21} \eta_1 \eta_1 \quad (5.13)$$

$$= A_{21} a_1^2 \sin^2(\omega t + \theta_1) \quad (5.14)$$

$$= S_1 + S_2 \sin(2\omega t + \theta_2) \quad (5.15)$$

where all terms on the right-hand-side not involving the first mode are uniformly zero.

<sup>1</sup>This is the essential assumption of the proof, that the system can be considered in small periods of time.

Setting  $M = 1$  (anticipating the next step of the proof), the solution to this equation takes the form

$$\eta_2(t) = \sum_{k=0}^{2M} a_{2k} \sin(k\omega t + \theta_2 k t) \quad (5.16)$$

Note that  $\eta_1$  can be written in this form as well.

Again, since all higher modes contain no non-zero terms on the right hand side of the simple harmonic oscillator equation, those modes have only the trivial solution:

$$\eta_n(t) = 0, \quad n > 2 \quad (5.17)$$

*Induction: Step N.* Now consider the system after some time  $t'$ . The modes are ringing according to

$$\eta_n(t) = \begin{cases} \sum_{k=0}^M a_n k \sin(k\omega t + \theta_n k), & n \leq N \\ 0, & n > N \end{cases} \quad (5.18)$$

Consider a mode  $n \leq 2N$ .

$$\ddot{\eta}_n + \omega_n^2 \eta_n - 2\alpha_n \dot{\eta}_n = \sum_{m=1}^{n-1} (A_{nm} \eta_m \eta_{n-m} + B_{nm} \dot{\eta}_m \dot{\eta}_{n-m}) + \sum_{m=1}^{\infty} (C_{nm} \eta_m \eta_{n+m} + D_{nm} \dot{\eta}_m \dot{\eta}_{n+m}) \quad (5.19)$$

$$= \sum_{m=1}^{n-1} (A_{nm} \eta_m \eta_{n-m} + B_{nm} \dot{\eta}_m \dot{\eta}_{n-m}) + \sum_{m=1}^{2N} (C_{nm} \eta_m \eta_{n+m} + D_{nm} \dot{\eta}_m \dot{\eta}_{n+m}) \quad (5.20)$$

$$= \sum_{m=1}^{2N} \sum_{j,k=0}^M R_{nmkj} \sin(j\omega t) \sin(k\omega t) \quad (5.21)$$

$$= \sum_{m=1}^{2N} \sum_{l=0}^{2M} R'_{nml} \sin(l\omega t + \theta_n ml) \quad (5.22)$$

This has a solution of the form

$$\eta_n(t) = \sum_{k=0}^{2M} a_n k \sin(k\omega t + \theta_n k), \quad n \leq 2N \quad (5.23)$$

For  $n > 2N$ , all the right-hand-side terms are zero, and again the trivial solutions

$$\eta_n(t) = 0, \quad n > 2N \quad (5.24)$$

result.

Thus, given that at a time  $t$  up to  $N$  modes are ringing at only harmonics of the driven frequency, then after time  $t$ , up to  $2N$  modes are ringing at only harmonics of the driven frequency, and all other modes will have no excitation.

By induction, only harmonics of the driven system ever appear.



## 5.2.2 Generalization

This argument generalizes to the situation where at most  $M$  modes either have positive growth (are “linearly unstable”) or are directly driven. Each mode appears as a damped-driven harmonic oscillator. Only the natural frequencies of unstable modes will give rise to limit cycles; all other frequencies will decay. This is a property of the homogeneous, also called the transient, solutions associated with non-driven natural frequencies.

With the only surviving frequencies belonging to unstable or driven modes, the sum and difference frequencies of those modes will survive due to the *nonlinear, coupling* nature of the inter-modal driving terms. Sum and difference frequencies of each mode with itself lead to harmonics. The case of multiple unstable or driven frequencies leads to chaotic-looking solutions<sup>2</sup>.

It is out of the scope of this chapter to address the question of whether and to what degree multiple unstable modes have been observed in combustion instabilities. The things to look for are: noisy or random pressure signatures that transform to a more ordered spectrum consisting of a few dominant frequencies, their harmonics, and their sum/difference frequencies.

## 5.3 Procedure

Solving Equation 5.3 numerically for the  $\eta_n$  functions of time was a multi-stage process:

- Numerically compute values for frequency for each mode, and order the modes by frequency ( $\omega_n \leq \omega_{n+1}$ ).
- Numerically compute values for the tensors  $A_n, B_{nml}, C_{nml}$  by numerically integrating the appropriate functions ( $\psi_n, \nabla\psi_n$ ).
- Program the equations and initial conditions.
- Numerically integrate the equations forward in time (with e.g. a Runge-Kutta routine).<sup>3</sup>

Initially, this was done using initial conditions corresponding to a spinning wave (the first two modes started with out-of-phase initial conditions, all other modes zero). However, the results appeared chaotic. It was determined that the natural (nonharmonic) frequencies of several of the non-fundamental modes were ringing indefinitely with limit cycle amplitudes. Therefore, the equations were altered to be damped-driven-nonlinear oscillators, as follows:

$$\ddot{\eta}_n - \alpha_n \dot{\eta}_n + \omega_n^2 \eta_n = F_n - \sum_{m,l=1}^{\infty} \dot{\eta}_m \dot{\eta}_l \frac{1}{\gamma A_n \kappa_l^2 \kappa_m^2} \left( \frac{1}{2} (\kappa_n^2 - \kappa_m^2 + \kappa_l^2) B_{nml} + \kappa_l^2 B_{nml} - \gamma \kappa_m^2 \kappa_l^2 C_{nml} \right) \quad (5.25)$$

with  $\alpha_n = D\omega_n^2$ . Driving a spinning wave then consisted of uniformly zero initial conditions, with  $F_1 = F \sin(\omega_1 t)$ ,  $F_2 = F \cos(\omega_2 t)$ ,  $F_n = 0$  ( $n > 2$ ), remembering that  $\omega_1 = \omega_2$  because the first two modes are the sin and cos solutions of the same Bessel function and root.

This, then, added two steps to the simulations:

<sup>2</sup>Chaotic-looking signals are signals which appear to be noisy or random with possibly some periodicity, but which result from structured deterministic systems.

<sup>3</sup>Integration was performed with the default routine of Mathematica 9’s “ndsolve” function. The default routine uses an adaptive Runge-Kutta solver for initial-value-problems with known Jacobians. Other integration routines were tried, with no difference to the solution.

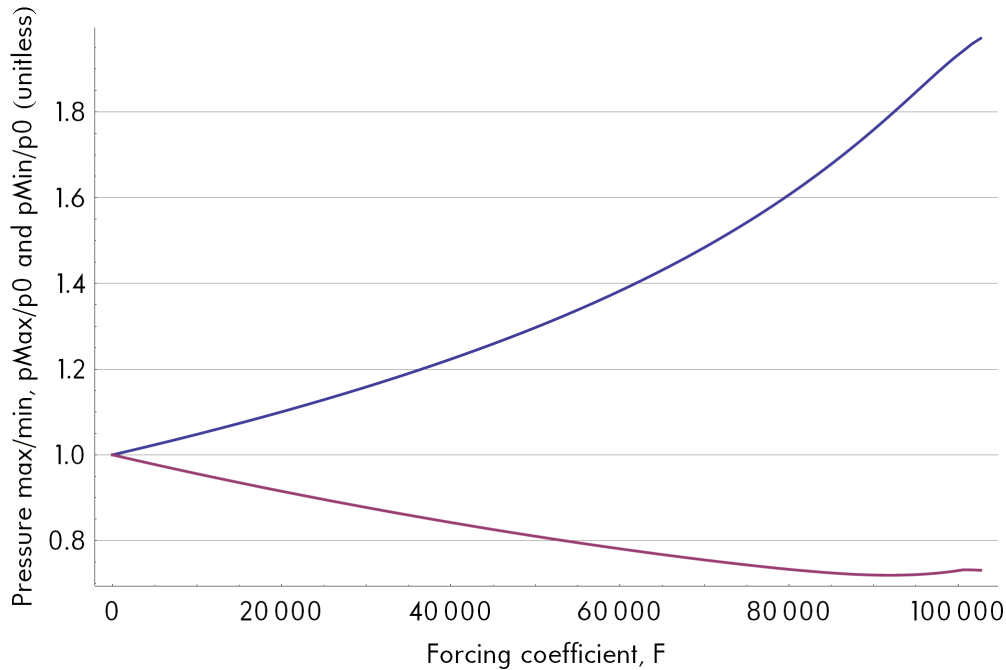


Figure 5.1: Minimum and maximum relative pressures ( $\frac{p_{max}}{p_0}$ ,  $\frac{p_{min}}{p_0}$ ) of oscillator 1T spinning wave solution.

- Determine appropriate values for  $D$ .
- Perform the full simulation process for varying values of  $F$ .

All of this was accomplished using Mathematica 9, and the complete simulation results for one value of  $F$  are presented in Appendix C.

### 5.3.1 Driving vs. Amplitude

Simulations for the 1T spinning mode were run with varying values of forcing amplitude  $F$ . The first 44 spatial mode shapes were included (up to 5 modal diameters and 5 nodal circles, with  $\sin(\theta)$ ,  $\cos(\theta)$  degeneracies). The solutions became numerically unstable above values of  $F$  corresponding to peak-to-peak amplitudes of  $1.2p_0$ .

Figure 5.1 shows the progression of maximum and minimum pressure as  $F$  is increased from zero. Note that the minimum pressure never goes below  $0.7p_0$ , which is quite different from the simulations of Chapters 3 and 4. This suggests that a different numerical instability is limiting the process. The specific error attained was “step size is effectively zero”. As this numerical technique captured the oscillation directly in the numerical solution, this suggested that the solution was varying too fast for the solver’s precision.<sup>4</sup>

Peak-to-peak amplitudes were calculated for the limit cycle wave of each simulation run. Figure 5.2 shows these peak-to-peak amplitudes plotted against the forcing constant,  $F$ . The maximum amplitude attained with this method was  $1.2p_0$ , significantly lower than the  $2.5p_0$  attained with the theories of Chapters 3 and 4.

<sup>4</sup>A 64-bit version of Mathematica 9 was employed using machine precision: 64-bit.

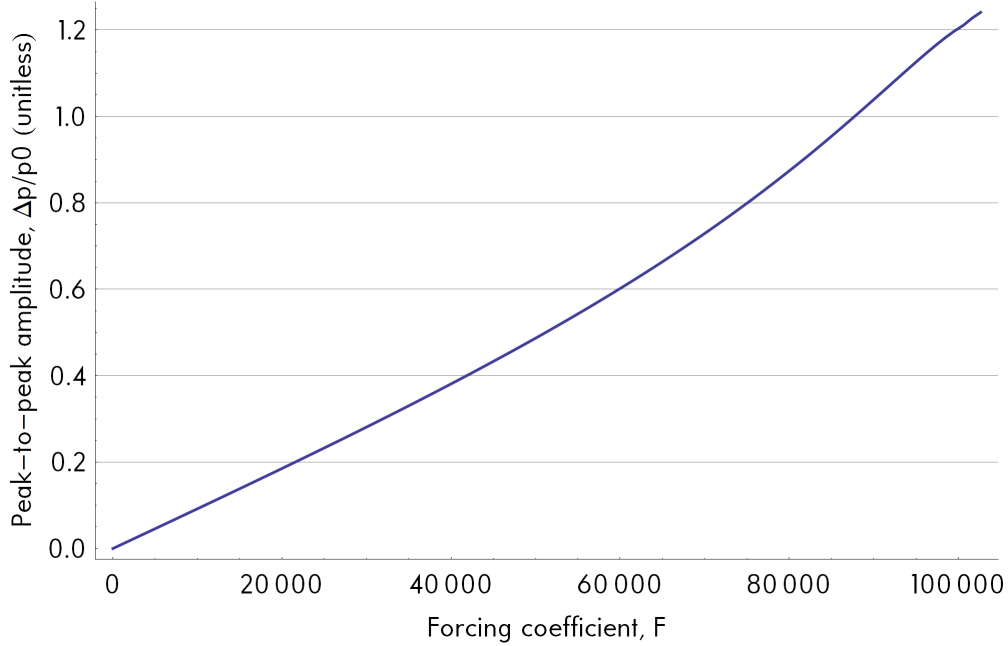


Figure 5.2: Peak-to-peak amplitudes ( $\frac{P_{max}-P_{min}}{p_0}$ ) of oscillator 1T spinning wave solution.

## 5.4 Experimental Validation

Note that the maximum attained peak-to-peak amplitude with the oscillator theory was  $1.2p_0$ , which excludes one of the test cases.

The theory was validated against the model experiment of Chapter 2 in two ways. First, for each test case, the experimental data and the solution with matching peak-to-peak amplitude were plotted together, as shown in Figure 5.3. The characteristic steepening shape—the shift from sinusoidal to a “U” shape—is apparent in both theory and experiment, and the two visually match fairly well for all four test cases. Though this theory was unable to model the highest-amplitude case, this nonlinear oscillator approach produced waveforms that were more visually similar to the experiments than the waveforms produced by the theories of Chapters 3, 4 and 6.

Second, an error was calculated between the predicted and observed waveforms. The error was taken as the root-mean-square of the fractional error of each pressure measurement  $i$  of the  $M$  test points available for a given test case:

$$\text{RMS error} = \sqrt{\frac{1}{M} \sum_i \left( \frac{P_{i,experiment} - P_{i,theory}}{P_{i,experiment}} \right)^2} \quad (5.26)$$

Table 5.1 shows this RMS error for each test point. The first three cases showed minimal error ( $< 4\%$ ), while the error grew somewhat for the higher amplitude case to  $7\%$ .

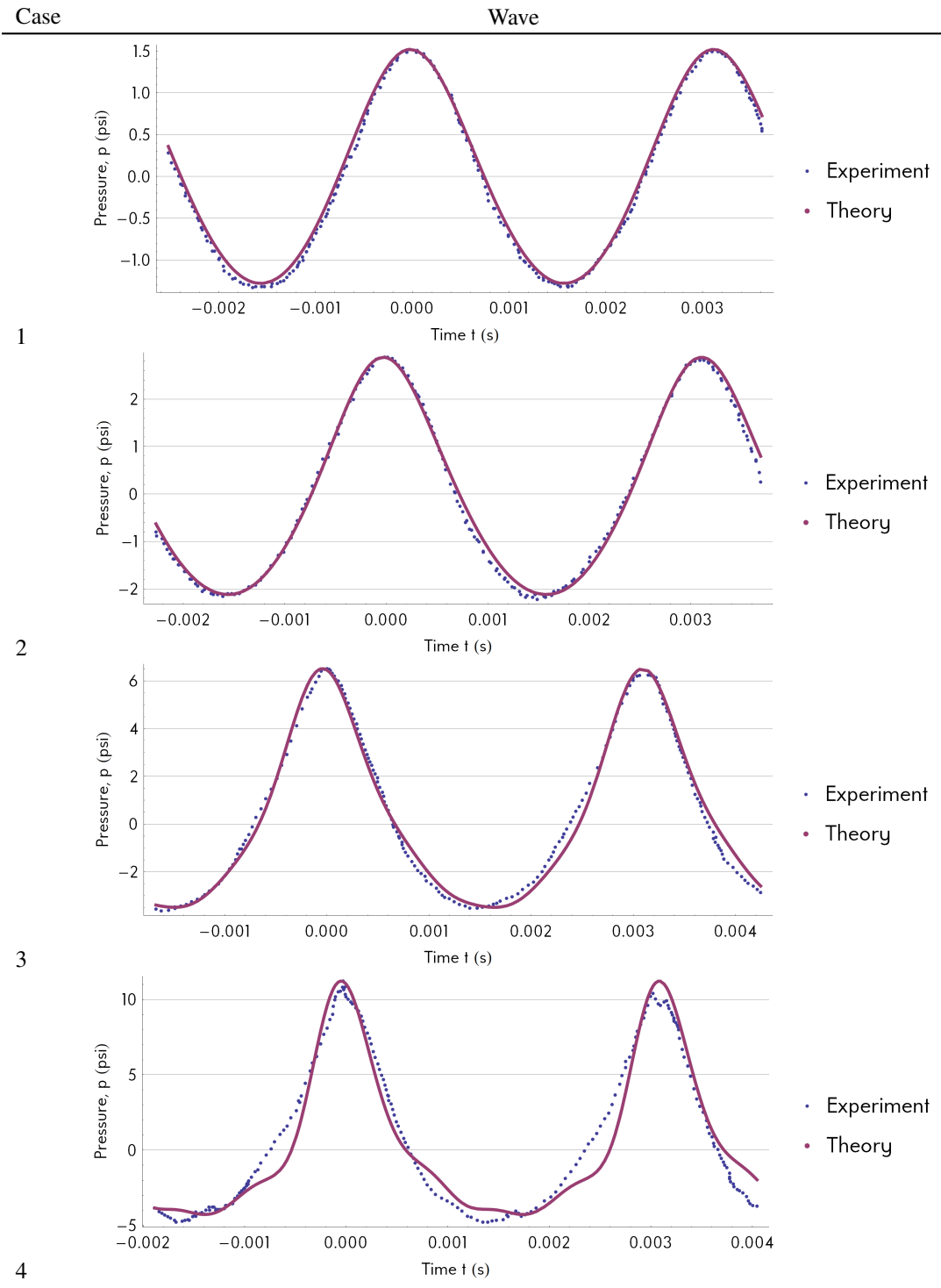


Figure 5.3: Pressure-time comparison of nonlinear oscillator prediction (in red) to Heidmann experiment (in blue). See Table 2.2 for information on cases.

## 5.5 Mode/Harmonic Decomposition

The mode/harmonic decomposition seeks to put the solution in terms of coefficients  $a_{nm}$ ,  $b_{nm}$  as in Equation 1.44:

$$p(\vec{r}, t) = \sum_{n,m=1}^{\infty} (a_{nm} \sin(m\omega t) + b_{nm} \cos(m\omega t))\psi_n(\vec{r}) \quad (5.27)$$

The expansion assumed in Equation 5.1 was already halfway in this form:

$$p_1 = p_0 \sum_{n=1}^{\infty} \eta_n(t)\psi_n(\vec{r}) \quad (5.28)$$

with the only required calculation being the temporal decomposition:

$$a_{nm} = \frac{\int_{t=0}^{\tau} \sin(m\omega t)\eta_n(t)dt}{\int_{t=0}^{\tau} \sin^2(m\omega t)dt} \quad (5.29)$$

$$b_{nm} = \frac{\int_{t=0}^{\tau} \cos(m\omega t)\eta_n(t)dt}{\int_{t=0}^{\tau} \cos^2(m\omega t)dt} \quad (5.30)$$

with  $\tau$  the period of oscillation. Tables 5.2 and 5.3 show an example set of decomposition coefficients for one oscillator simulation.

### 5.5.1 Assumption Examined

The second of the two primary questions posed at the start of the work concerned the quality of an assumption:

How much error is created by the mode/frequency assumption of Equation 1.32?

To restate the mode/frequency assumption: the total nonlinear wave solution can be described as a superposition of linear acoustic modes, each ringing at a single frequency. As described in Chapter 1, the mode/harmonic coefficients determined from the oscillator solution were used to address this question.

Table 5.1: RMS error comparison of oscillator prediction to experiment

Peak-to-peak Case	(dimensionless) $\Delta p$	RMS err $\frac{\Delta p}{p_0}$	
1	2.8 psi	0.19	2.5%
2	5.5 psi	0.37	2.7%
3	10.0 psi	0.67	3.9%
4	15.5 psi	1.01	7.4%
5	24.0 psi	1.52	Unknown

Table 5.2:  $a_{nm}$  decomposition coefficients for nonlinear oscillators. Modes  $n$  are ordered by natural frequency. sin/cos indicates the  $\theta$ -coordinate spatial degeneracy. Harmonics  $m$  are numbered from  $m = 1$  for the fundamental frequency. Coefficients with values smaller than .001 are displayed as  $\lambda$ .

$m$	$m$	$a_{nm}$	1	2	3	4	5	6	7	8	9
0	1T0R	sin	-0.105	-0.001	$\lambda$	$\lambda$	$\lambda$	$\lambda$	$\lambda$	$\lambda$	$\lambda$
1	1T0R	cos	0.684	-0.001	$\lambda$	$\lambda$	$\lambda$	$\lambda$	$\lambda$	$\lambda$	$\lambda$
2	2T0R	sin	-0.001	-0.436	$\lambda$	$\lambda$	$\lambda$	$\lambda$	$\lambda$	$\lambda$	$\lambda$
3	2T0R	cos	$\lambda$	0.016	-0.002	0.002	$\lambda$	$\lambda$	$\lambda$	$\lambda$	$\lambda$
4	0T1R	-	$\lambda$	0.083	$\lambda$	$\lambda$	$\lambda$	$\lambda$	$\lambda$	$\lambda$	$\lambda$
5	3T0R	sin	-0.002	-0.004	-0.037	$\lambda$	-0.002	$\lambda$	$\lambda$	$\lambda$	$\lambda$
6	3T0R	cos	-0.013	0.010	-0.297	$\lambda$	$\lambda$	$\lambda$	$\lambda$	$\lambda$	$\lambda$
7	4T0R	sin	-0.004	0.013	-0.001	0.199	$\lambda$	$\lambda$	$\lambda$	$\lambda$	$\lambda$
8	4T0R	cos	-0.003	-0.003	-0.002	-0.035	$\lambda$	-0.002	$\lambda$	$\lambda$	$\lambda$
9	1T1R	sin	-0.025	0.003	-0.022	0.001	$\lambda$	$\lambda$	$\lambda$	$\lambda$	$\lambda$
10	1T1R	cos	-0.062	0.002	0.031	0.002	$\lambda$	$\lambda$	$\lambda$	$\lambda$	$\lambda$
11	2T1R	sin	$\lambda$	0.042	0.002	-0.040	-0.002	$\lambda$	$\lambda$	$\lambda$	$\lambda$
12	2T1R	cos	$\lambda$	-0.005	$\lambda$	0.034	0.001	$\lambda$	$\lambda$	$\lambda$	$\lambda$
13	0T2R	-	$\lambda$	-0.003	$\lambda$	0.005	$\lambda$	$\lambda$	$\lambda$	$\lambda$	$\lambda$
14	3T1R	sin	-0.004	$\lambda$	$\lambda$	$\lambda$	-0.057	-0.001	$\lambda$	$\lambda$	$\lambda$
15	3T1R	cos	$\lambda$	$\lambda$	0.025	0.001	-0.033	-0.001	$\lambda$	$\lambda$	$\lambda$
16	1T2R	sin	0.003	$\lambda$	-0.009	$\lambda$	-0.007	$\lambda$	$\lambda$	$\lambda$	$\lambda$
17	1T2R	cos	0.023	$\lambda$	-0.007	$\lambda$	$\lambda$	$\lambda$	$\lambda$	$\lambda$	$\lambda$
18	4T1R	sin	$\lambda$	$\lambda$	$\lambda$	0.012	$\lambda$	0.025	$\lambda$	$\lambda$	$\lambda$
19	4T1R	cos	$\lambda$	-0.003	$\lambda$	$\lambda$	$\lambda$	-0.053	$\lambda$	$\lambda$	$\lambda$
20	2T2R	sin	$\lambda$	-0.011	$\lambda$	0.008	0.001	-0.008	$\lambda$	$\lambda$	$\lambda$
21	2T2R	cos	$\lambda$	$\lambda$	$\lambda$	-0.013	$\lambda$	$\lambda$	$\lambda$	$\lambda$	$\lambda$
22	0T3R	-	$\lambda$	-0.003	$\lambda$	-0.002	$\lambda$	$\lambda$	$\lambda$	$\lambda$	$\lambda$
23	3T2R	sin	0.001	$\lambda$	$\lambda$	$\lambda$	0.007	$\lambda$	-0.007	$\lambda$	$\lambda$
24	3T2R	cos	$\lambda$	$\lambda$	-0.001	$\lambda$	0.009	$\lambda$	-0.010	$\lambda$	$\lambda$
25	1T3R	sin	$\lambda$	$\lambda$	0.005	$\lambda$	$\lambda$	$\lambda$	$\lambda$	$\lambda$	$\lambda$
26	1T3R	cos	-0.009	$\lambda$	0.004	$\lambda$	-0.002	$\lambda$	$\lambda$	$\lambda$	$\lambda$
27	4T2R	sin	$\lambda$	$\lambda$	$\lambda$	$\lambda$	$\lambda$	0.016	$\lambda$	0.008	$\lambda$
28	4T2R	cos	$\lambda$	$\lambda$	$\lambda$	$\lambda$	$\lambda$	-0.002	$\lambda$	-0.010	$\lambda$
29	2T3R	sin	$\lambda$	0.004	$\lambda$	-0.003	$\lambda$	0.003	$\lambda$	$\lambda$	$\lambda$
30	2T3R	cos	$\lambda$	$\lambda$	$\lambda$	0.003	$\lambda$	-0.002	$\lambda$	$\lambda$	$\lambda$
31	0T4R	-	$\lambda$	0.002	$\lambda$	$\lambda$	$\lambda$	$\lambda$	$\lambda$	$\lambda$	$\lambda$
32	3T3R	sin	$\lambda$	$\lambda$	$\lambda$	$\lambda$	$\lambda$	$\lambda$	$\lambda$	$\lambda$	$\lambda$
33	3T3R	cos	$\lambda$	$\lambda$	0.002	$\lambda$	0.003	$\lambda$	0.003	$\lambda$	-0.002
34	1T4R	sin	$\lambda$	$\lambda$	-0.001	$\lambda$	$\lambda$	$\lambda$	$\lambda$	$\lambda$	$\lambda$
35	1T4R	cos	0.004	$\lambda$	-0.002	$\lambda$	0.001	$\lambda$	$\lambda$	$\lambda$	$\lambda$
36	4T3R	sin	$\lambda$	$\lambda$	$\lambda$	-0.001	$\lambda$	$\lambda$	$\lambda$	0.005	$\lambda$
37	4T3R	cos	$\lambda$	$\lambda$	$\lambda$	$\lambda$	$\lambda$	$\lambda$	$\lambda$	0.002	$\lambda$
38	2T4R	sin	$\lambda$	-0.002	$\lambda$	$\lambda$	$\lambda$	$\lambda$	$\lambda$	$\lambda$	$\lambda$
39	2T4R	cos	$\lambda$	$\lambda$	$\lambda$	$\lambda$	$\lambda$	$\lambda$	$\lambda$	$\lambda$	$\lambda$
40	3T4R	sin	$\lambda$	$\lambda$	$\lambda$	$\lambda$	$\lambda$	$\lambda$	$\lambda$	$\lambda$	$\lambda$
41	3T4R	cos	$\lambda$	$\lambda$	-0.002	$\lambda$	$\lambda$	$\lambda$	0.001	$\lambda$	$\lambda$
42	4T4R	sin	$\lambda$	$\lambda$	$\lambda$	0.001	$\lambda$	$\lambda$	$\lambda$	$\lambda$	$\lambda$
43	4T4R	cos	$\lambda$	$\lambda$	$\lambda$	$\lambda$	$\lambda$	$\lambda$	$\lambda$	$\lambda$	$\lambda$

Table 5.3:  $b_{nm}$  decomposition coefficients for nonlinear oscillators. Modes  $n$  are ordered by natural frequency. sin/cos indicates the  $\theta$ -coordinate spatial degeneracy. Harmonics  $m$  are numbered from  $m = 1$  for the fundamental frequency. Coefficients with values smaller than .001 are displayed as  $\lambda$ .

$m$	$m$	$b_{nm}$	1	2	3	4	5	6	7	8	9
0	1T0R	sin	-0.849	0.003	$\lambda$	-0.006	$\lambda$	$\lambda$	$\lambda$	$\lambda$	$\lambda$
1	1T0R	cos	-0.060	0.003	$\lambda$	-0.006	$\lambda$	$\lambda$	$\lambda$	$\lambda$	$\lambda$
2	2T0R	sin	$\lambda$	-0.019	-0.002	-0.002	$\lambda$	$\lambda$	$\lambda$	$\lambda$	$\lambda$
3	2T0R	cos	0.001	-0.439	0.002	$\lambda$	$\lambda$	$\lambda$	$\lambda$	$\lambda$	$\lambda$
4	0T1R	-	$\lambda$	-0.003	0.003	$\lambda$	$\lambda$	$\lambda$	$\lambda$	$\lambda$	$\lambda$
5	3T0R	sin	0.015	0.010	0.297	$\lambda$	$\lambda$	$\lambda$	$\lambda$	$\lambda$	$\lambda$
6	3T0R	cos	-0.003	0.004	-0.037	$\lambda$	-0.002	$\lambda$	$\lambda$	$\lambda$	$\lambda$
7	4T0R	sin	-0.001	0.003	-0.002	0.035	$\lambda$	0.002	$\lambda$	$\lambda$	$\lambda$
8	4T0R	cos	0.004	0.013	0.002	0.199	-0.001	$\lambda$	$\lambda$	$\lambda$	$\lambda$
9	1T1R	sin	0.061	$\lambda$	-0.040	-0.002	$\lambda$	$\lambda$	$\lambda$	$\lambda$	$\lambda$
10	1T1R	cos	0.008	-0.002	-0.015	$\lambda$	$\lambda$	$\lambda$	$\lambda$	$\lambda$	$\lambda$
11	2T1R	sin	$\lambda$	0.003	$\lambda$	-0.035	-0.001	$\lambda$	$\lambda$	$\lambda$	$\lambda$
12	2T1R	cos	$\lambda$	0.039	-0.002	-0.040	-0.002	$\lambda$	$\lambda$	$\lambda$	$\lambda$
13	0T2R	-	$\lambda$	-0.009	$\lambda$	-0.008	$\lambda$	$\lambda$	$\lambda$	$\lambda$	$\lambda$
14	3T1R	sin	$\lambda$	$\lambda$	-0.025	0.001	0.033	0.001	$\lambda$	$\lambda$	$\lambda$
15	3T1R	cos	-0.005	$\lambda$	$\lambda$	$\lambda$	-0.057	-0.001	$\lambda$	$\lambda$	$\lambda$
16	1T2R	sin	-0.016	$\lambda$	0.011	$\lambda$	$\lambda$	$\lambda$	$\lambda$	$\lambda$	$\lambda$
17	1T2R	cos	0.002	$\lambda$	-0.007	$\lambda$	-0.005	$\lambda$	$\lambda$	$\lambda$	$\lambda$
18	4T1R	sin	$\lambda$	0.003	$\lambda$	$\lambda$	$\lambda$	0.053	$\lambda$	$\lambda$	$\lambda$
19	4T1R	cos	$\lambda$	$\lambda$	$\lambda$	0.012	$\lambda$	0.025	$\lambda$	$\lambda$	$\lambda$
20	2T2R	sin	$\lambda$	-0.002	$\lambda$	0.012	$\lambda$	$\lambda$	$\lambda$	$\lambda$	$\lambda$
21	2T2R	cos	$\lambda$	-0.009	$\lambda$	0.008	$\lambda$	-0.008	$\lambda$	$\lambda$	$\lambda$
22	0T3R	-	$\lambda$	0.005	$\lambda$	$\lambda$	$\lambda$	-0.001	$\lambda$	$\lambda$	$\lambda$
23	3T2R	sin	-0.001	$\lambda$	0.001	$\lambda$	-0.009	$\lambda$	0.010	$\lambda$	$\lambda$
24	3T2R	cos	$\lambda$	$\lambda$	-0.001	$\lambda$	0.007	$\lambda$	-0.007	$\lambda$	$\lambda$
25	1T3R	sin	0.005	$\lambda$	-0.004	$\lambda$	0.003	$\lambda$	$\lambda$	$\lambda$	$\lambda$
26	1T3R	cos	-0.002	$\lambda$	0.004	$\lambda$	$\lambda$	$\lambda$	$\lambda$	$\lambda$	$\lambda$
27	4T2R	sin	$\lambda$	$\lambda$	$\lambda$	$\lambda$	$\lambda$	0.002	$\lambda$	0.010	$\lambda$
28	4T2R	cos	$\lambda$	$\lambda$	$\lambda$	$\lambda$	$\lambda$	0.016	$\lambda$	0.008	$\lambda$
29	2T3R	sin	$\lambda$	0.001	$\lambda$	-0.003	$\lambda$	0.002	$\lambda$	$\lambda$	$\lambda$
30	2T3R	cos	$\lambda$	0.004	$\lambda$	-0.002	$\lambda$	0.003	$\lambda$	$\lambda$	$\lambda$
31	0T4R	-	$\lambda$	-0.002	$\lambda$	0.001	$\lambda$	$\lambda$	$\lambda$	$\lambda$	$\lambda$
32	3T3R	sin	$\lambda$	$\lambda$	-0.002	$\lambda$	-0.003	$\lambda$	-0.003	$\lambda$	0.002
33	3T3R	cos	$\lambda$	$\lambda$	$\lambda$	$\lambda$	$\lambda$	$\lambda$	$\lambda$	$\lambda$	$\lambda$
34	1T4R	sin	-0.003	$\lambda$	$\lambda$	$\lambda$	-0.001	$\lambda$	$\lambda$	$\lambda$	$\lambda$
35	1T4R	cos	0.001	$\lambda$	-0.001	$\lambda$	$\lambda$	$\lambda$	$\lambda$	$\lambda$	$\lambda$
36	4T3R	sin	$\lambda$	$\lambda$	$\lambda$	$\lambda$	$\lambda$	$\lambda$	$\lambda$	-0.002	$\lambda$
37	4T3R	cos	$\lambda$	$\lambda$	$\lambda$	-0.001	$\lambda$	$\lambda$	$\lambda$	0.005	$\lambda$
38	2T4R	sin	$\lambda$	$\lambda$	$\lambda$	$\lambda$	$\lambda$	$\lambda$	$\lambda$	$\lambda$	$\lambda$
39	2T4R	cos	$\lambda$	-0.003	$\lambda$	$\lambda$	$\lambda$	$\lambda$	$\lambda$	$\lambda$	$\lambda$
40	3T4R	sin	$\lambda$	$\lambda$	0.002	$\lambda$	$\lambda$	$\lambda$	-0.001	$\lambda$	$\lambda$
41	3T4R	cos	$\lambda$	$\lambda$	$\lambda$	$\lambda$	$\lambda$	$\lambda$	$\lambda$	$\lambda$	$\lambda$
42	4T4R	sin	$\lambda$	$\lambda$	$\lambda$	$\lambda$	$\lambda$	$\lambda$	$\lambda$	$\lambda$	$\lambda$
43	4T4R	cos	$\lambda$	$\lambda$	$\lambda$	0.001	$\lambda$	$\lambda$	$\lambda$	$\lambda$	$\lambda$

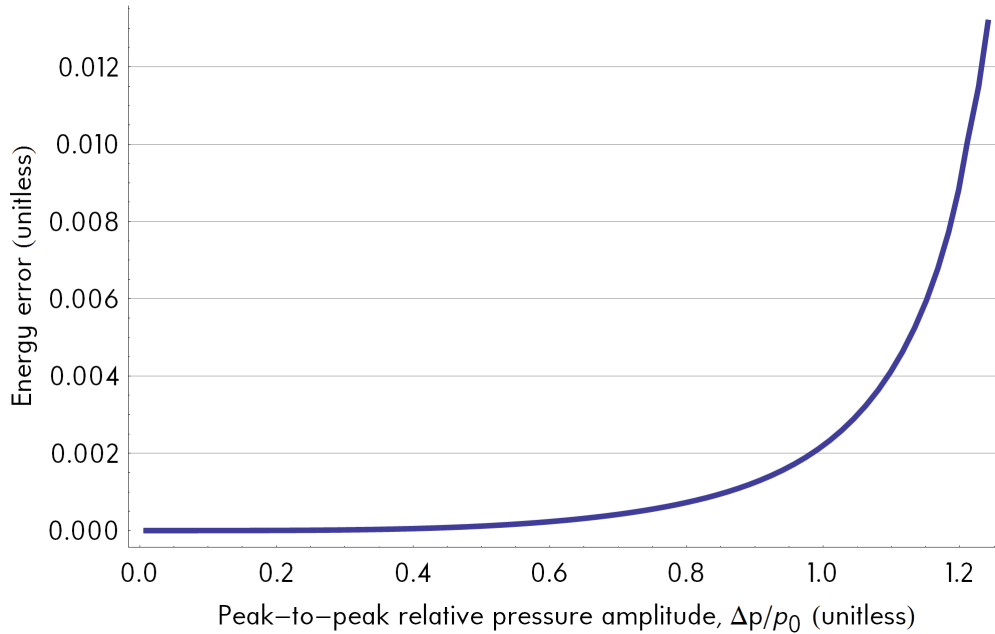


Figure 5.4: Plot of error energy versus relative peak-to-peak pressure amplitude for oscillator simulations

Tables 5.2 and 5.3 show that the assumption was not met exactly. In any given row or column, one coefficient is an order of magnitude larger than nearly all the other coefficients. However, there are modes (2T1R, for instance, row 11 in Table 5.2) that have more than one harmonic ringing at the same order of magnitude. Also, some harmonics (e.g.  $m = 3$ , column 3 of Table 5.2) have distinct contributions from more than one mode shape. This indicates both shifted mode shapes (as in Chapter 4) and non-sinusoidal excitation of individual modes.

To quantify the change in the solution with and without the assumption, the coefficients were examined with an energy-error method as described in Chapter 1. This energy error addressed a different question from the RMS experiment error. The RMS experiment error addressed the issue of whether the solutions agreed with physical evidence. This energy error addressed the question of whether the theory agrees with the mode/frequency assumption.

Figure 5.4 shows this error varying with the forcing parameter  $F$ . The maximum error shown, 1.2%, indicates that the energy stored in nondominant modes in the nonlinear oscillator solutions is two orders of magnitude smaller than the total unsteady energy. That is to say, though the assumption is not met exactly, the error associated with the assumption is  $< 2\%$  for amplitudes up to  $1.2p_0$ .

Note, however, the presence of an exponential trend in Figure 5.4. This approach cannot predict the error of higher-amplitude waves, but if this trend continues, the error associated with the mode/frequency assumption will reach unacceptable levels at  $2p_0$ .



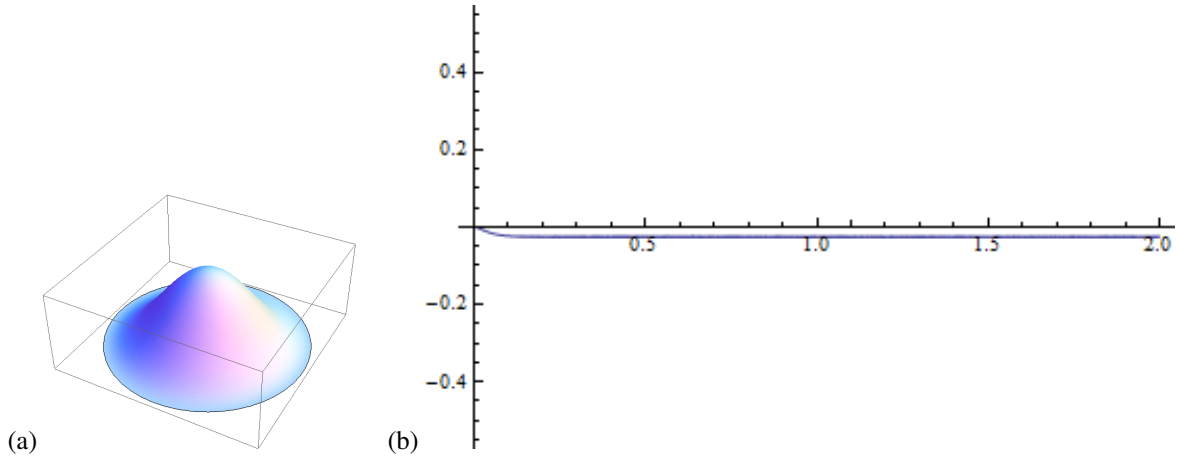


Figure 5.5: 1R component of oscillator simulation: (a) mode shape, (b)  $\eta_{1R}(t)$  versus time (sec)

## 5.6 DC Valley

At first, the solutions decomposed into  $a_{nm}$ ,  $b_{nm}$  and then recomposed into waveforms were different from the solutions plotted directly from the numerically evaluated  $\eta_n$  functions.

This was traced to missing zero-frequency (time-independent) components, primarily in the 0T1R mode (also called the “1R” mode). Figure 5.5 shows the 1R mode shape and a time-history of the numerically solved  $\eta_{1R}(t)$  function.  $\eta_{1R}(t)$  shifted from zero to a negative value, with little or no oscillation. This negative value, multiplied by the 1R mode, gives a valley shape, with lowered mean pressure at the center and raised mean pressure at the rim.

This DC valley offset is discussed further in Chapter 7.

## 5.7 Summary

Models of the form of nonlinearly coupled harmonic oscillators were sought. A previously derived oscillator model was numerically solved under damped, driven conditions appropriate to drive a 1T spinning mode. The model was found to be numerically unstable above limit cycle peak-to-peak relative amplitudes of 1.2 times the mean pressure.

The solutions were validated against experiment. Visual comparison showed the characteristic “U” shape waveform matching the experimental waveforms, and RMS error comparisons revealed 7% error or less for all test cases. The solutions were decomposed into mode/harmonic coefficients, and the coefficients showed the mode/frequency assumption to be valid to amplitudes of  $1.2p_0$ , peak-to-peak.

The DC valley observed in Maslen and Moore’s solution also appeared in the oscillator solution. It contributed in a similar way to the waveform shape.

Overall, the conclusions of Chapter 4 were confirmed using a different theory that made different assumptions, providing reinforcement of two conclusions:

- The mode/frequency assumption is a valid to amplitudes of at least  $1.2p_0$  peak-to-peak (with no data for higher amplitudes).
- Steepened 1T cylindrical waves induce a time-independent, radially distributed DC shift in pressure (and other flow variables).

# Chapter 6

## Theory 4: CFD

Computational fluid dynamics (CFD) is employed by researchers and engineers to obtain solutions to the fluid dynamic equations. CFD was used to provide additional evidence concerning the question of shifted mode shapes (the mode/frequency assumption).

### 6.1 Theory

To obtain a CFD solution for the mode problem of Chapter 2, it was necessary to state appropriate equations governing the solution, and select a suitable numerical scheme to solve the governing equations.

#### 6.1.1 Governing Equations

The exact form of the governing equations selected depends on the numerical scheme used to solve them. A finite volume approach was employed, which used the fluid dynamic equations in integral form:

$$\begin{aligned} \frac{d}{dt} \int_V \rho dV + \int_{\partial V} \rho(\vec{u} \cdot d\vec{A}) &= 0 && \text{Conservation of Mass} \\ \frac{d}{dt} \int_V \vec{u} \rho dV + \int_{\partial V} \rho \vec{u}(\vec{u} \cdot d\vec{A}) &= \sum_k F_k && \text{Conservation of Momentum} \\ \frac{d}{dt} \int_V \rho e dV + \int_{\partial V} \rho e(\vec{u} \cdot d\vec{A}) &= \sum_k \Gamma_k && \text{Conservation of Energy} \end{aligned} \tag{6.1}$$

In the above equations,  $F_k$  are various forces acting on the fluid, and  $\Gamma_k$  are various sources/sinks of internal energy (such as heat transfer). The only force considered in the solver was pressure, and no sources or sinks of energy were considered.

#### 6.1.2 Numerical Approach

The heart of CFD schemes is transforming integral or differential equations governing a continuous domain into algebraic equations governing a discrete domain.

The CFD scheme chosen was as follows, with justifications listed for each decision.

- Finite volume. Finite volume solvers use the volume form of the fluid dynamic equations. For the inviscid equations and first order schemes, this eliminates the need to calculate all derivatives except the time derivative.
- Unstructured mesh. This comes down to a preference. No one structured mesh would work equally well for all problems under consideration, and generating highly refined unstructured meshes is easier than generating custom structured meshes. However, unstructured meshes have higher dissipation than structured meshes.
- Roe flux scheme. While originally an AUSM+ scheme was used [49], the Roe flux scheme is trusted by CFD veterans as having lower dissipation and giving higher quality solutions. [50]

Some might question the choice of a traditional CFD solver over a computational aeroacoustics (CAA) method. The problems under consideration are essentially pressure waves, and CAA was developed extensively to deal with specific issues encountered in the calculation of fluid dynamic waves. These include [51]:

- wide frequency ranges;
- small amplitudes;
- radiation to far field;
- radiation boundary conditions;
- multiple scales.

However, of these concerns, only the first and last apply to the problem of finite amplitude waves in closed cavities. The waves under consideration are of the same order of magnitude as the mean variables, which is different from CAA problems where pressure variations are five or six orders of magnitude smaller. Internal flow with rigid wall boundaries means radiation out of the system should not happen, exactly the opposite of a typical aeroacoustics problem.

The remaining two concerns (wide frequency ranges and multiple scales), as well as the known difficulties with using first order schemes and unstructured meshes (dissipation), are addressed in this case by increasing the computational cell density. Remembering that the order accuracy of a scheme (first order, fourth order, etc.) is not the same as the accuracy of a solution; solutions capturing wide ranges of frequencies and wavelengths can be achieved for this problem of strong waves by using small time steps and tightly spaced grid points.

## 6.2 Procedure

### 6.2.1 Solver Development

A new custom finite-volume solver was developed in phases as experience was gained and capabilities added. The original motivation for the solver was unpublished work by Jacob [47], using a one dimensional AUSM+ solver to simulate the longitudinal steepening problem.

The AUSM family has many strong advantages, especially programmatic simplicity and low computational cost. [49] However, for this relatively simple 2D problem, its disadvantages (primarily numerical dissipation) seemed larger. The Riemann solver of Roe [50] is believed to be one of the lowest dissipation flux schemes available to finite volume

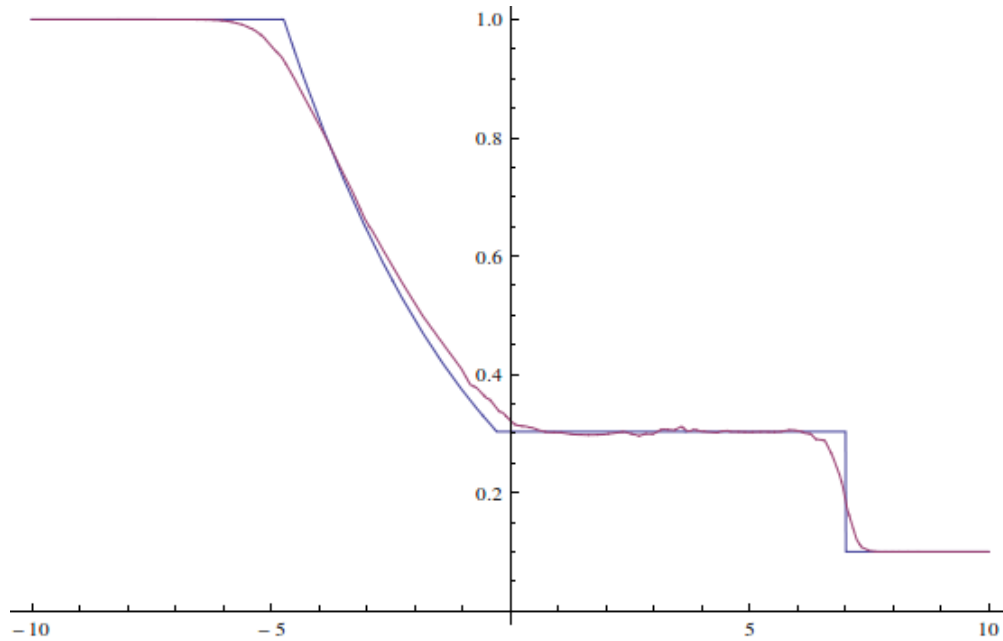


Figure 6.1: Sod shock problem verification: nondimensional pressure

solvers. Though the Roe scheme requires eigenvalues and eigenvectors of the Riemann problem, with many thanks to Dr. Masatsuka for his freely available well-documented codes [52], a Roe scheme from those codes was adapted and incorporated in the new solver.

The new solver was verified using a standard test problem: the Sod shock tube. The Sod shock tube problem is a one dimensional problem with three initial conditions: zero velocity throughout the domain (fluid initially at rest), dimensionless pressure of 1 in the left half of the domain with 0.1 in the right half of the domain, and initial dimensionless densities of 1 in the left half and 0.1 in the right half. From this initial discontinuity, a shock propagates to the right and an expansion fan propagates to the left.

In order to verify the 2D solver, the Sod shock tube problem was simulated on a square mesh, with the wave propagation along the  $y = x$  line (i.e., rotated 45 degrees from purely  $x$  or purely  $y$ ). Figures 6.1 and 6.2 show that the solver exhibits all the expected waves (fast expansion left, contact discontinuity right, fast shock right), with some dispersion of the shocks relative to the analytic solution. Remembering that this is a first order scheme on an unstructured 2-D mesh, this dispersion is within the expected range. Figures 6.3, 6.4, and 6.5 show how the solution was oriented on a diagonal 2-D mesh.

## 6.2.2 Test Case Development

In following Jacob [47], the original goal of the CFD work was to give the solver initial conditions for an acoustic mode at very high amplitude, then permit the solver to steepen the wave. Initial results were promising, and with mesh refinement the solution appears to have little dissipation in the first dozen wavelengths, while fully steepening in the

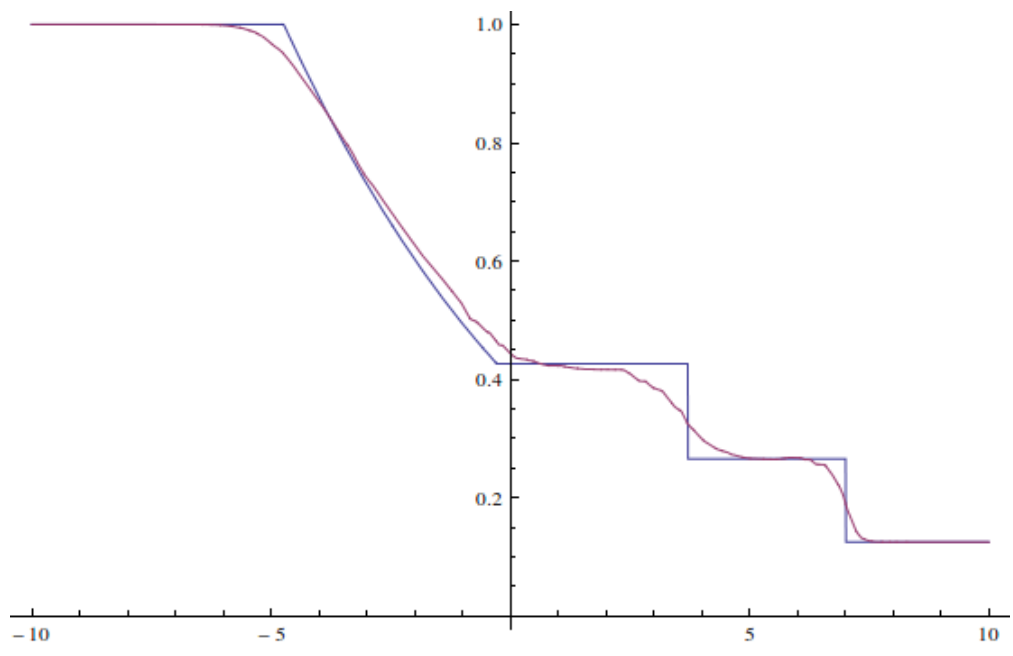


Figure 6.2: Sod shock problem verification: nondimensional density

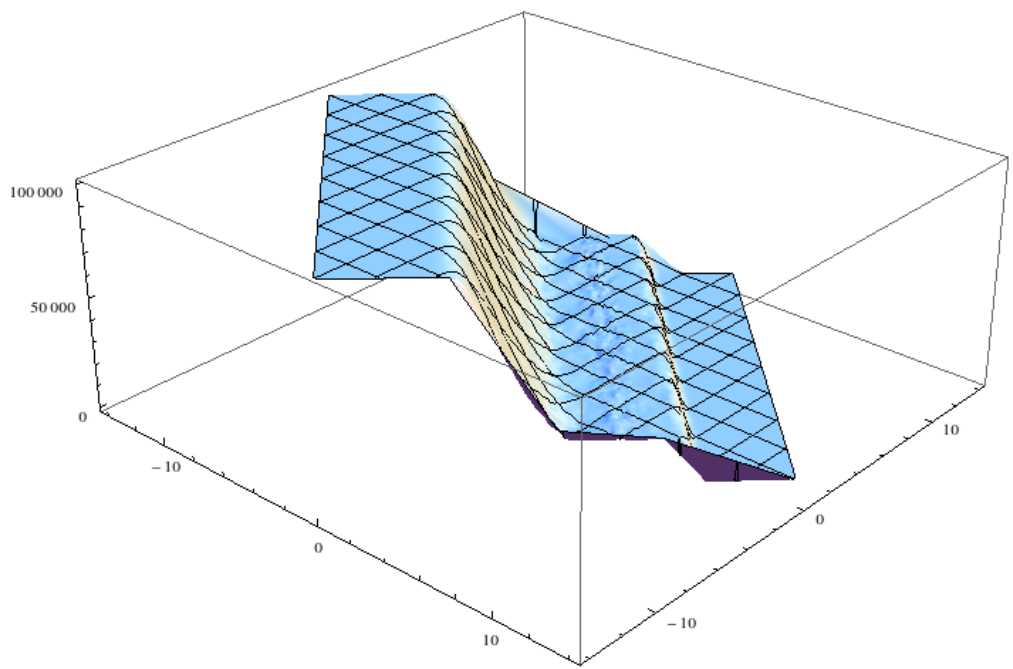


Figure 6.3: Sod shock problem: nondimensional pressure surface

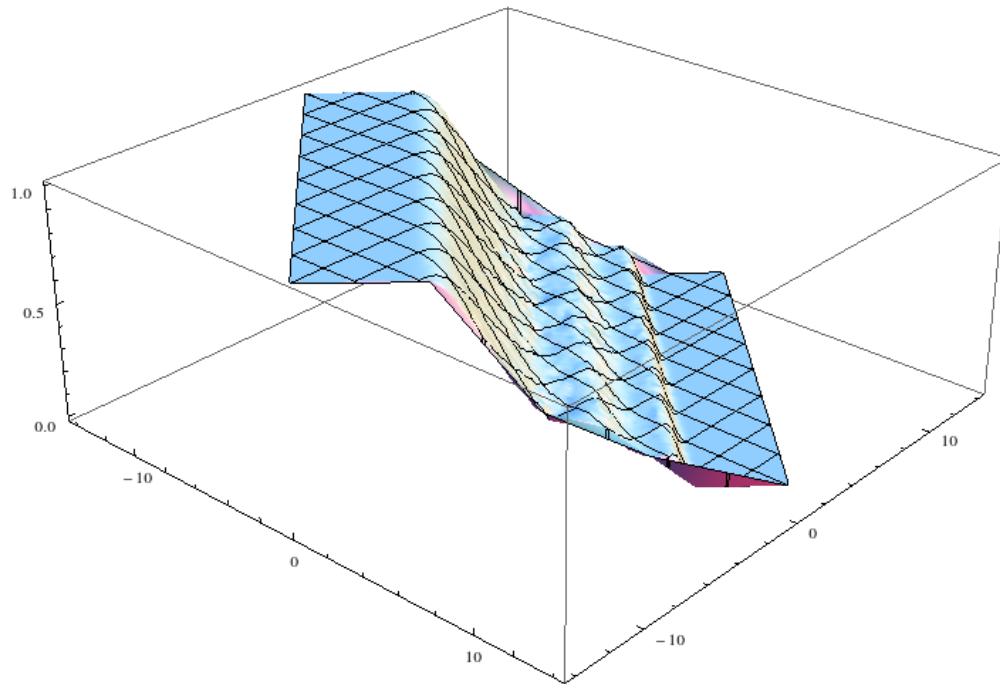


Figure 6.4: Sod shock problem: nondimensional density surface

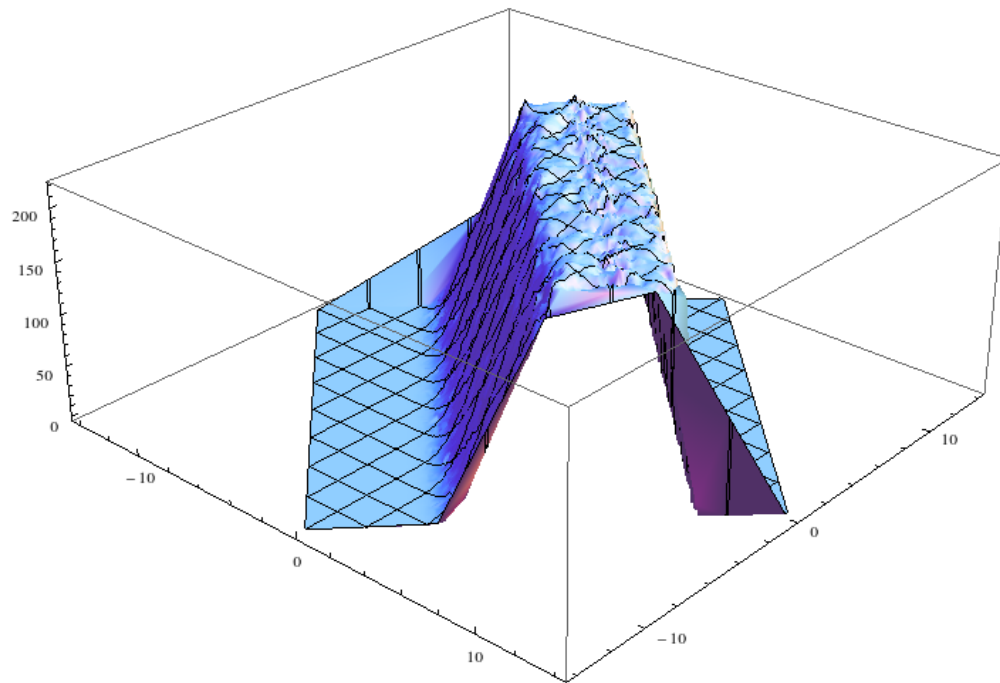


Figure 6.5: Sod shock problem: nondimensional x-velocity surface

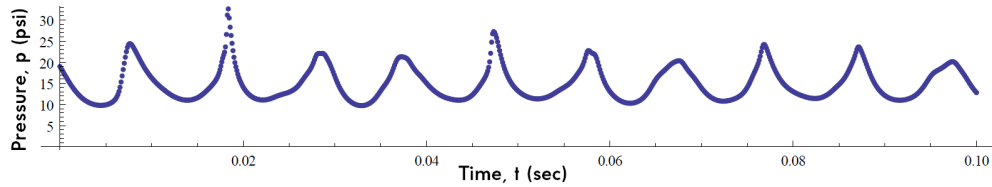


Figure 6.6: Example CFD trace showing pressure at one point on the edge, throughout the simulation

first two wavelengths.

It was suggested that modeling the wave as driven and damped might give better results. In the CFD solver, driving would require careful selection of oscillatory boundary conditions matched to the model problem. Damping would require adding viscous and heat transfer effects (in turn requiring the addition of gradient estimation methods).

From the primary models of Chapters 3, 4 and 5, it was unclear whether an isentropic steepening or damped/driven steepening would be more appropriate. The solution of Maslen and Moore was isentropic, yet seemed to capture the steepening reasonably well. Both other methods, however, were numerically unstable without damping/driving.

Several different approaches were tried to find boundary conditions suitable to driving. While partially successful, the amplitudes achievable with these driving boundary conditions were too small to be useful for considering the steepening problem. Only one of the five test cases fell within the range of amplitudes that were successfully achieved with steepening.

As the primary difficulty seemed to be the appearance of negative densities, range limiters were added to the solver to enforce density to be strictly positive. Though this permitted solutions to run longer, it did not solve the problem, as eventually the fluxes were calculated to be above machine precision, and NaN (not-a-number) values appeared in the solution.

Thus, the isentropic steepening approach was applied: begin with initial conditions corresponding to an acoustic mode at very high amplitudes, start the solver, and stop the solver once the solution achieved a limit cycle waveform. This turned out to be approximately 10 wave cycles for the mesh used on test cases.

### 6.2.3 Mesh Refinement

To ensure the solution was independent of a particular mesh, the mesh was refined multiple times and compared against the finest mesh used. The model simulation was a spinning wave initial condition, run through 10 wavelength cycles. A single point in space was studied over time (Figure 6.6 shows an example), and the entire spatial solution was studied at the final time of the simulation (see Figure 6.7).

Figures 6.8 and 6.9 are closely related, in that they show the observed convergence of the solution with mesh refinement. Both compare each solution in the series to the solution with the smallest grid spacing, using an RMS



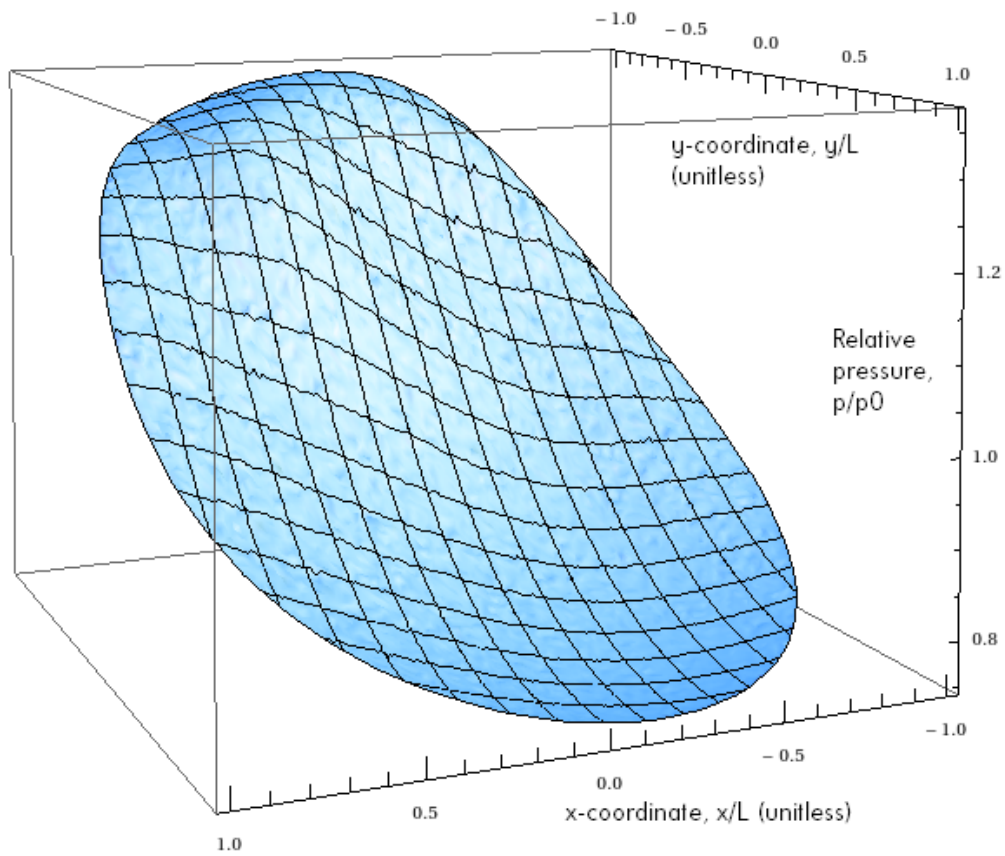


Figure 6.7: Example CFD mode shape showing pressure at every point in space, at one point in time

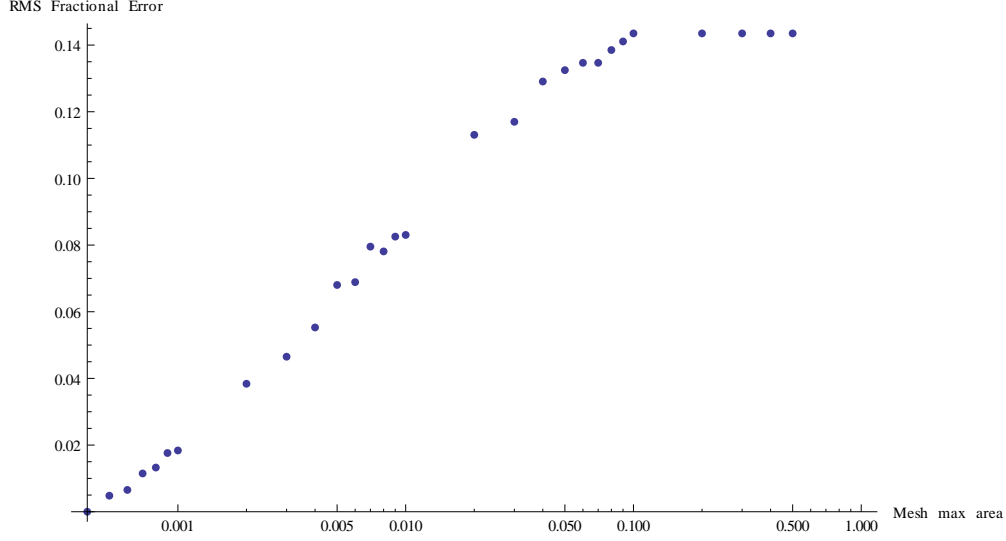


Figure 6.8: Mesh independence of final spatial pressure distribution

error:

$$\text{RMS convergence error of solution } k \text{ to final solution } f = \sqrt{\frac{1}{N} \sum_n \left( \frac{p_{k,n} - p_{f,n}}{p_{f,n}} \right)^2} \quad (6.2)$$

where  $N$  is the number of points considered. Figure 6.8 uses the final spatial distribution as the points under consideration. The RMS error is between the pressure surfaces at final time for each solution, showing that each mesh refinement got closer to the same final pressure distribution. Figure 6.9 uses the times of an individual point in space as the points under consideration. The RMS error represents the difference between different time histories, showing converging of the time-dependent solution.

Over the range studied, mesh refinement always caused declining RMS error. Machine precision error was not reached in the studied case. In applying CFD to the model problem, a mesh of 5,000 points was used, corresponding to average spatial separation of 0.03 (nondimensional, corresponds to 3% of the chamber radius).

## 6.2.4 Initial Conditions vs. Amplitude

Simulations for the model problem of Chapter 2 were run with varying values of the initial acoustic mode amplitude. The initial conditions are determined by multiplying an initial amplitude factor  $A_0$  by the 1T spinning mode solution at time  $t = 0$ :

$$\psi_{1T}(r, \theta, t) = A_0 J_1(\lambda_{1T} r / R) \cos(\theta + \omega_{1T} t) \quad (6.3)$$

This initial amplitude factor  $A_0$  is not the same as peak-to-peak wave amplitude (nor even peak-to-mean wave amplitude), as it would be for a sine or cosine mode. Unlike sine and cosine, Bessel functions do not rise/fall in equal measure. Nevertheless,  $A_0$  is the dimensionless amplitude of the mode.

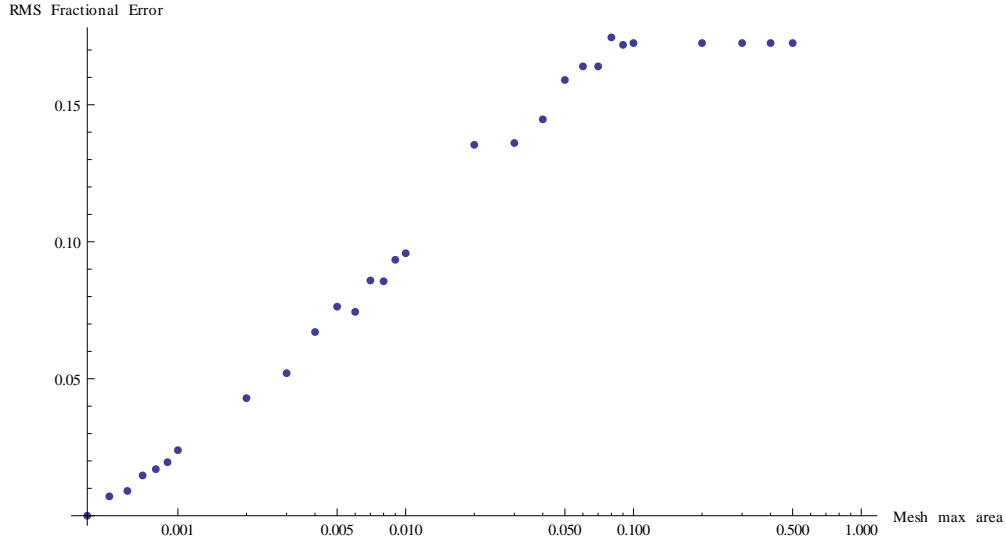


Figure 6.9: Mesh independence of pressure-time solution at the wall.

When this velocity potential  $\psi_{1T}$  is transformed into velocity, pressure and density distributions, the resulting initial conditions show the pressure distribution and velocity distribution 90 degrees out of phase with each other, as shown in Figure 6.10.

As the initial amplitude  $A_0$  was increased, the solutions became unstable at  $A_0 = 0.8$  and the solver was unable to complete the simulation. As Figure 6.11 shows, the pressure did not approach zero at these amplitudes. Some other limitation of the solver, possibly maximum precision, limited the range of achievable amplitudes. Figure 6.12 shows the range of achieved peak-to-peak amplitudes and their corresponding initial wave amplitudes. The maximum realized peak-to-peak amplitude was approximately  $0.9p_0$ , excluding two of the experimental test cases.

### 6.3 Experimental Validation

Note that the maximum attained peak-to-peak amplitude with the CFD solver was  $0.9p_0$ , which excludes two of the test cases.

The theory was validated against experiment in two ways. First, for each test case, the experimental data and the solution with matching peak-to-peak amplitude were plotted together, as shown in Figure 6.13. The characteristic steepening shape—the shift from sinusoidal to a “U” shape—is apparent in both the CFD simulations and the experiment. The third test case showed the theory deviating at the peaks from the symmetric “U” shape, though still capturing the sharper peaks and shallower troughs. This deviation may be due to numerical instabilities appearing in the solution, enough to alter the solution but not enough to cause the solver to crash.

Second, an error was calculated between the predicted and observed waveforms. The error was taken as the root-mean-square of the fractional error of each pressure measurement  $i$  of the  $M$  test points available for a given test

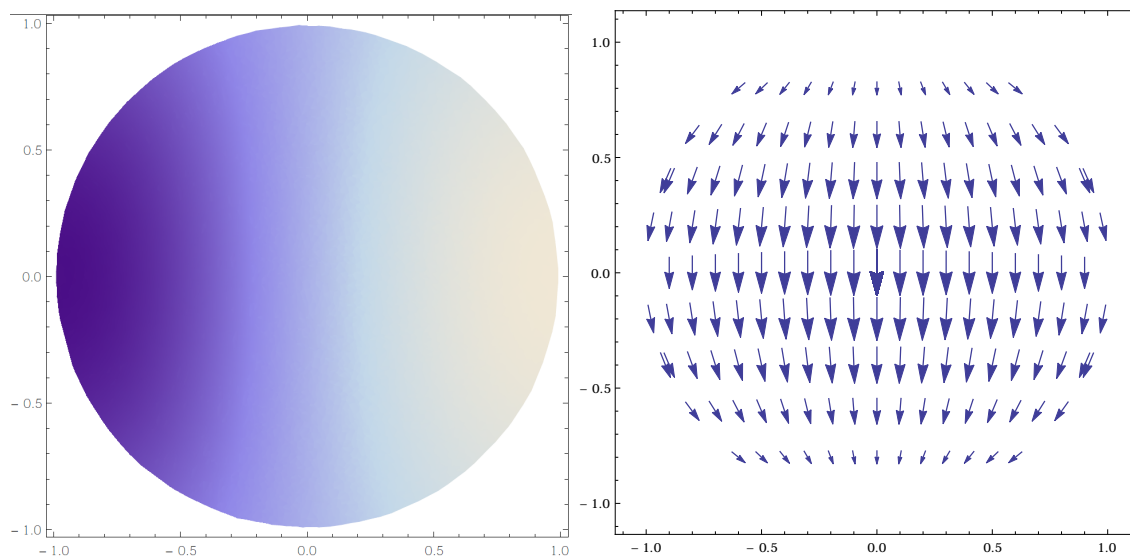


Figure 6.10: Diagram of CFD initial conditions, showing the pressure distribution (left) and the velocity distribution (right).

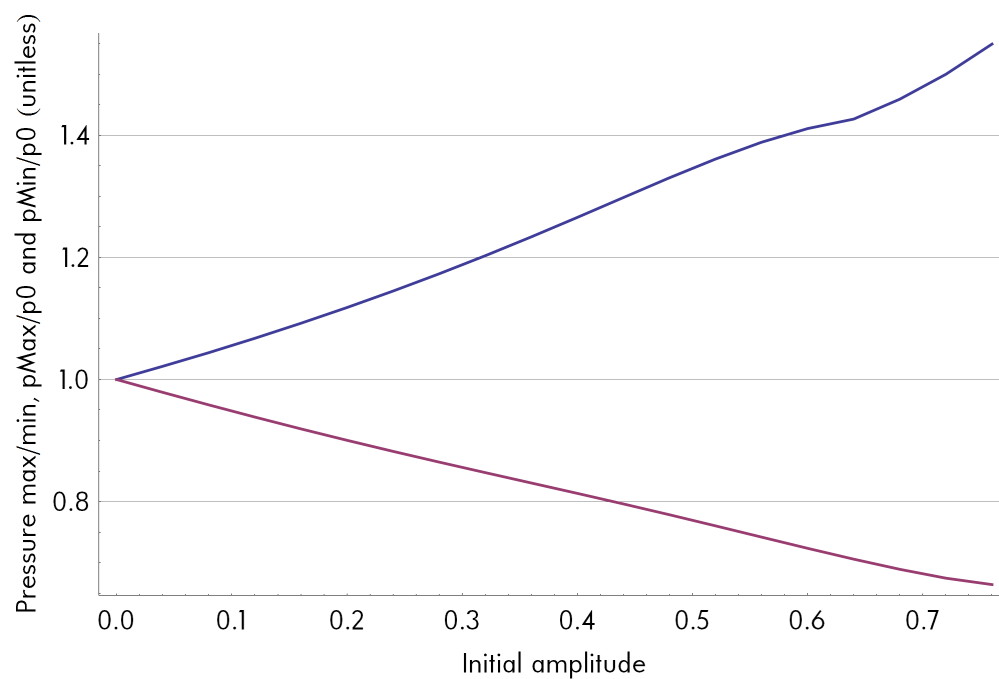


Figure 6.11: Minimum and maximum relative pressures ( $\frac{p_{max}}{p_0}, \frac{p_{min}}{p_0}$ ) of CFD 1T spinning wave solution

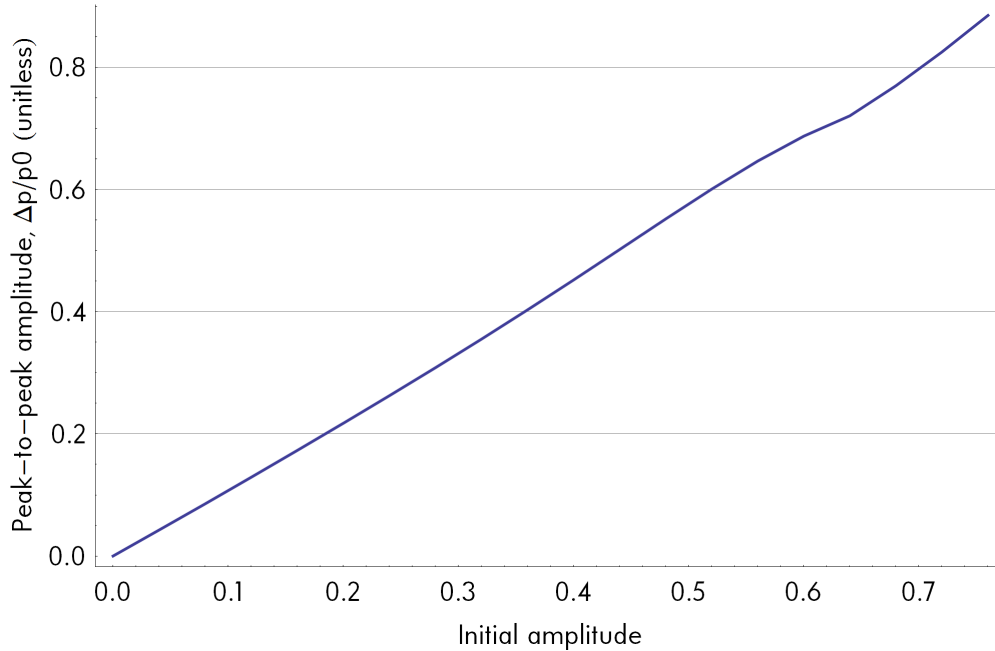


Figure 6.12: Peak-to-peak amplitudes ( $\frac{p_{max}-p_{min}}{p_0}$ ) of CFD 1T spinning wave solution.

case:

$$\text{RMS error} = \sqrt{\frac{1}{M} \sum_i \left( \frac{p_{i,experiment} - p_{i,theory}}{p_{i,experiment}} \right)^2} \quad (6.4)$$

Note that this RMS error is different from that of Section 6.2.3. This RMS experiment error measured the difference between a particular solution and the experimental evidence. The RMS error of Section 6.2.3 measured the difference between two solutions to the same problem with different meshes.

Table 6.1 shows this RMS error for each test point. The first two cases show an error of < 5%, while the error grew for the higher amplitude case to 11.1%. Though this error does not indicate excellent agreement, it indicates that the solution is capturing at least some of the relevant physics.

## 6.4 Mode/Harmonic Decomposition

### 6.4.1 Procedure

The final limit cycle solutions were decomposed numerically into linear-mode/harmonic coefficients, as described in Chapter 1. As the CFD solution consisted of the values of fluid variables at discrete mesh points, no analytical techniques could be performed to simplify the computation of the integrals. Mathematica 9 was used to interpolate the CFD solution and compute the decomposition integrals of Chapter 1 numerically.

The decomposition was in some ways at least as challenging as obtaining a reasonable solution. Consider decom-

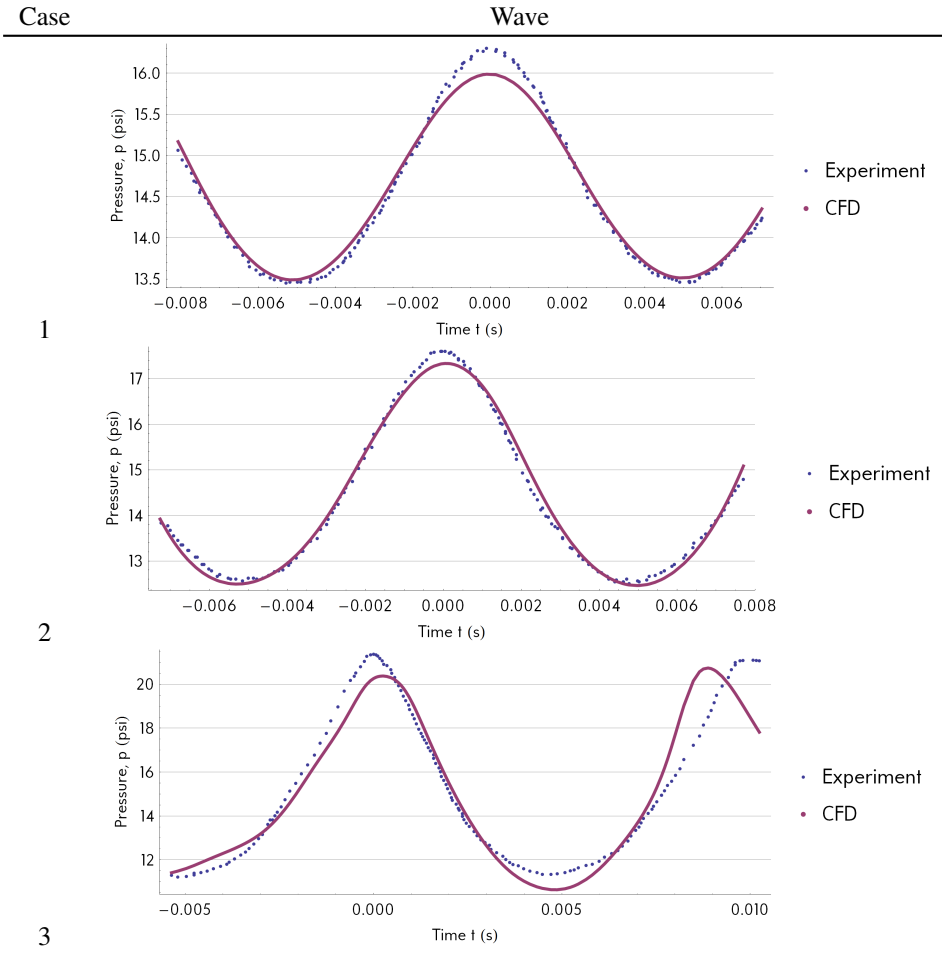


Figure 6.13: Pressure-time comparison of CFD prediction (in red) to Heidmann experiment (in blue). See Table 2.2 for information on cases.

Table 6.1: RMS error comparison of CFD prediction to experiment

Case	Peak-to-peak (dimensionless) $\Delta p$	RMS err $\frac{\Delta p}{p_0}$	
1	2.8 psi	0.19	4.5%
2	5.5 psi	0.37	3.8%
3	10.0 psi	0.67	11.1%
4	15.5 psi	1.01	Unknown
5	24.0 psi	1.52	Unknown

posing one solution into  $N$  modes with  $M$  harmonics, given data over  $T$  seconds at time slices every  $dt$  seconds. One decomposition requires  $M * (T/dt)$  two-dimensional spatial integrals to resolve the time functions of each mode, and  $M * N$  temporal integrals to resolve the harmonic coefficients from the time functions. For  $M = 44$ ,  $N = 20$ , and  $T/dt = 200$ , this comes to 8800 two-dimensional integrals and 880 one dimensional integrals.

Several different numerical integration techniques were explored. Mathematica's QuasiMonteCarlo method was found to provide the most accurate results in reasonable times. (The accuracy of a decomposition was determined by comparing the decomposed/reconstructed solution to the original solution.) However, ultimately it proved much less costly to estimate the spatial integrals by using a technique similar to Discrete Fourier Transforms, except applied to the acoustic mode shapes.

To evaluate the spatial integrals:

$$\eta_n(t) = \frac{\int_V p(\vec{r}, t) \psi_n(\vec{r}) dV}{\int_V \psi_n^2 dV} \quad (6.5)$$

The integrals were replaced by sums over the mesh points  $k$ :

$$\eta_n(t) \approx \frac{\sum_k p(\vec{r}_k, t) \psi_n(\vec{r}_k) dV_k}{\sum_k \psi_n(\vec{r}_k)^2 dV_k} \quad (6.6)$$

By approximating  $dV_k$  as a constant, it factors out of the numerator and denominator sums, then cancels, leaving the equation:

$$\eta_n(t) \approx \frac{1}{C_n} \sum_k p(\vec{r}_k, t) \psi_n(\vec{r}_k) \quad (6.7)$$

$$C_n = \sum_k \psi_n(\vec{r}_k)^2 \quad (6.8)$$

The procedure was as follows:

- Pre-calculate the value of each acoustic mode at each of the mesh points:  $\psi_n(\vec{r}_k)$
- Pre-calculate the normalizing coefficients  $C_n$ .
- For each mode and each time step, compute the sum in Equation 6.7

Unlike the other theories, the numeric integrals for the higher modes introduced errors into the solution. The decomposed/recomposed solution actually got worse when higher modes were included in the decomposition. This indicated that one of the limitations of CFD—the ability to resolve spatial variations on the scale of the mesh—was influencing the decomposition. Higher modes have many more nodes and antinodes, requiring meshes with much smaller grid spacing than was employed.

This limited the analysis to ten modes, though those ten modes were enough to capture the majority of the wave: < 2% RMS error across the solution domain. That is to say, an RMS fractional solution error across the mesh points comparing the CFD solution and the decomposed/recomposed solution was < 2% when only ten modes were included in the decomposition.

Tables 6.2 and 6.3 show an example set of decomposition coefficients for one CFD simulation.

Table 6.2:  $a_{nm}$  decomposition coefficients for CFD. Modes  $n$  are ordered by natural frequency. sin/cos indicates the  $\theta$ -coordinate spatial degeneracy. Harmonics  $m$  are numbered from  $m = 1$  for the fundamental frequency. Coefficients with values smaller than .001 are displayed as  $\lambda$ .

$m$			$m$	1	2	3	4	5	6	7	8	9
$a_{nm}$												
0	1T0R	sin	0	-0.007	0.002	$\lambda$	-0.001	-0.002	$\lambda$	$\lambda$	$\lambda$	
1	1T0R	cos	0	-0.607	-0.013	$\lambda$	-0.004	-0.005	-0.003	-0.003	-0.002	
2	2T0R	sin	0	-0.277	0.010	0.005	-0.004	-0.006	-0.003	-0.002	-0.002	
3	2T0R	cos	0	-0.084	-0.023	0.029	0.012	0.006	0.006	0.005	0.004	
4	0T1R	-	0	-0.086	-0.062	0.031	0.015	0.008	0.007	0.006	0.005	
5	3T0R	sin	0	0.007	0.018	$\lambda$	0.003	0.004	0.002	0.002	0.002	
6	3T0R	cos	0	-0.027	0.021	-0.002	-0.012	-0.013	-0.007	-0.006	-0.006	
7	1T1R	sin	0	-0.044	-0.022	0.023	0.025	0.012	0.010	0.008	0.007	
8	1T1R	cos	0	0.028	-0.013	-0.025	0.006	0.006	0.003	0.003	0.002	
9	2T1R	sin	0	0.034	-0.008	0.002	0.003	0.005	0.003	0.003	0.002	

Table 6.3:  $b_{nm}$  decomposition coefficients for CFD. Modes  $n$  are ordered by natural frequency. sin/cos indicates the  $\theta$ -coordinate spatial degeneracy. Harmonics  $m$  are numbered from  $m = 1$  for the fundamental frequency. Coefficients with values smaller than .001 are displayed as  $\lambda$ .

$m$			$m$	1	2	3	4	5	6	7	8	9
$b_{nm}$												
0	1T0R	sin	0.003	-0.001	-0.003	$\lambda$	$\lambda$	$\lambda$	$\lambda$	$\lambda$	$\lambda$	$\lambda$
1	1T0R	cos	0.011	-0.342	-0.013	$\lambda$	0.002	-0.001	-0.002	$\lambda$	$\lambda$	$\lambda$
2	2T0R	sin	-0.048	0.551	-0.007	-0.002	0.002	-0.002	-0.003	-0.001	-0.001	
3	2T0R	cos	-0.072	-0.132	-0.092	0.022	0.014	0.004	0.001	0.002	0.001	
4	0T1R	-	-0.005	0.047	0.056	-0.005	-0.004	-0.005	-0.005	-0.003	-0.002	
5	3T0R	sin	-0.073	0.006	-0.011	-0.002	-0.002	$\lambda$	0.001	$\lambda$	$\lambda$	
6	3T0R	cos	-0.048	-0.084	-0.087	0.014	0.023	0.007	$\lambda$	0.002	0.001	
7	1T1R	sin	-0.020	0.016	-0.005	0.006	0.002	-0.002	-0.003	-0.001	-0.001	
8	1T1R	cos	0.017	0.027	0.006	0.019	$\lambda$	$\lambda$	0.002	$\lambda$	$\lambda$	
9	2T1R	sin	-0.007	-0.002	0.008	0.038	$\lambda$	0.003	0.004	0.002	0.002	



## 6.4.2 Assumption Examined

The second of the two primary questions posed at the start of the work concerned the quality of an assumption:

How much error is created by the mode/frequency assumption of equation 1.32?

To restate the mode/frequency assumption: the total nonlinear wave solution can be described as a superposition of linear acoustic modes, each ringing at a single frequency. As described in Chapter 1, the mode/harmonic coefficients determined from the CFD solution were used to address this question.

Tables 6.2 and 6.3 show that the assumption was not met exactly, though it was met approximately. The majority of coefficients are weak but some harmonics (columns) have more than one nontrivial coefficient, and some modes (rows) have more than one coefficient. This indicates a small deviation from the linear/acoustic mode assumption (each column would have only one nonzero coefficient) and from the single-frequency-per-mode assumption (each row would only have one nonzero coefficient).

To quantify the change in the solution with and without the assumption, the coefficients were examined with an energy-error method as described in Chapter 1. This energy error addressed a different question from either the RMS mesh error or the RMS experiment error. The RMS experiment error addressed the issue of whether the solutions agreed with physical evidence. The RMS mesh error addressed the difference of the solution under different mesh conditions. This energy error addressed the question of whether the theory agrees with the mode/frequency assumption.

Figure 6.14 shows this error varying with the forcing parameter  $F$ . The maximum error shown, approximately 4%, indicates that at an amplitudes of  $.9p_0$  peak-to-peak, the mode/frequency assumption misses only 4% of the system energy.

## 6.5 DC Valley

As in both the perturbation theory of Chapter 4 and the oscillator theory of Chapter 5, the CFD solution exhibited significant zero-frequency (time-independent) components. Figure 6.15 shows the effect of these time-independent components on the overall solution.

The shape of the steady component was observed to be visually different from that of the other theories. The CFD steady component had a saddle shape, rather than the radially symmetric valley shape of the other approaches. Nevertheless, it had a similar effect on the overall wave shape: flattening down a hump in the center of the wave, making the lower part of the wave flatter and the rising part of the wave steeper.

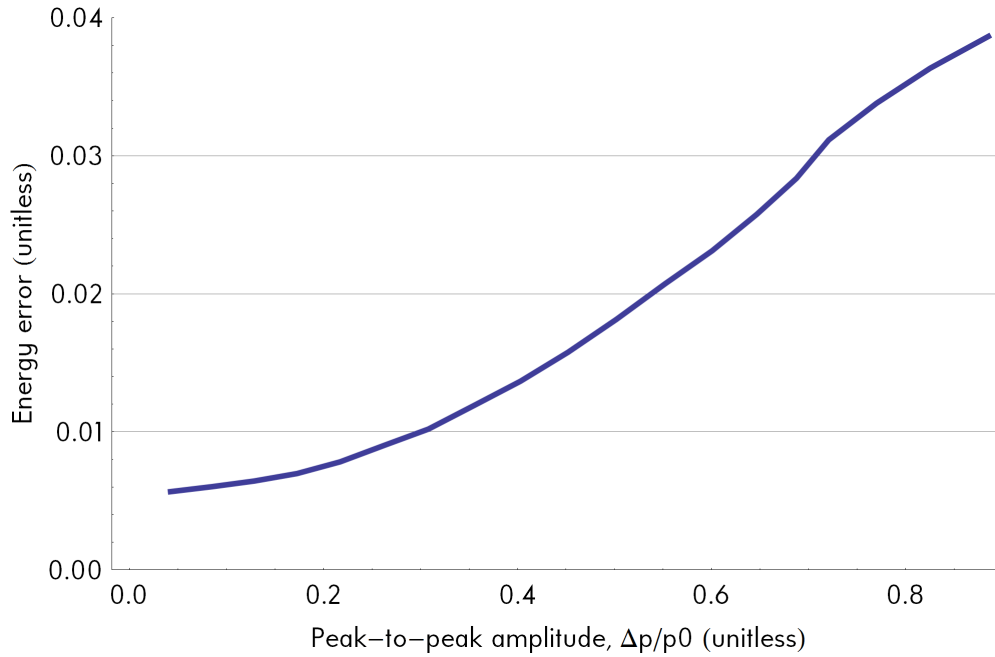


Figure 6.14: Plot of energy in nondominant mode/harmonic combinations

## 6.6 Summary

CFD solutions for the model problem were sought using a custom unstructured, finite volume solver. Initial conditions for a strong cylindrical mode were observed to steepen to shapes similar to other solutions.

The CFD solution had weaker experimental validation than the other two theories (11% error for case 3 with CFD, versus < 4% for the other theories). Even so, the CFD solution provided further evidence for the two primary conclusions of Chapters 4 and 5:

- The mode/frequency assumption is a reasonable assumption to amplitudes of  $1.2p_0$  peak-to-peak, or higher.
- Steepened 1T cylindrical waves induce a time-independent, radially distributed DC shift in pressure (and other flow variables).

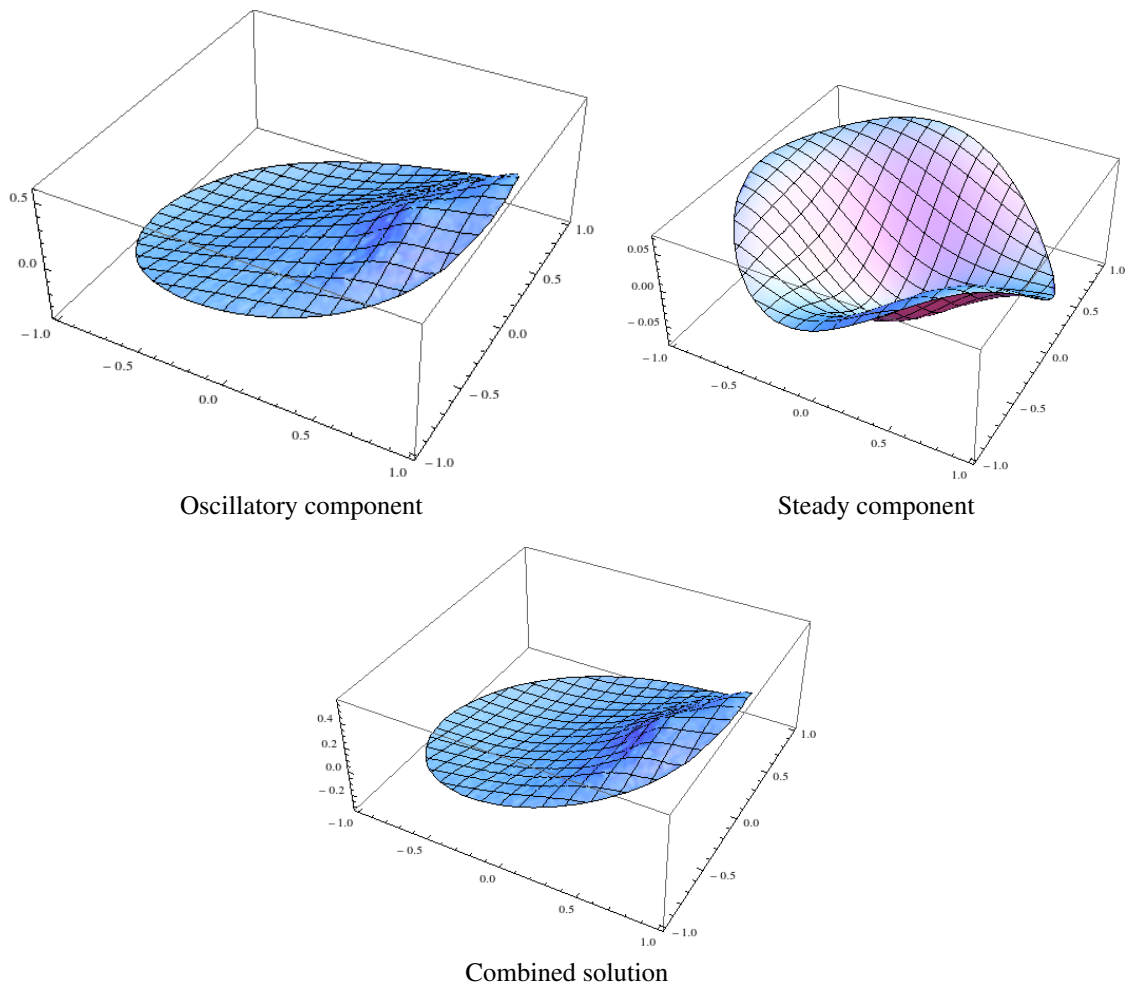


Figure 6.15: DC valley in CFD results. Surface height indicates pressure value (nondimensional:  $p/p_0$ ).

# Chapter 7

## Conclusions

The mode/harmonic assumption simplifies both linear and nonlinear combustion instability analysis and prediction. If justified, it reduces the time and cost of instability predictions and analysis, which in turn reduces the cost and uncertainty of new engine development. Yet cylindrical waves—the simplest non-axial waves—call this assumption into question.

The most common cylindrical wave instability—the 1T spinning wave—was used as a test problem to determine how and to what degree the mode/harmonic assumption can be made for strong waves in non-axial geometries (where natural resonance frequencies are not integer harmonics).

### 7.1 Rediscovering Heidmann

In a literature search for good experimental validation data, some work by Heidmann [26] was found that used a rotating gas jet to generate strong, spinning cylindrical waves.

This work was found to be representative of 1T waves as found in the combustion instability literature. Yet the work also appeared to be ignored by the combustion instability community. The properties of this experiment were seen to be valuable for validating nonlinear combustion instability theories.

### 7.2 The Why of Cylindrical Harmonics

The first of two questions posed at the start of the work was:

Why do cylindrical waves steepen into apparent harmonics, despite the natural resonances being non-harmonic?

Three theories were used to investigate this question, leading to three answers.

The first theory treated wave steepening as a nonlinear cascade of energy between modes, each governed by an energy balance. It was found that the frequency shift of each mode stores energy, and those frequency shifts are each

governed by an energy balance. When all modes are in balance with only one strongly unstable frequency, all other modes will shift to harmonics of that frequency.

The second theory treated steepened waves as a single fluid-dynamic motion. It was found that harmonics appear because the solution remains a periodic wave as it changes shape, and all periodic functions decompose into harmonics.

The third theory treated steepened waves as nonlinearly coupled harmonic oscillators. It was found that only harmonics appear due to the nonlinear coupling acting to drive modes at sum and difference frequencies, leading to a harmonic cascade of a driven or unstable frequency.

### 7.3 Mode/Frequency Assumption

The second of the two primary questions posed at the start concerned the quality of an assumption:

How much error is created by the mode/frequency assumption, that nonlinear steepened waves in chambers can be represented as a superposition of linear acoustic modes each ringing at a single frequency?

Four theories were used to address this question. All theories were validated against experimental data for the model problem, a strong 1T spinning wave.

The first theory, amplitude evolution derived from energy balance, made the assumption, and was found to predict the waveforms of all test cases reasonably well ( $< 7\%$  error).

The second theory, a nonlinear wave equation perturbing the linear mode shapes, did not make the assumption, yet was limited to three harmonics. The resulting solutions were found to be nearly identical to a superposition of three linear modes ringing at single frequencies: less than  $0.5\%$  error at peak-to-peak amplitudes of up to  $2.0p_0$ .

The third theory, nonlinearly coupled oscillators derived from a nonlinear wave equation, did not make the assumption, and allowed near-arbitrary solutions (among those that obey the boundary conditions). The resulting solutions were found to agree with the assumption to a high degree:  $< 1.2\%$  error at peak-to-peak amplitudes of up to  $1.2p_0$ .

The fourth theory, isentropically steepening mode shapes using CFD, did not make the assumption, and allowed near-arbitrary solutions. The resulting solutions were found to agree with the mode/frequency assumption to a reasonable degree:  $< 4\%$  error at peak-to-peak amplitudes up to  $0.9p_0$ .

### 7.4 DC Valley

In three of the four theories, a result was observed that was not discussed in the combustion instability literature reviewed: several of the modes contained a constant-offset, or zero-frequency component, in addition to the anticipated harmonic sine/cosine content. The energy-balance theory assumes that each mode has sinusoidal time dependence, and therefore could not predict a spatially-dependent DC shift. The other three different theories, with different assumptions and calculation methods, all showed this effect. This indicated that it might be a real effect (as opposed to

merely an artifact of the calculation technique). No experiments were ever performed to test for this (requiring static pressure transducers across the radius of a chamber), so this finding was not experimentally validated in this effort.

DC shift, or DC offset, of pressure is a well known phenomena in combustion instability [53] [54]. DC shifts have been observed in solid rocket motors when longitudinal modes become strong enough that nonlinear effects are important. However, a DC offset that has a spatially-varying but non-time-varying distribution was *not* among the range of expected behaviors, based upon a reading of the literature.

This time-independent, radially-distributed offset would appear, in a chamber instrumented primarily around the diameter, as a constant offset to the mean chamber pressure. The radial distribution could have important consequences to, e.g., liquid rocket engines, as it implies that different injectors are experiencing different mean pressure. This could affect stoichiometry, mixing, cooling, etc.

## 7.5 Expanded State-of-the-Art

Prior to this work, several theories predicted the behavior of strong waves in cylinders. However, these theories made assumptions that disagreed qualitatively with experiment (the acoustic mode frequencies versus harmonics). Also, these theories lacked quantitative experimental validation.

The present work quantified the error associated with assuming the nonlinear solution is a superposition of linear eigenmode solutions with altered frequencies. The error this assumption introduces was shown to grow with amplitude, possibly exponentially. However, the error was found to be less than 10% for amplitudes up to 1.2 times the mean pressure. This indicates that the assumption is a good one for most physical systems (even strongly nonlinear ones), which generally have amplitudes below 0.5 times the mean pressure.

The present work also validated all of the theories against an experiment conducted at NASA Lewis by Heidmann. This experiment was shown to have relevance to the validation of nonlinear combustion instability theories. Using this experiment the various theories were shown to have differing degrees of accuracy in capturing the physics of strong waves in cylinders.

Finally, the present work identified a spatially-dependent, time-independent DC-shift. This phenomena is likely the cause of observed DC-shift in some rocket engines, but no experiment was found in the literature which was instrumented to detect the spatial dependence of the shift. The effect is apparent in even the oldest solutions, but has not been discussed in the combustion instability literature, despite its possible importance to system performance.

## 7.6 Future Work

There are several directions that future work on this subject could take.

For further validating the mode/frequency assumption, these four theories could be applied to other geometries. Important cases would include non-longitudinal, axial geometries (e.g., cone-shaped solid rocket motors), annular cylindrical geometries (as in turbines), and non-antisymmetric geometries (e.g., ellipsoidal geometries). Further, the

recent approach of Sirignano [11] using a CFD solution technique on a nonlinear wave equation might also be applied, potentially providing additional evidence concerning the assumption.

If further validation is pursued, a number of improvements could be made to improve the calculations. Estimates could be made of the driving and viscous damping coefficients for the energy-balance and nonlinear-oscillator models, instead of the ansatz presently used. A more complete CFD model could be developed, including viscosity, heat transfer, and driving boundary conditions.

To provide a more general theory than the amplitude evolution model (which makes the mode/frequency assumption), a nonlinear oscillator model could be derived from the energy balance model. The more general time functions of this model would allow for more general steepened wave solutions, eliminating the question of the mode/frequency assumption's accuracy. Deriving an oscillator model from the energy balance theory would enable that model to employ the power of the energy balance theory, incorporating all sources and sinks of unsteady energy.

The DC valley phenomenon opens up several avenues of further investigation. Perhaps the most urgent would be to verify that it is a real phenomenon observed in experiments. A new implementation of the rotating gas jet would be an excellent way to approach that problem. Instrumenting the chamber across the radius for both static and dynamic pressure would allow the measurement of the total waveform as well as any spatial distributed mean pressure shift. Recent advances in flow diagnostics might be applied to measure 2D pressure and velocity distributions, allowing stronger validation of theories.

To determine what should be looked for in the experiment beyond the 1T spinning mode, the CFD and nonlinear oscillator theories could be applied to the the first three tangential spinning and sloshing modes, and possibly some of the higher mixed modes. This should indicate what, if any, DC shift distributions should appear in experiments if the phenomena is physical.

Should the phenomenon be experimentally verified, then theories that deal with nonlinearity need to accommodate it. Theories that already allow for it need to be validated: that they are predicting the shift. Other theories, such as the energy-balance amplitude evolution, will require extension to permit energy to be stored in this zero-frequency manner.

## **Bibliography**



- [1] J. Oefelein and V. Yang, "Comprehensive review of liquid-propellant combustion instabilities in f-1 engines," *J Propulsion and Power*, 1993.
- [2] F. Blomshield, "Historical perspective of combustion instability in motors: Case studies," *37th Joint Propulsion Conference*, 2001.
- [3] F. Culick, *Unsteady Motions in Combustion Chambers for Propulsion Systems*. RTO/NATO, 2006.
- [4] G. Flandro, "Energy balance analysis of nonlinear combustion instability," *JPP 1(3)*, 1985.
- [5] Rayleigh, *The Theory of Sound*. Dover, 1945.
- [6] B. Enflo and H. CM, *Theory of Nonlinear Acoustics in Fluids*. Kluwer Academic Publishers, 2002.
- [7] Arfken and Weber, *Mathematical Methods for Physicists*. Academic Press, 2001.
- [8] R. Saenger and G. Hudson, "Periodic shock waves in a resonating gas column," *Journal of the Acoustical Society of America* 32, 1960.
- [9] A. Coppens and J. Sanders, "Finite-amplitude standing waves within real cavities," *Journal of the Acoustical Society of America* 58, 1975.
- [10] G. Xia, M. Haravinski, W. Anderson, and M. CL, "Investigation of modeling and physical parameters on instability prediction in a model rocket combustor," *47th Joint Propulsion Conference*, 2011.
- [11] W. Sirignano and P. Popov, "Two-dimensional model for liquid-propellant transverse combustion instability," *51st Aerospace Sciences Meeting*, 2013.
- [12] F. Culick, "Nonlinear behavior of acoustic waves in combustion chambers," *Acta Astronautica* 3(9), 1976.
- [13] S. Cheng and L. Crocco, "Theory of combustion instability in liquid propellant rocket motors," *AGARD Monograph No 8, Butterworth Scientific Pub*, 1956.
- [14] E. Jacob, G. Flandro, and P. Gloyer, "Nonlinear energy transfer applied to data analysis in combustion instability," *47th Joint Propulsion Conference*, 2011.
- [15] E. Jacob, *A Study of Nonlinear Combustion Instability*. PhD thesis, The University of Tennessee Space Institute, 2009.
- [16] J. French, "Non-linear combustion instability prediction of srms using spp/ssp," *39th Joint Propulsion Conference*, 2003.
- [17] G. Flandro, E. Perry, and J. French, "Nonlinear rocket motor stability computations: Understanding the brownlee-marble observations," *44th AIAA ASM*, 2006.
- [18] G. Flandro and E. Jacob, "Finite amplitude waves in liquid rocket combustion chambers," *46th AIAA ASM*, 2010.

- [19] A. Wilson, G. Flandro, and E. Jacob, "Piston-driven oscillations and nonlinear acoustics: Validating ucds(tm) predictions," *47th Joint Propulsion Conference*, 2011.
- [20] E. Jacob, G. Flandro, and D. Banuti, "Forced resonant shock waves and mean pressure shift in a closed tube," *43rd Joint Propulsion Conference*, 2007.
- [21] S. Maslen and F. Moore, "On strong transverse waves without shocks in a circular cylinder," *Journal of Aeronautical Sciences*, Vol 23, No 6, vol. ., 1956.
- [22] B. Zinn and E. Powell, "Application of the galerkin method in the solution of combustion-instability problems," *Proc. of 19th International Astronautical Congress 1968*, 1970.
- [23] V. Yang and F. Culick, "On the existence and stability of limit cycles for transverse acoustic oscillations in a cylindrical combustion chamber 1: Standing modes," *Combust. Sci. and Tech. Vol 72*, 1990.
- [24] V. Burnley, *Nonlinear Combustion Instability and Stochastic Sources*. PhD thesis, California Institute of Technology, 1996.
- [25] E. Jacob, G. Flandro, P. Gloyer, and J. French, "Nonlinear liquid rocket combustion instability behavior using ucds(tm) process," *46th Joint Propulsion Conferenc*, 2010.
- [26] M. Heidmann, "Strong, traveling, transverse acoustic modes generated by a rotating gas jet.," *AIAA Journal* 5, 1967.
- [27] M. Heidmann and C. Feiler, "Evaluation of tangential velocity effects on spinning transverse combustion instability," *NASA TN D-2306*, 1966.
- [28] D. Harrje and F. Reardon, "Liquid propellant rocket combustion instability," *NASA SP-194*, 1972.
- [29] R. Sackheim, "Kickoff presentation: Focused on rocket engine/motor instability issues," *Workshop on the Future of Modeling and Simulation for Combustion Applications*, 2006.
- [30] V. Brownlee, *An Experimental Investigation of Unstable Combustion in Solid Propellant Rocket Motors*. PhD thesis, California Institute of Technology, 1959.
- [31] H. Krieg, "Tangential mode of combustion instability, detonation and two-phase flow," *Progress in Astronautics and Rocketry*, Vol 6, 1964.
- [32] F. Reardon, L. Crocco, and D. Harrje, "Transverse combustion instability in liquid propellant rocket motors," *ARS J* 32, 1962.
- [33] J. Sotter, J. Woodward, and R. Clayton, "Injector response to strong, high-frequency pressure oscillations," *J. Spacecraft*, 1969.

- [34] F. Blomshield, C. Beiter, H. Mathes, J. Crump, and M. Beckstead, "Nonlinear stability testing and pusling of full scale tactical motors," *AIAA JPC*, 1991.
- [35] G. Settles, *Schlieren and Shadowgraph Techniques: Visualizing Phenomena in Transparent Media*. Springer, 2001.
- [36] R. Saenger, *Periodic Shock Waves in Resonating Gas Columns*. PhD thesis, New York University, 1958.
- [37] S. Temkin, "Nonlinear gas oscillations in a resonant tube," *The Physics of Fluids, Vol 11 No 5*, 1968.
- [38] C. Morfey and S. Temkin, "Unstable combustion of advanced solid propellants," *Bolt Beranek and Newman Inc, BBN Report No 1547*, 1967.
- [39] A. Wilson, "Nonlinear acoustics of piston-driven gas-column oscillations," *UTSI Thesis*, 2010.
- [40] P. Caap and P. Monkewitz, "An experimental and theoretical study of radial acoustic resonance in a cylindrical cavity," *Journal of Sound and Vibration, 108(1)*, 1986.
- [41] B. Phillips, C. Morgan, and J. Kauffman, "Mechanical absorpotion of acoustic oscillations in simulated rocket combustion chambers," *NASA TN D-3792*, 1967.
- [42] M. Heidmann, "Emperical characterization of some pressure wave shapes in strong traveling transverse acoustic modes," *NASA TM X-1716*, 1969.
- [43] G. Flandro, "Private communication," ., 2013.
- [44] M. Heidmann, "Performance study of rotating gas jet generator for strong traveling transverse acoustic modes," *NASA TN D-4380*, 1968.
- [45] C. Oberg, R. Kesselring, C. Warner III, and M. Schuman, "Analysis of combustion instability in liquid propellant engines with or without acoustic cavities," ??, 1974.
- [46] M. Heidmann, "Amplification by wave distortion in unstable combustors," *AIAA Journal*, 1971.
- [47] E. Jacob, "Private communication," ., 2013.
- [48] E. Powell, *Nonlinear Combustion Instability in Liquid Propellant Rocket Engines*. PhD thesis, Georgia Institute of Technology, 1970.
- [49] M. Liou, "A sequel to ausm, part ii: Ausm-plus-up for all speeds," *Journal of Computational Physics 214*, 137-170, 2006.
- [50] E. Toro, *Riemann Solvers and Numerical Methods for Fluid Dynamics*. Springer, 1997.
- [51] C. Tam, "Computational aeroacoustics: An overview of computational challenges and applications," *International Journal of Computational Fluid Dynamics, Vol 18(6) pp 547-567*, 2004.

- [52] K. Masatsuka, *I do like CFD*. Masatsuka, 2012.
- [53] G. Flandro, "Irregular burning: On the origin of the dc shift," *43rd Joint Propulsion Conference*, 2007.
- [54] S. Malhotra and G. Flandro, "On the origin of the dc shift," *AIAA Paper 97-3249*, 1997.
- [55] M. Myers, "An exact energy corollary for homentropic flow," *Journal of Sound and Vibrations*, vol 109, 1986.
- [56] R. Cantrell and R. Hart, "Interaction between sound and flow in acoustic cavities: Mass, momentum, and energy transfer," *J. Acoust. Soc. Amer* vol36, 1966.
- [57] H. Liepmann and A. Roshko, *Elements of Gasdynamics*. Dover Publications Inc., 1957.
- [58] A. Quarteroni, R. Sacco, and F. Saleri, *Numerical Mathematics*. Springer, 2007.
- [59] P. Morse and K. Ingard, *Theoretical Acoustics*. McGraw-Hill Book Company, 1968.
- [60] V. Kuznetsov, "Equations of nonlinear acoustics," ??, 1971.
- [61] L. Soderholm, "On the kuznetsov equation and higher order nonlinear acoustics," *Nonlinear Acoustics at the Turn of the Millennium*, 2000.

## Appendices

# Appendix A

## Energy Balance: Derivation

The theory described here is attributed to Flandro [4], based on work by Myers [55] and Cantrell & Hart [56], and exactly follows the version laid out by Jacob [15] and Wilson [39], with two modifications: The theory explicitly assumes a cylindrical geometry (as mentioned without derivation by Jacob [15]), and the damping/driving terms are only considered for their functional dependencies, not their exact values.

The derivation proceeds as follows:

- In Section A.1, a complete set of independent fluid and thermodynamic variables are chosen, and said variables are assumed to have an expanded / perturbed form.
- In Section A.2, an appropriate, closed set of governing equations (fluid dynamic, thermodynamic, and state) are chosen.
- In Section A.3, the energy balance equation is expanded around the mean (or zeroth-order) variables.
- In Sections A.3.1, A.3.2, and A.3.3, the energy balance equation is examined at each order.
- Section A.4 documents the assumptions made about the system.
- Section A.5 decomposes the fluctuations into individual acoustic modes.
- In Sections A.6, A.7, and A.8, the expansion is substituted into the expanded terms of the energy balance equation.
- Finally, in Section A.9, the resulting terms are time averaged and volume-integrated, isolating the the amplitude functions  $\{R_n\}$ .

This gives a dynamic model for amplitude evolution in time, which classically looks like

$$\dot{R}_n = \underbrace{\left( \sum_j \alpha_{n,j} \right) R_n}_{\text{feedback sources and sinks}} - \underbrace{\frac{2-\gamma}{8\gamma} \omega_n \sum_{l,m=1}^{\infty} E_{n,l,m} R_l R_m}_{\text{nonlinear mode coupling}} \quad (\text{A.1})$$

## A.1 Variables and Expansions

Motivated by a desire to choose the entropy equation (over the energy equation), the following independent field variables are selected:

$$\vec{u} = \vec{u}_0 + \vec{u}_1 + \vec{u}_2 + \dots \quad (\text{A.2})$$

$$p = p_0 + p_1 + p_2 + \dots \quad (\text{A.3})$$

$$\rho = \rho_0 + \rho_1 + \rho_2 + \dots \quad (\text{A.4})$$

$$T = T_0 + T_1 + T_2 + \dots \quad (\text{A.5})$$

$$s = s_0 + s_1 + s_2 + \dots \quad (\text{A.6})$$

$$(\text{A.7})$$

where

$$\frac{|\Xi|}{\Xi_0} \approx \epsilon^i, \quad (\text{A.8})$$

$\epsilon$  is a small quantity ( $\ll 1$ ), and  $\Xi \in \{\vec{u}, p, \rho, T, s\}$ .

For convenience, mass flux is defined:

$$\vec{m} = \vec{m}_0 + \vec{m}_1 + \vec{m}_2 + \dots \quad (\text{A.9})$$

$$\equiv \rho \vec{u} \quad (\text{A.10})$$

$$= (\rho_0 + \rho_1 + \dots)(\vec{u}_0 + \vec{u}_1 + \dots) \quad (\text{A.11})$$

$$= (\rho_0 \vec{u}_0) + (\rho_0 \vec{u}_1 + \rho_1 \vec{u}_0) + \dots \quad (\text{A.12})$$

## A.2 Defining Equations

Based upon the choice of variables, the following governing equations are required: two thermodynamic relations, an equation of state, and five fluid mechanic equations (three for the vector velocity plus density and entropy).

The thermodynamic relations are (for derivations, see Liepman and Roshko [57]):

$$dp = \frac{a^2 \rho}{c_p} ds + a^2 d\rho \quad (\text{A.13})$$

$$dT = \frac{T}{c_p} ds + \frac{1}{\rho c_p} dp \quad (\text{A.14})$$

A thermally perfect gas is assumed, with speed of sound:

$$a = \sqrt{\gamma RT} \quad (\text{A.15})$$

Table A.1: Additional variables and their defining equations.

	Variable	Defining equation
$h$	enthalpy	$h = e + \frac{p}{\rho}$
$e$	internal energy	$de = T ds + \frac{p}{\rho^2} d\rho$
$H$	total enthalpy	$H = h + \frac{1}{2}\vec{u}^2$
$\vec{\omega}$	vorticity	$\vec{\omega} = \nabla \times \vec{u}$
$\vec{\zeta}$	lambda vector	$\vec{\zeta} = \vec{\omega} \times \vec{u}$
$Q$	heat release	$Q = \frac{1}{T}(\Phi - \nabla \cdot \vec{q} + \mathcal{H})$
$\mathcal{H}$	distributed heat release	
$\vec{q}$	heat transfer	
$\vec{\psi}$	viscous stress	$\vec{\psi} = \frac{1}{\rho}(-\mu\nabla \times \nabla \times \vec{u} + (\eta + \frac{4}{3}\mu)\nabla(\nabla \cdot \vec{u}) + \vec{F})$
$\vec{F}$	body force	
$\Phi$	viscous dissipation	$P_{ij} \frac{\partial u_j}{\partial x_i}$
$P_{ij}$	transposed stress tensor	$P_{ij} = \sigma'_{ij} = \mu \left( \frac{\partial v_i}{\partial x_j} + \frac{\partial v_j}{\partial x_i} - \frac{2}{3} \delta_{ik} \frac{\partial v_l}{\partial x_l} \right) + \eta \delta_{ik} \frac{\partial v_l}{\partial x_l}$

and further an ideal gas is assumed with equation of state:

$$p = \rho RT \quad (\text{A.16})$$

The five fluid mechanic equations are continuity, vector momentum (three equations in one vector equation), and entropy:

$$\frac{\partial \rho}{\partial t} + \nabla \cdot \vec{m} = 0 \quad \text{Continuity} \quad (\text{A.17})$$

$$\frac{\partial \vec{u}}{\partial t} + \vec{\omega} \times \vec{u} + \nabla H - T \nabla s = \vec{\psi} \quad \text{Momentum} \quad (\text{A.18})$$

$$\frac{\partial(\rho s)}{\partial t} + \nabla \cdot (\vec{m} s) = Q \quad \text{Entropy} \quad (\text{A.19})$$

The additional variables used in these equations are given in Table A.1.

Although not required, there are additional thermodynamic relations that are of use in some of the derivations. For completeness, the entire set of thermodynamic relations are summarized in Table A.2.



Table A.2: The thermodynamic relations.

Symbol	Variable	Relation
$e$	internal energy	$de = T ds + \frac{p}{\rho^2} d\rho$
$h$	enthalpy	$T ds + \frac{1}{\rho} dp$ $\gamma T ds + \frac{a^2}{\rho} d\rho$
$p$	pressure	$dp = \frac{a^2 \rho}{c_p} ds + a^2 d\rho$
$T$	temperature	$dT = \frac{T}{c_p} ds + \frac{1}{\rho c_p} dp$ $dT = \frac{1}{c_p} (\gamma T ds + \frac{a^2}{\rho} d\rho)$

### A.3 Finalized Energy Balance

By applying the zeroth order equations, Jacob [15] finds the energy balance to be

$$\frac{\partial E}{\partial t} + \nabla \cdot \vec{W} = D \quad (\text{A.20})$$

with

$$E = \rho((H - H_0 - T_0(s - s_0)) - \vec{m}_0 \cdot (\vec{u} - \vec{u}_0)) - (p - p_0) \quad (\text{A.21})$$

$$W = (\vec{m} - \vec{m}_0)((H - H_0) + T_0(s - s_0)) + \vec{m}_0(T - T_0)(s - s_0) \\ - (m_j - m_{0j}) \left( \frac{P_{ij}}{\rho} - \frac{P_{0ij}}{\rho_0} \right) + (T - T_0) \left( \frac{\vec{q}}{T} - \frac{\vec{q}_0}{T_0} \right) \quad (\text{A.22})$$

$$D = \vec{m} \cdot \vec{\zeta}_0 + \vec{m}_0 \cdot \vec{\zeta} - (s - s_0)\vec{m} \cdot \nabla T_0 + (s - s_0)\vec{m}_0 \cdot \nabla T \\ - \left( \frac{P_{ij}}{\rho} - \frac{P_{0ij}}{\rho_0} \right) \frac{\partial}{\partial x_i} (m_j - m_{0j}) \\ + (m_j - m_{0j}) \left( \frac{P_{ij}}{\rho^2} \frac{\partial \rho}{\partial x_i} - \frac{P_{0ij}}{\rho_0^2} \frac{\partial \rho_0}{\partial x_i} \right) \\ + (T - T_0) \left( \frac{\phi}{T} - \frac{\phi_0}{T_0} \right) + \left( \frac{\vec{q}}{T} - \frac{\vec{q}_0}{T_0} \right) \cdot \nabla (T - T_0) \\ - (T - T_0) \left( \frac{\vec{q} \cdot \nabla T}{T^2} - \frac{\vec{q}_0 \cdot \nabla T_0}{T_0^2} \right) \quad (\text{A.23})$$

#### A.3.1 1st Order Energy

When the completely expanded variables are substituted into the energy balance, Jacob shows that the energy balance equation to first order

$$\frac{\partial E_1}{\partial t} + \nabla \cdot \vec{W}_1 = D_1 \quad (\text{A.24})$$

collapses to  $0 = 0$ ; that is, the expansion itself satisfies the first order energy constraint and reveals no relationships between the first order variables.

#### A.3.2 2nd Order Energy

The second order equation establishes relationships between the first order variables:

$$\frac{dE_2}{dt} + \nabla \cdot \vec{W}_2 = D_2 \quad (\text{A.25})$$

where

$$E_2 = \frac{p_1^2}{2\rho_0 a_0^2} + \rho_1(\vec{u}_0 \cdot \vec{u}_1) + \frac{1}{2}\rho_0(\vec{u}_1 \cdot \vec{u}_1) + \frac{\rho_0 T_0}{2c_p} s_1^2 \quad (\text{A.26})$$

$$\vec{W}_2 = \vec{m}_1(h_1 + \vec{u}_0 \cdot \vec{u}_1) - \vec{m}_1 T_0 s_1 + \vec{m}_0 T_1 s_1 \quad (\text{A.27})$$

$$D_2 = \vec{m}_1 \cdot \vec{\psi}_1 + T_1 Q_1 - \vec{m}_1 s_1 \cdot \nabla T_0 + \vec{m}_0 s_1 \cdot \nabla T_1 - \rho_0 \vec{u}_0 \cdot (\vec{u}_1 \times \vec{\omega}_1) - \rho_1 \vec{u}_1 \cdot (\vec{u}_0 \times \vec{\omega}_0) \quad (\text{A.28})$$

### A.3.3 3rd Order Energy

The full (and extensive) third-order energy balance result derived by Jacob establishes some relationships among second-order variables. But the third-order energy term itself reveals an additional relationship between first-order variables:

$$E_3 = \frac{1}{2}\rho_1 \vec{u}_1^2 + \frac{1-2\gamma}{6\rho_0^2} p_1^3 \quad (\text{A.29})$$

This nonlinear coupling results in energy transfer between the various acoustic modes.

## A.4 Cylinder Mode Assumptions

To obtain solutions for the system of interest, relevant assumptions are made. For an acoustic experiment with no mean flow, assume:

$$\vec{u}_0 \equiv 0 \quad \text{no mean flow} \quad (\text{A.30})$$

$$s_1 \equiv 0 \quad \text{entropy fluctuations negligible} \quad (\text{A.31})$$

$$\vec{\omega}_0 \equiv 0 \quad \text{irrotational mean flow (from no mean flow)} \quad (\text{A.32})$$

Further, assume there is driving at the 1T resonant frequency,  $\omega_{1T}$ .

## A.5 Acoustic Decomposition

Following Jacob [15] and based on the work of Quarteroni et al. [58], the decomposition for a short, flat circular chamber is a standard Galerkin spectral decomposition:

$$p_1 = p_0 \sum_{n=1}^{\infty} \eta_n(t) \psi_n(\vec{r}) \quad (\text{A.33})$$

$$u_1 = \sum_{n=1}^{\infty} \frac{1}{\gamma k_n^2} \dot{\eta}_n(t) \nabla \psi_n(\vec{r}) \quad (\text{A.34})$$

$$\eta_n = R_n \sin(\omega_n t) \quad (\text{A.35})$$

$$\psi_n = \cos\left(m_n \theta + \frac{\pi}{2} \chi_n\right) J_{m_n}\left(\lambda_n \frac{r}{R}\right) \quad (\text{A.36})$$

$$\omega_n = j_n * \lambda_{m_n} \frac{a_0}{R} \quad (\text{A.37})$$

$$k_n = \frac{\omega_n}{a_0} \quad (\text{A.38})$$

$$m_n = 0, 1, 2, 3, \dots \quad \text{number of modal diameters} \quad (\text{A.39})$$

$$j_n = 0, 1, 2, 3, \dots \quad \text{number of modal circles} \quad (\text{A.40})$$

$$\lambda_{m_n} = j_n \text{ root of } J'_{m_n}(r) \quad (\text{A.41})$$

$$\chi_n = \begin{cases} 0, & \cos(m\theta) \text{ solutions} \\ -1, & \sin(m\theta) \text{ solutions} \end{cases} \quad (\text{A.42})$$

## A.6 Source: Driving Work

The previous work with this theory focused on the self-excited oscillations common in combustion devices, or piston-driving as used in active control systems and acoustics experiments. Here, the primary source of oscillating energy is the work done by a rotating gas-jet. The theory had never been used before with systems this kind of driving, therefore the work term needed to be evaluated and the time/space-averaging procedure applied.

The work term  $\vec{W}_2$  in the second order energy balance is given by

$$\vec{W}_2 = \vec{m}_1(h_1 + \vec{u}_0 \cdot \vec{u}_1) - \vec{m}_1 T_0 s_1 + \vec{m}_0 T_1 s_1 \quad (\text{A.43})$$

Table A.3 inserts expansions and assumptions into this expression for  $\vec{W}_2$ , which simplifies to

$$\vec{W}_2 = \vec{u}_1 p_1 \quad (\text{A.44})$$

Integrating to get the total rate of work done, and applying the divergence theorem,

$$\int_V \nabla \cdot \vec{W}_2 dV = \int_S \hat{n} \cdot (\vec{u}_1 p_1) dS \quad (\text{A.45})$$

Note that  $\vec{u}_1$  vanishes everywhere except at the inlet of the rotating gas jet, which has area  $A_p$ , offset from center  $R_j$ , injection velocity  $U_j$ , and azimuthal rotation  $\theta_j(t) = \omega_1 T t$ .

Evaluating this integral does not result in the usual form of the  $\alpha$  constant. The equation  $R' = \alpha R$  is a feedback equation, where the change in oscillations depends upon the already existing oscillations. But this is a driven system, and therefore energy will be added whether oscillations currently exist or not. Hence a constant term  $\zeta_n$  is required to in the dynamic model:

$$\dot{R}_n = \alpha_n R_n + \zeta_n \quad (\text{A.46})$$

Solutions to this equation have a linear, unbounded rise in amplitude at the driven resonant frequency, with no other frequencies excited. Nonlinear terms and viscous damping are required to prevent this non-physical result.

## A.7 Sink: Viscous Boundary Layer Losses

In his textbook, Culick [3] derived the growth constant  $\alpha$  due to viscous losses in the acoustic boundary layer of a cylinder. For the sake of brevity the derivation will not be repeated here. Rather, it can be shown that the boundary layer growth constant is given by:

$$\alpha_{bl,n} = -\frac{1}{R_t} \sqrt{\frac{\omega_n \nu}{2}} \left( 1 + \frac{\gamma - 1}{\sqrt{Pr}} \right) \quad (\text{A.47})$$

Table A.3: Assumptions and expansions applied to  $\vec{W}_2$ .

$\vec{W}_2$	substitution	reason
$\vec{m}_1(h_1 + \vec{u}_0 \cdot \vec{u}_1) - \vec{m}_1 T_0 s_1 + \vec{m}_0 T_1 s_1$		Second order energy
$\vec{m}_1(h_1 + \vec{u}_0 \cdot \vec{u}_1) - \vec{m}_1 T_0 s_1 + \vec{m}_0 T_1 s_1$	$s_1 \equiv 0$	Entropy fluctuations neglected
$\vec{m}_1(h_1 + \vec{u}_0 \cdot \vec{u}_1)$		
$\vec{m}_1(h_1 + \vec{u}_0 \cdot \vec{u}_1)$	$\vec{u}_0 \equiv 0$	No mean flow
$\vec{m}_1 h_1$		
$(\rho_0 \vec{u}_1 + \rho_1 \vec{u}_0) h_1$	$\vec{m}_1 = \rho_0 \vec{u}_1 + \rho_1 \vec{u}_0$	From variable expansion
$(\rho_0 \vec{u}_1 + \rho_1 \vec{u}_0) h_1$		
$(\rho_0 \vec{u}_1 + \rho_1 \vec{u}_0) h_1$	$\vec{u}_0 \equiv 0$	No mean flow
$\rho_0 \vec{u}_1 h_1$		
$\rho_0 \vec{u}_1 \left( \frac{p_1}{\rho_0} + \left( \gamma T_1 - \frac{a_0^2}{c_p} \right) s_1 \right)$	$h_1 = \frac{p_1}{\rho_0} + \left( \gamma T_1 - \frac{a_0^2}{c_p} \right) s_1$	From variable expansion
$\rho_0 \vec{u}_1 \left( \frac{p_1}{\rho_0} + \left( \gamma T_1 - \frac{a_0^2}{c_p} \right) s_1 \right)$		
$\rho_0 \vec{u}_1 \left( \frac{p_1}{\rho_0} + \left( \gamma T_1 - \frac{a_0^2}{c_p} \right) s_1 \right)$	$s_1 \equiv 0$	Entropy fluctuations neglected
$\rho_0 \vec{u}_1 \frac{p_1}{\rho_0}$		
$\rho_0 \vec{u}_1 \frac{p_1}{\rho_0}$		(canceling)
$\vec{u}_1 p_1$		

## A.8 Sink: Compressive Viscous Losses

Morse and Ingard [59] derive the rate of energy loss per unit volume  $D_{cv}$  due to the effects of compressive viscosity in an acoustic wave to be

$$D_{cv} = (\eta + \frac{4}{3}\mu) \left\langle \left| \frac{du_x}{dx} \right|^2 \right\rangle \quad (\text{A.48})$$

The same process is applied to this source term: substitute the spectral expansion, time average, and volume integrate. For a longitudinal excitation of a long, thin tube, this results in an  $\alpha$ :

$$\begin{aligned} \alpha_{cv} &= (\gamma_{II} + 4/3)\mu \frac{\omega_n^2}{2\rho_0 RT_0 \gamma} \\ &= (\gamma_{II} + 4/3) \frac{\mu}{\rho_0} \frac{\omega_n^2}{2a_0^2} \\ &= (\gamma_{II} + 4/3)v \frac{\omega_n^2}{2a_0^2} \end{aligned} \quad (\text{A.49})$$

This shows an  $\omega_n^2$  dependence for the compressive viscous losses. This  $\omega_n^2$  rapidly dominates the  $\sqrt{\omega_n}$  dependence of the boundary layers, causing this compressive viscous effect to dominate the viscous losses.

Rather than performing exact computations for the viscous coefficient, an ansatz based upon this dependence was used.

## A.9 Dynamic Model

Following Flandro (and applying the changes required by driving), the dynamic model used was:

$$\dot{R}_n = \underbrace{\left( \sum_j \alpha_{n,j} \right) R_n}_{\text{feedback sources and sinks}} + \underbrace{\sum_k \zeta_{n,k}}_{\text{forced sources and sinks}} - \underbrace{\frac{2-\gamma}{8\gamma} \omega_n \sum_{l,m=1}^{\infty} E_{n,l,m} R_l R_m}_{\text{nonlinear mode coupling}} \quad (\text{A.50})$$

## Appendix B

# Steepening: Alternate Wave Equation

## Derivation

Maslen and Moore derived a nonlinear wave equation directly from the governing equations of gas dynamics. They then applied the method of strained parameters to derive a series of linear, inhomogeneous ordinary differential equations governing components of the solution.

This derivation used a different wave equation to derive governing equations. The wave equation was derived by Kuznetsov [60] and expanded on by Söderholm [61], and (as used here) was described in Enflo [6].

The procedure followed by Maslen and Moore, and emulated here, is:

1. State the governing equations (fluid, thermodynamic, state).
2. Reduce the number of field variables to one (potential flow).
3. Derive a (nonlinear) wave equation (eliminate variables from the governing equations).
4. Reduce the nonlinear problem into a series of linear problems (perturb the wave equation).
5. Apply boundary conditions to solve the first-order problem (find the eigenvalue / eigenfunction solution space).
6. Use the first-order solutions to solve for second-order corrections.
7. Use the first- and second-order solutions to solve for third-order corrections.

### B.1 Governing Equations

Strong wave in cylinders are unsteady, compressible, thermodynamic flows. With an Eulerian perspective, the solution consists of field variables specified at every point in space ( $\vec{x}$ ) and time ( $t$ ):

- $\rho$  density
- $p$  pressure
- $T$  temperature
- $\vec{u}$  fluid velocity

This requires knowledge of thermodynamic properties of the fluid as a function of pressure and temperature:

- $s$  entropy
- $h$  enthalpy
- $e$  internal energy
- $\kappa$  thermal conductivity
- $\mu$  shear viscosity
- $\zeta = \frac{2}{3}\lambda_{\text{bulk}}$  (compressive) viscosity

The governing equations are the physical conservation equations,

$$\text{Mass: } \left[ \frac{\partial \rho}{\partial t} + \nabla(\rho \vec{u}) \right] = 0 \quad (\text{B.1})$$

$$\text{Momentum: } \rho \left[ \frac{\partial \vec{u}}{\partial t} + (\vec{u} \cdot \nabla) \vec{u} \right] = -\nabla p + \eta \nabla^2 \vec{u} + \left( \zeta + \frac{\eta}{3} \right) \nabla(\nabla \cdot \vec{u}) \quad (\text{B.2})$$

$$\text{Energy: } \rho T \left[ \frac{\partial s}{\partial t} + (\vec{u} \cdot \nabla) s \right] = \kappa \nabla^2 T + \zeta (\nabla \cdot \vec{u})^2 + \frac{1}{2} \eta \left( \frac{\partial u_j}{\partial x_i} + \frac{\partial u_i}{\partial x_j} - \frac{2}{3} \nabla \cdot \vec{u} \delta_{ij} \right)^2 \quad (\text{B.3})$$

combined with thermodynamic state equations:

$$\text{Ideal fluid: } p = (c_p - c_v) \rho T \quad (\text{B.4})$$

$$\text{Enthalpy of ideal fluid: } h(p, T) = c_p T \quad (\text{B.5})$$

$$\text{Constant shear viscosity: } \mu(p, T) = \mu_0 \quad (\text{B.6})$$

$$\text{Constant bulk viscosity: } \zeta(p, T) = \zeta_0 \quad (\text{B.7})$$

$$\text{Constant thermal conductivity: } \kappa(p, T) = \kappa_0 \quad (\text{B.8})$$

$$\text{Constant specific heats: } c_p(p, T) = (c_p)_0, c_v(p, T) = (c_v)_0 \quad (\text{B.9})$$

Note the assumptions made. Constant diffusion properties ( $\mu, \zeta, \kappa$ ) were assumed in the derivation of the momentum and energy equations as presented. The ideal fluid assumption led to simpler forms of most of the thermodynamic relations. Implicitly, the fluid was assumed to be everywhere in local thermodynamic equilibrium. At an even more fundamental level, the continuum assumption was made to use these forms of the governing equations. For strong waves, the constant diffusion property assumption may not hold. For short wavelengths, the continuum assumption may not hold. For steep gradients, the equilibrium assumption may not hold. However, the various length, time, frequency and amplitude scales required for these assumptions to break down are well beyond those in any of the simulations under consideration.



## B.2 Potential Flow

The velocity field was assumed to be irrotational, and thus represented by the gradient of a scalar potential  $\Phi$ .

$$\nabla \times \vec{u} = 0 \quad (\text{B.10})$$

$$\vec{u} = -\nabla\Phi \quad (\text{B.11})$$

Additionally, the flow was assumed isentropic, which yielded

$$p = p_0 \left( \frac{\rho}{\rho_0} \right)^\gamma \quad (\text{B.12})$$

## B.3 Wave Equation

To obtain a wave equation, further assumptions were introduced. The thermodynamic field variables were assumed to have spatially and temporally constant equilibrium values  $\rho_0, p_0, T_0, s_0$ . The fluid was assumed to have a zero steady velocity,  $\vec{u}_0 = 0$ . The space and time dependence of all field variables  $\rho, p, T, s, \vec{u}$  was assumed to be “small” with respect to their equilibrium values. Likewise, the diffusion coefficients  $\kappa, \eta, \zeta$  were assumed to be “small”, i.e., some dimensionless number associated with them is much less than unity, as described in Enflo [6].

Let  $a_0$  be the mean speed of sound,  $\gamma$  the ratio of specific heats of an ideal gas,  $\rho_0$  the mean density, and  $b$  a diffusion parameter (defined below in equation B.14). Assume that viscosity and thermal diffusion coefficients are “small”. Under these assumptions, Soderholm [61] gave a detailed derivation leading to a nonlinear wave equation  $3^{rd}$ -order accurate in nonlinear terms and  $2^{nd}$ -order accurate in viscous terms:

$$\frac{\partial^2 \Phi}{\partial t^2} - a_0^2 \nabla^2 \Phi = -\frac{\partial}{\partial t} \left( (\nabla \Phi)^2 \right) - \frac{1}{2} \nabla \Phi \cdot \nabla \left( (\nabla \Phi)^2 \right) - (\gamma - 1) \left( \frac{\partial \Phi}{\partial t} + \frac{1}{2} (\nabla \Phi)^2 \right) \nabla^2 \Phi + b \nabla^2 \frac{\partial \Phi}{\partial t} \quad (\text{B.13})$$

The diffusion parameter combines the effects of thermal conductivity  $k$ , shear viscosity  $\eta$ , and compressive viscosity  $\zeta = 2/3\mu$  (with the usual specific heats  $c_p, c_v$ ):

$$b = \kappa \left( \frac{1}{c_v} - 1 c_p \right) + \frac{4}{3} \eta + \zeta \quad (\text{B.14})$$

As Enflo describes it, “to second order in the small quantities, the total effect of viscosity and heat conduction is given by a single constant  $b$ ” (page 23 of [6]). Note that Enflo’s chief concern is sound waves as radiation, and that acoustic boundary layers do not contribute strongly to losses in those conditions. In other words, this equation accounts for bulk losses due to thermal conductivity and viscosity to second order. The irrotational assumption precludes this equation from capturing the acoustic boundary layer that contributes strongly to losses in cavities.

Perturbing the wave equation B.13:

$$\Phi(\vec{x}, t) = \phi_0 + \epsilon\phi_1 + \epsilon^2\phi_2 + \epsilon^3\phi_3 + \dots \quad (\text{B.15})$$

$$\phi_0 = \text{constant} \equiv 0 \quad (\text{no mean flow}) \quad (\text{B.16})$$

$$\frac{\partial^2 \phi_1}{\partial t^2} - c_0^2 \nabla^2 \phi_1 = 0 \quad (\text{B.17})$$

$$\frac{\partial^2 \phi_2}{\partial t^2} - c_0^2 \nabla^2 \phi_2 = -\frac{\partial}{\partial t} \left[ \nabla \phi_1 \cdot \nabla \phi_1 + \frac{\gamma-1}{2a_0^2} \frac{\partial \phi_1}{\partial t} \frac{\partial \phi_1}{\partial t} \right] + b \nabla^2 \frac{\partial \phi_1}{\partial t} \quad (\text{B.18})$$

$$\frac{\partial^2 \phi_3}{\partial t^2} - c_0^2 \nabla^2 \phi_3 = -\frac{\partial}{\partial t} \left[ 2 \nabla \phi_1 \cdot \nabla \phi_2 + \frac{\gamma-1}{a_0^2} \frac{\partial \phi_1}{\partial t} \frac{\partial \phi_2}{\partial t} \right] + b \nabla^2 \frac{\partial \phi_2}{\partial t} \quad (\text{B.19})$$

$$-\frac{1}{2} \nabla \phi_1 \cdot \nabla \left( (\nabla \phi_1)^2 \right) - \frac{\gamma-1}{2} (\nabla \phi_1)^2 \nabla^2 \phi_1 \quad (\text{B.20})$$

For comparison, Maslen and Moore's (non-dimensional) perturbed equations are

$$\Phi(\vec{x}, t) = \phi_0 + \epsilon\phi_1 + \epsilon^2\phi_2 + \epsilon^3\phi_3 + \dots \quad (\text{B.21})$$

$$\phi_0 = \text{constant} \equiv 0 \quad (\text{no mean flow}) \quad (\text{B.22})$$

$$\frac{\partial^2 \phi_1}{\partial t^2} - c_0^2 \nabla^2 \phi_1 = 0 \quad (\text{B.23})$$

$$\frac{\partial^2 \phi_2}{\partial t^2} - c_0^2 \nabla^2 \phi_2 = -\frac{\partial}{\partial t} \left[ \nabla \phi_1 \cdot \nabla \phi_1 + \frac{\gamma-1}{2a_0^2} \frac{\partial \phi_1}{\partial t} \frac{\partial \phi_1}{\partial t} \right] \quad (\text{B.24})$$

$$\frac{\partial^2 \phi_3}{\partial t^2} - c_0^2 \nabla^2 \phi_3 = -\frac{\partial}{\partial t} \left[ 2 \nabla \phi_1 \cdot \nabla \phi_2 + \frac{\gamma-1}{a_0^2} \frac{\partial \phi_1}{\partial t} \frac{\partial \phi_2}{\partial t} \right] \quad (\text{B.25})$$

$$-\frac{1}{2} \nabla \phi_1 \cdot \nabla \left( (\nabla \phi_1)^2 \right) \quad (\text{B.26})$$

$$+ \frac{\gamma-1}{2} (\nabla \phi_1)^2 \frac{\partial^2 \phi_1}{\partial t^2} \quad (\text{B.27})$$

$$-(\gamma-1)^2 \frac{\partial \phi_1}{\partial t} \frac{\partial \phi_1}{\partial t} \frac{\partial^2 \phi_1}{\partial t^2} \quad (\text{B.28})$$

$$-\frac{\partial}{\partial t} \left[ (\gamma-1) \nabla \phi_1 \cdot \nabla \phi_1 \frac{\partial \phi_1}{\partial t} \right] \quad (\text{B.29})$$

This showed that Maslen and Moore captured all the nonlinear effects of the most recent developments in nonlinear acoustics, and even captured some nonlinear effects not captured by those developments. Further, the viscous terms of Solderholm's equation are largely irrelevant for cavity waves (in which the primary losses are in the boundary layers, not the fluid bulk). As such, Maslen and Moore's approach was seen as preferable for strong waves in cylinders, where nonlinearity is expected to dominate over viscosity.

## Appendix C

# Example Nonlinear Oscillator Simulation

The following tables show the details of one simulation using the nonlinear oscillator approach outlined in Chapter 5.

Through the tables, the numbers in the left cells indicate the mode's properties:

- $f$  is the natural frequency
- $i$  is the number of nodal diameters (also the number of the associated Bessel function)
- $j$  is the number of nodal circles (corresponding to the  $j^{\text{th}}$  root of the Bessel derivative)

The left plot in each row shows a generic mode shape (it can be thought of as the unit pressure wave for that mode).

The middle figure of each plots  $\eta_n(t)$  versus time for one mode, throughout a 2 second simulation. Note that all these plots have the same bounds, so the higher modes which do not appear to have much happening are very low amplitude.

The right plot of each row shows two periods from each mode's time function  $\eta_n(t)$  after limit cycle is attained.

The plots in figure C.1 follow this same pattern, but top-to-bottom, not left-to-right.

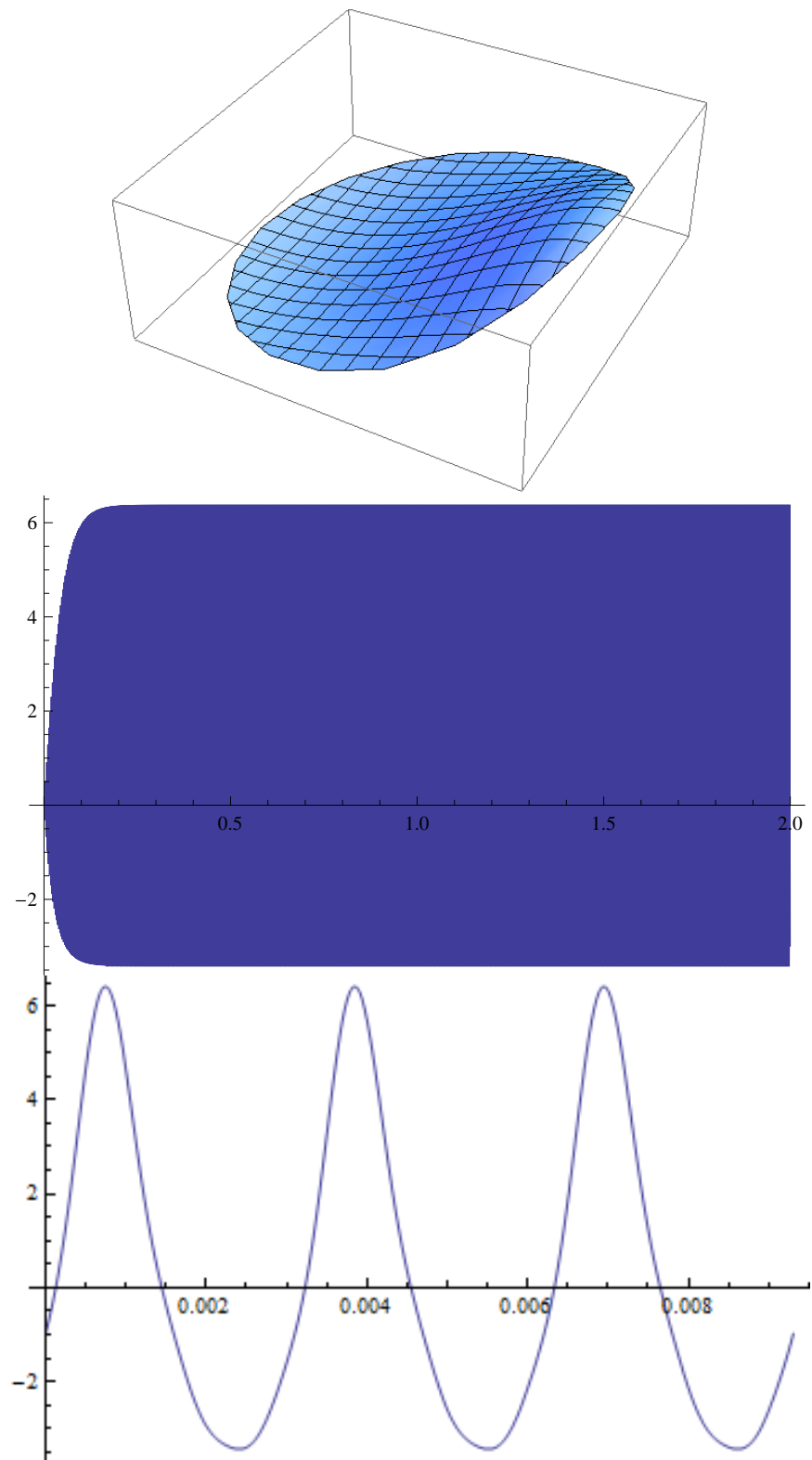


Figure C.1: The complete, superposed solution: (a) time snapshot of limit cycle mode shape; (b) time dependence at the wall for the complete simulation; (c) the limit cycle pressure-time wave as observed at a wall station.

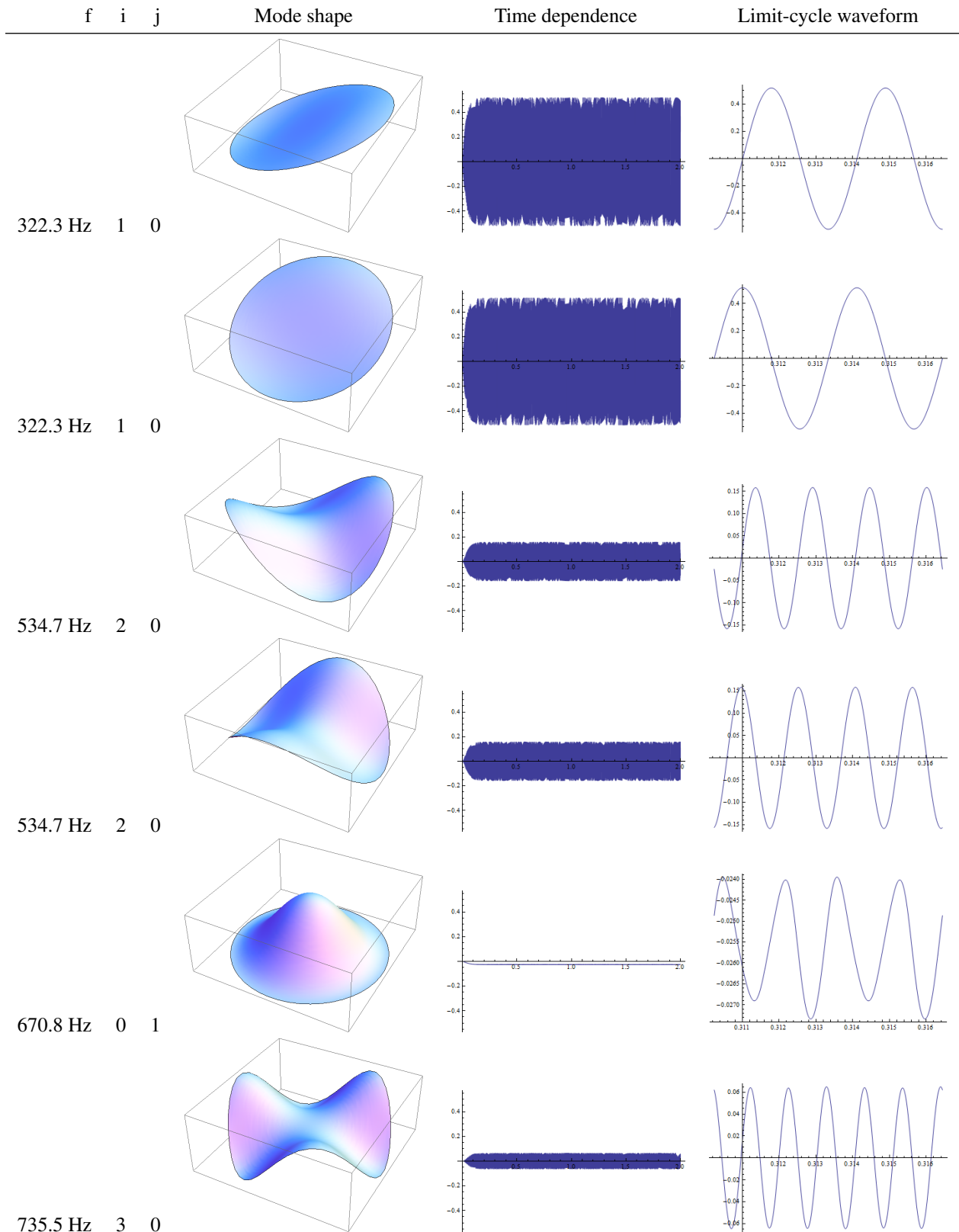


Figure C.2: Nonlinear oscillator simulation results, modes 1 through 6

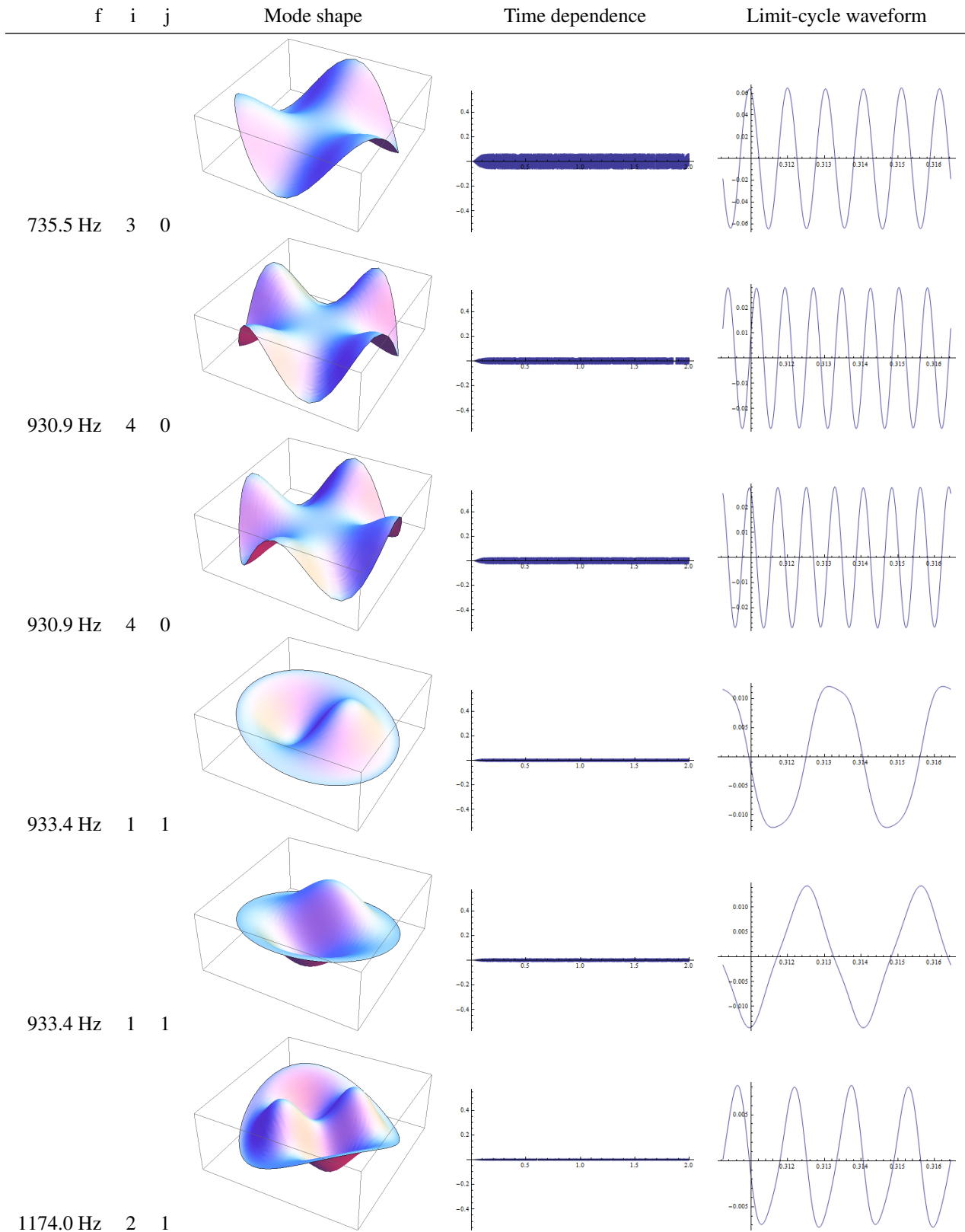


Figure C.3: Nonlinear oscillator simulation results, modes 7 through 12

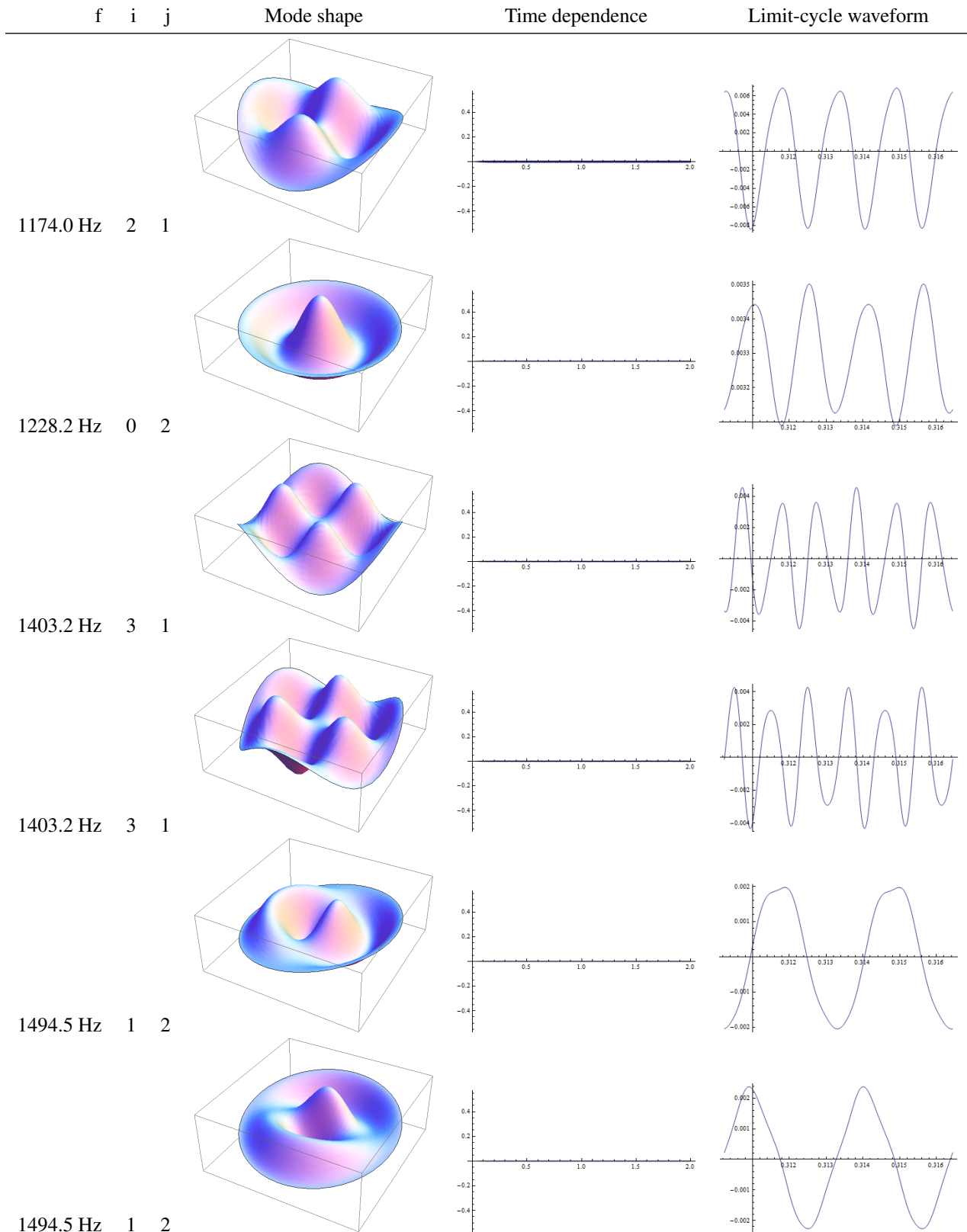


Figure C.4: Nonlinear oscillator simulation results, modes 13 through 18

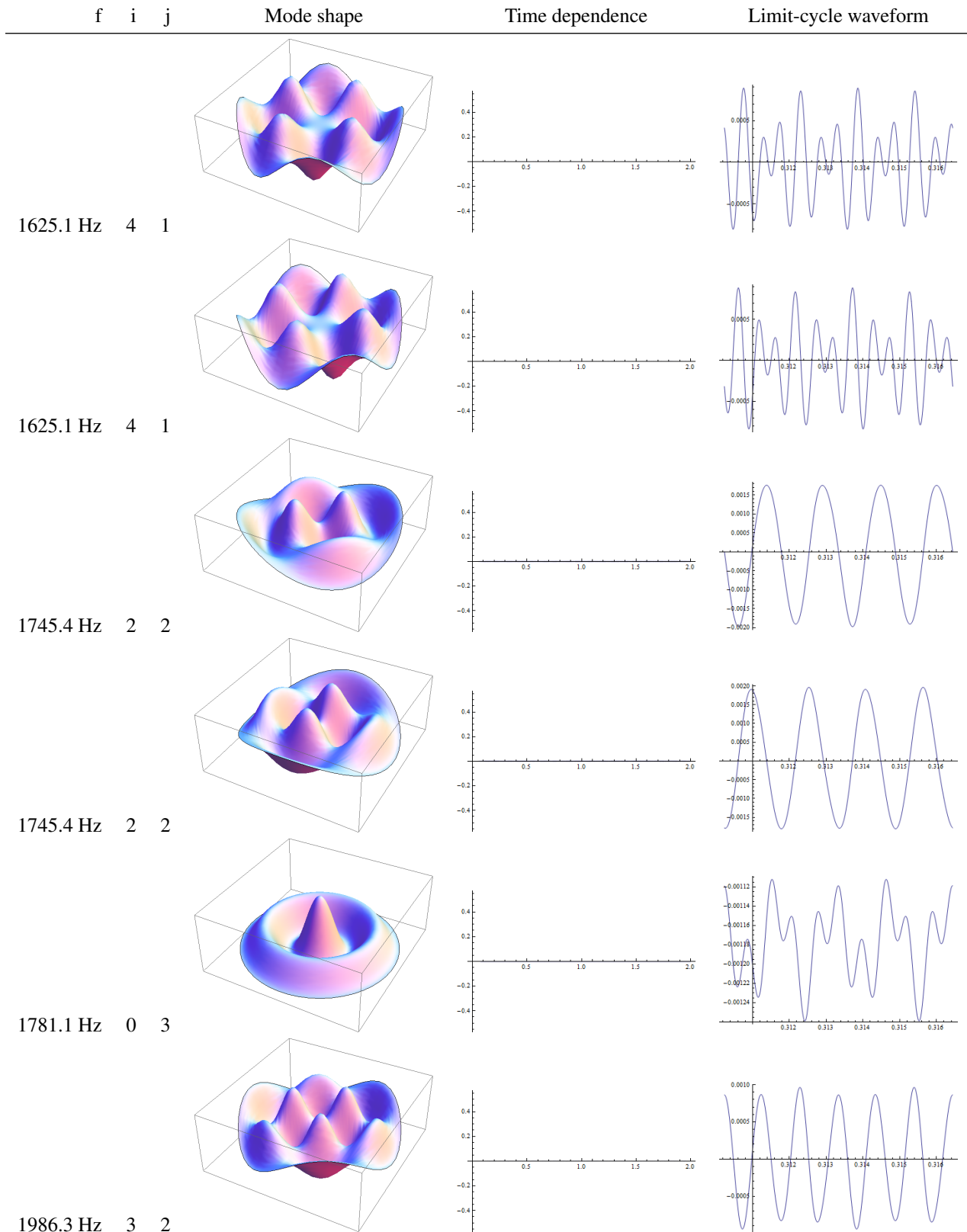


Figure C.5: Nonlinear oscillator simulation results, modes 19 through 24



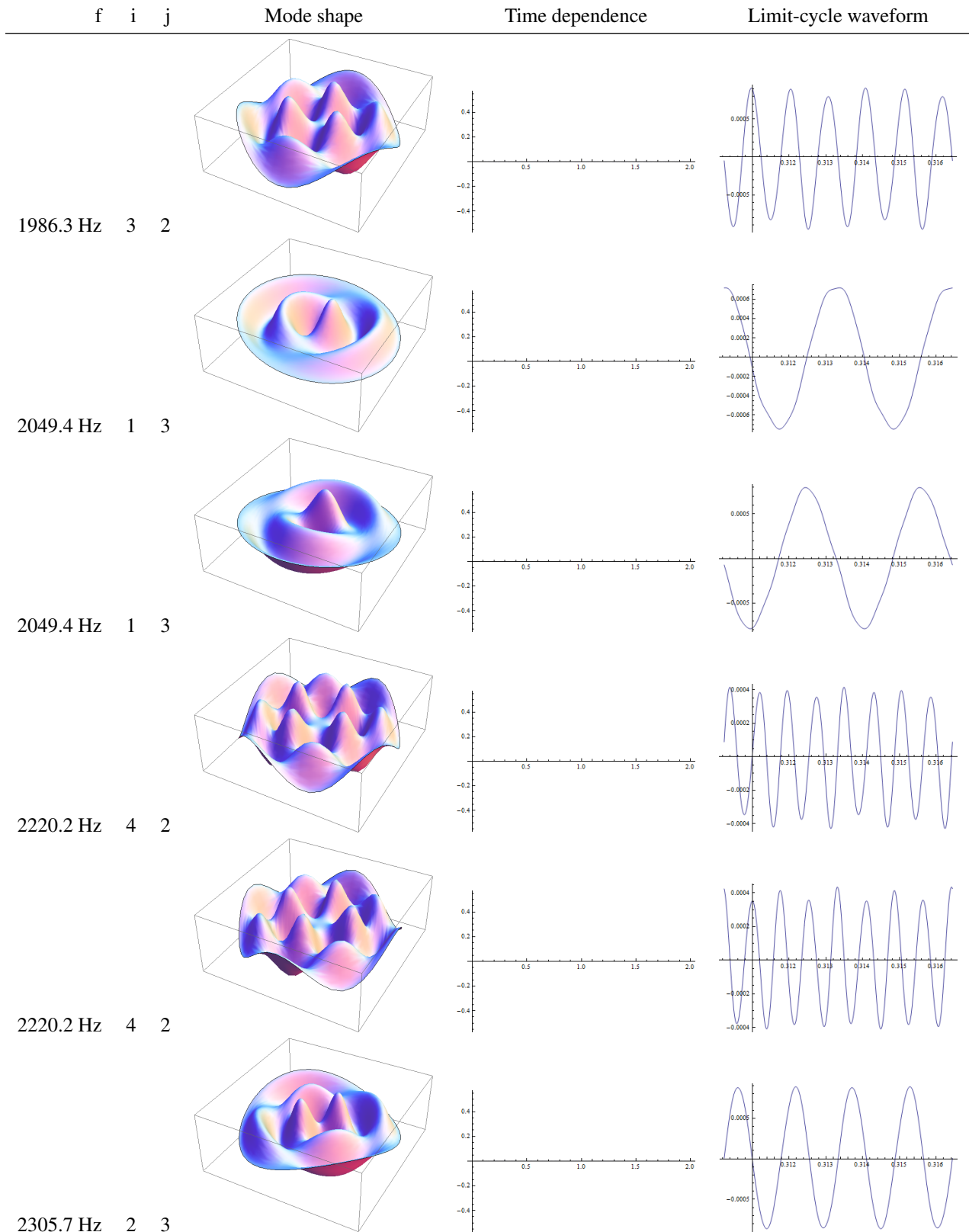


Figure C.6: Nonlinear oscillator simulation results, modes 25 through 30

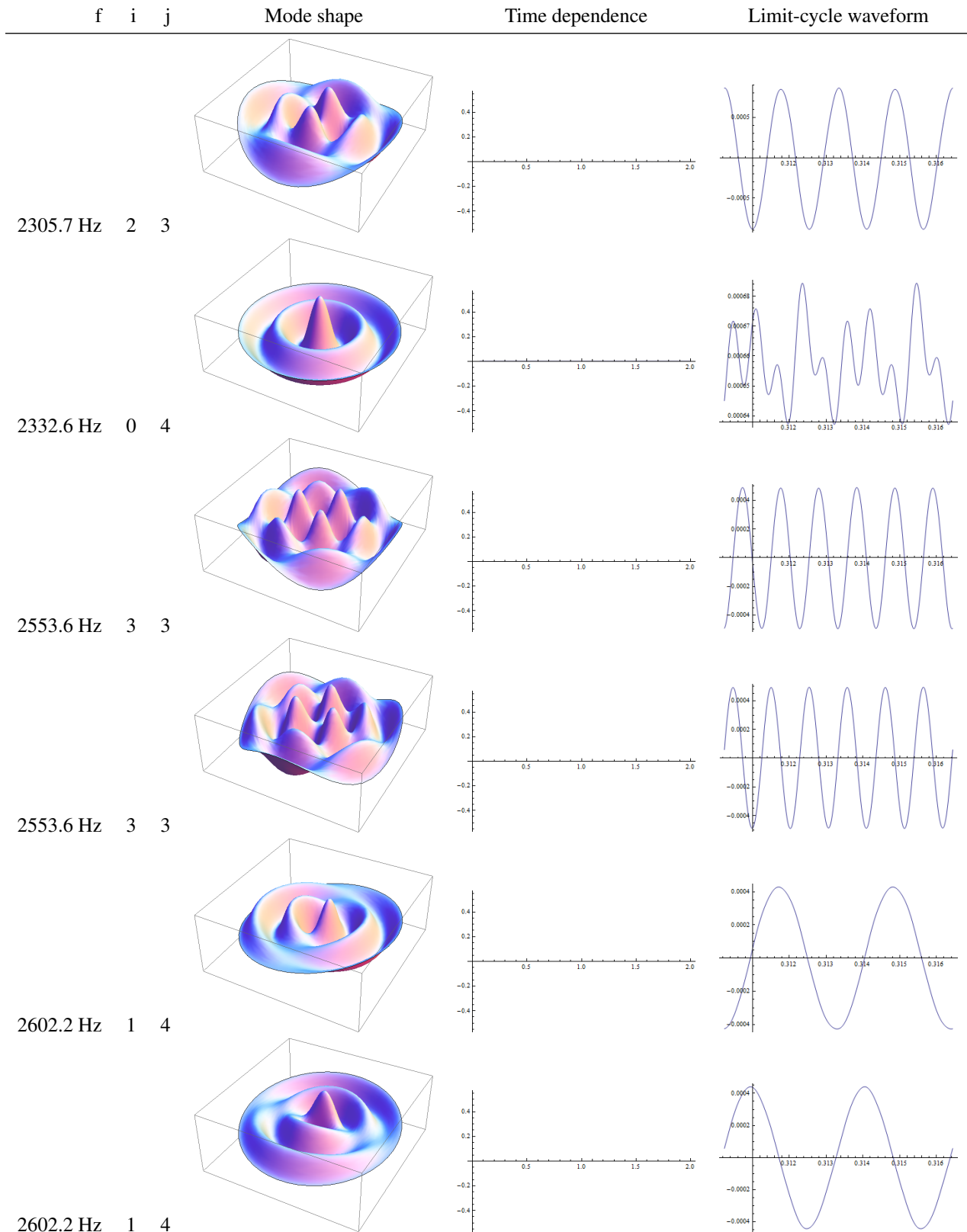


Figure C.7: Nonlinear oscillator simulation results, modes 31 through 36

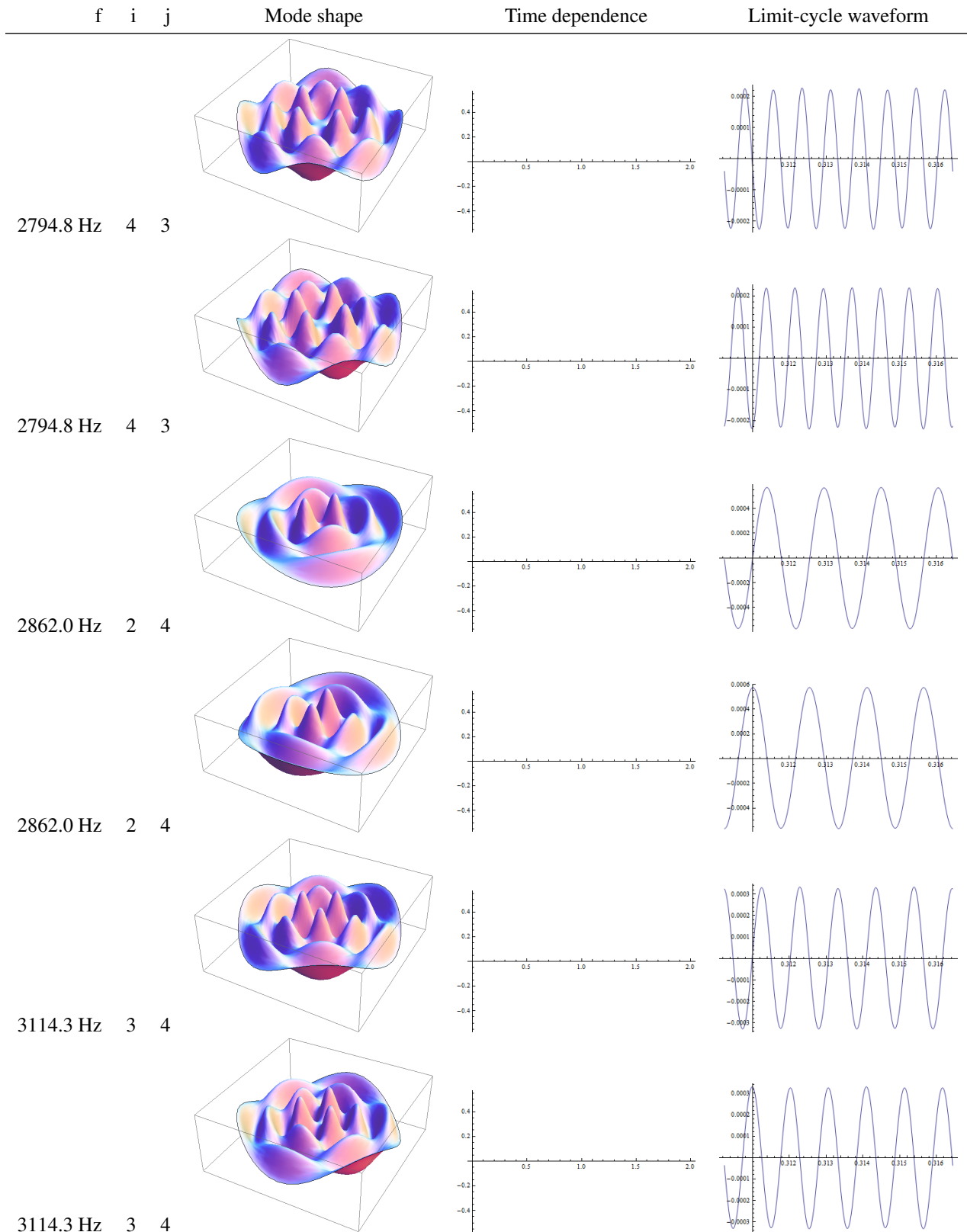


Figure C.8: Nonlinear oscillator simulation results, modes 37 through 42

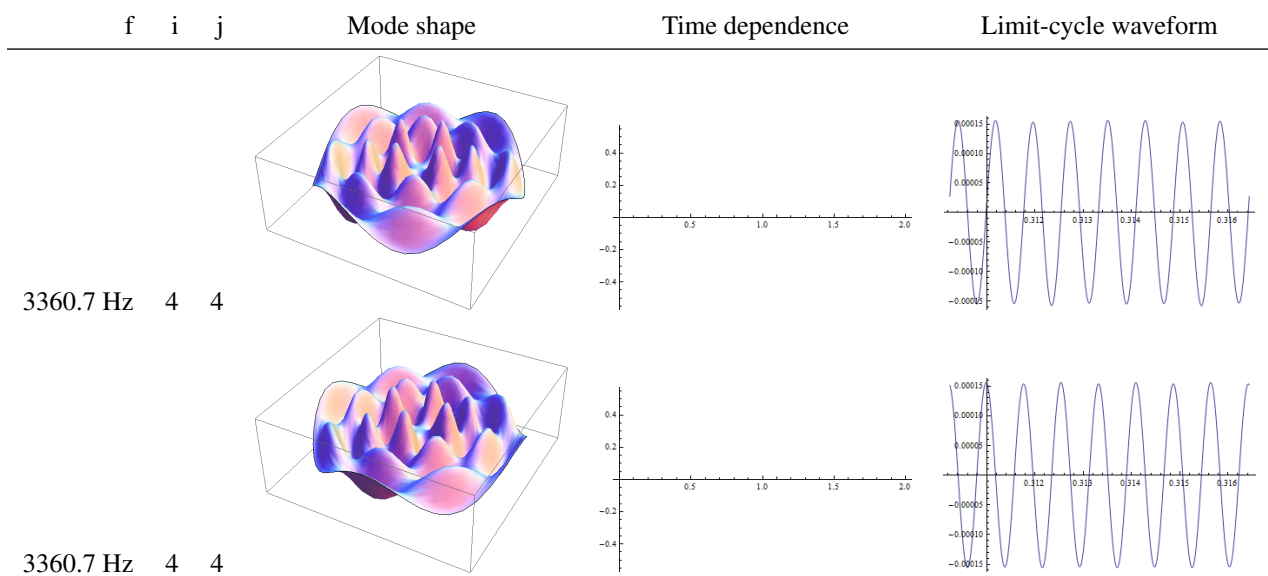


Figure C.9: Nonlinear oscillator simulation results, modes 43 through 44

# Appendix D

## Decomposition Examples

To see the value of this decomposition, consider what the mode/harmonic approximation implies for these coefficients. For example, Figure D.1 shows the sine coefficients  $a_{nm}$  for a simplified system. If the superposition of these three modes completely describes the system's periodic motion, then the approximation is exact. It satisfies two tests exactly:

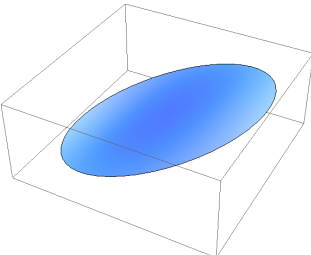
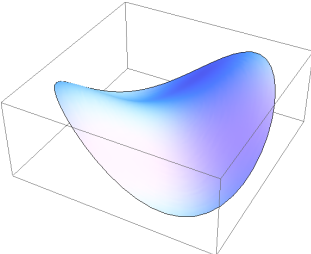
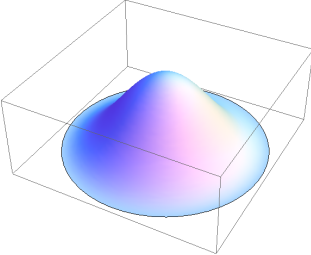
Mode	Shape	100Hz	200Hz	300Hz
1T		1.0	0.0	0.0
2T		0.0	0.3	0.0
1R		0.0	0.0	0.1

Figure D.1: System that meets mode/harmonic approximation

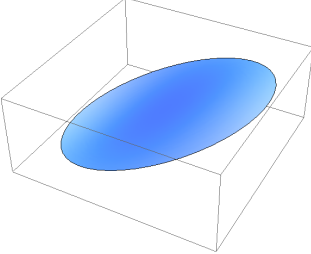
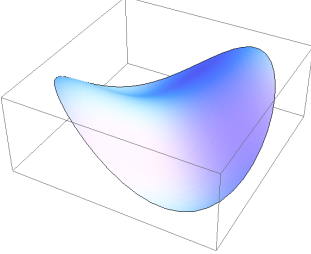
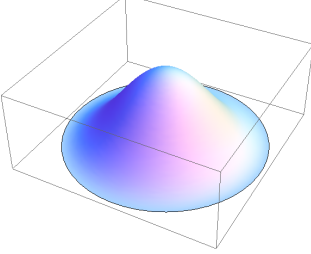
Mode	Shape	100Hz	200Hz	300Hz
1T		1.0	0.0	0.0
2T		1.0	0.0	0.0
1R		0.0	0.1	0.1

Figure D.2: System that does not meet mode/harmonic approximation

1. Each mode is ringing at only one frequency, and each frequency is an integer harmonic of the fundamental.
2. Each harmonic has one and only one acoustic mode contributing to its value (or, at most, has contributions from one and only one set of degenerate acoustic modes that have the same natural resonant frequency).

The example in Figure D.2 separately fails these two tests. It fails the first test, as the third mode is ringing at two different frequencies, i.e., does not have a simple sinusoidal time dependence. It fails the second test, as the first harmonic has two different modes contributing to its spatial dependence, i.e., has a shifted mode shape associated with a particular frequency.

In actual simulations, the situation is more complicated. Consider one final example, in Table D.3. In this case, the system matches the mode/harmonic assumption *to good approximation*. We quantify that approximation by using energy concepts. For each mode  $n$ , the fractional energy not in the “dominant” harmonic  $M$  is expressed as

$$E_{n,\text{err}} = \frac{\sum_{m \neq M} a_{nm}^2}{a_{nM}^2} \quad (\text{D.1})$$

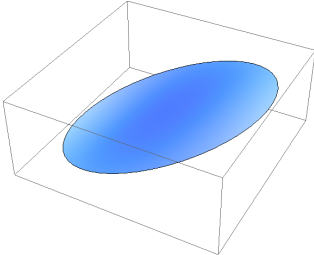
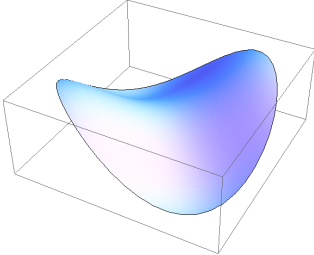
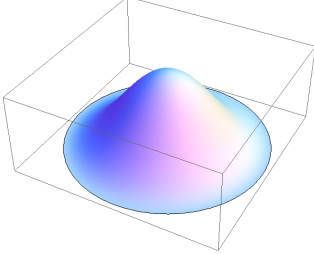
Mode	Shape	100Hz	200Hz	300Hz
1T		<b>0.85</b>	0.07	0.02
2T		0.04	<b>0.47</b>	0.03
1R		0.01	0.013	<b>0.15</b>

Figure D.3: System that approximately matches mode/harmonic assumption

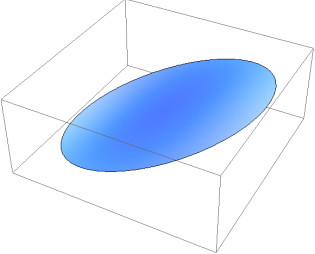
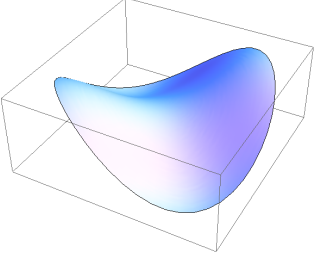
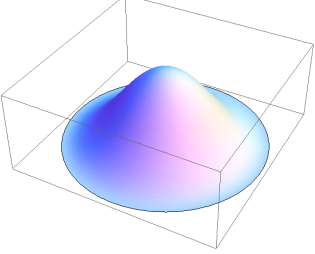
Mode	Shape	100Hz	200Hz	300Hz	Energy error
1T		0.85	0.07	0.02	0.733%
2T		0.04	0.47	0.03	1.13%
1R		0.01	0.013	0.15	1.20%
Energy error		0.235%	2.29%	5.78%	

Figure D.4: System that approximately matches mode/harmonic assumption, with error quantified

Similarly, for each harmonic  $m$ , the fractional energy not in the “dominant” mode  $N$  is expressed as

$$E_{m,\text{err}} = \frac{\sum_{n \neq N} a_{nm}^2}{a_{Nm}^2} \quad (\text{D.2})$$

Table D.4 revisits the system, but now including these error metrics. This can be further reduced to a single number: the ratio of energy in non-dominant mode or harmonics to the total energy in the system. This, however, requires careful inclusion of some constants. While integrating over the sin/cos functions produces a single constant that drops out of the equation, the spatial mode shapes are not normalized. So the total fractional error energy is given as:

$$E_{\text{err}} = \frac{\sum_{n,m \text{ not dominant}} \left( \int_V \psi_n^2 \right) a_{nm}^2}{\sum_{n,m} \left( \int_V \psi_n^2 \right) a_{nm}^2} \quad (\text{D.3})$$

For the last example problem given above, the result is  $E_{\text{err}} = 0.80\%$ , indicating that the approximation captures 99.2% of the total energy in the system. For the previous example which failed to meet the criteria (Table D.2), which of the



modes should be selected as the “dominant modes”? Considering the max of each row as dominant,  $E_{\text{err}} = 35.5\%$ , while considering the max of each column,  $E_{\text{err}} = 0.85\%$ . This accurately indicates that by energy, the system fails the no-shifted-mode-shape assumption far worse than it fails the single-frequency-per-mode assumption.

## **Vita**

Andrew Wilson is a PhD candidate at the University of Tennessee Space Institute. He received an Honors Bachelor of the Arts in Physics from the University of Chicago in 2005. That year, he co-founded Humanized, a small company dedicated to advanced human-computer interface design. In 2008, he began attending the Space Institute, which awarded him a Master's in Aerospace Engineering in 2010.